Spring 2012

Dynamics and Control of Satellite Relative Motion in Proximity Operations

Mohamed Elsayed Aly Abd Elaziz Okasha
Old Dominion University

DYNAMICS AND CONTROL OF SATELLITE RELATIVE MOTION IN

PROXIMITY OPERATIONS

by

Mohamed Elsayed Aly Abd Elaziz Okasha
B.S. June 2000, Cairo University, Egypt
M.S. October 2005, Cairo University, Egypt

A Dissertation Submitted to the Faculty of
Old Dominion University in Partial Fulfillment of the
Requirements for the Degree of

DOCTOR OF PHILOSOPHY

AEROSPACE ENGINEERING

OLD DOMINION UNIVERSITY
May 2012

Approved by:

_____
Brett Newman (Director)

_____
Robert Ash (Member)

_____
Thomas Alberts (Member)

_____
Zhao Sun (Member)

ABSTRACT

DYNAMICS AND CONTROL OF SATELLITE RELATIVE MOTION IN PROXIMITY OPERATIONS

Mohamed Okasha
Old Dominion University, 2012
Director: Dr. Brett Newman

In this dissertation, the development of relative navigation, guidance, and control algorithms of an autonomous space rendezvous and docking system are presented. These algorithms are based on innovative formulations of the relative motion equations that are completely explicit in time. The navigation system uses an extended Kalman filter based on these formulations to estimate the relative position and velocity of the chaser vehicle with respect to the target vehicle and the chaser attitude and gyro biases. This filter uses the range and angle measurements of the target relative to the chaser from a simulated LIDAR system, along with the star tracker and gyro measurements of the chaser. The corresponding measurement models, process noise matrix, and other filter parameters are provided. The guidance and control algorithms are based on the glideslope used in the past for rendezvous and proximity operations of the Space Shuttle with other vehicles. These algorithms are used to approach, flyaround, and to depart from a target vehicle in elliptic orbits. The algorithms are general and able to translate the chaser vehicle in any direction, decelerate while approaching the target vehicle, and accelerate when moving away. Numerical nonlinear simulations that illustrate the relative navigation, attitude estimation, guidance, and control algorithm's, as well as performance and accuracy are evaluated in the research study.

ACKNOWLEDGMENTS

There are several people deserving of special mention for their contributions to this dissertation. First, I would like to express my deep thanks to my supervisor and dissertation committee chair Dr. Brett Newman for his advice, guidance, patience, and thorough discussions during the whole period of my doctoral program. Second, I would like to express my gratitude to my dissertation committee members, Dr. Robert Ash and Dr. Thomas Alberts, for their advice and recommendations especially during my doctoral course work. During Dr. Ash's class of spacecraft mission analysis, I was able to pick up the idea of my point of research. His discussion inspired me to do the research and his wise advice was extremely valuable. The independent study that Dr. Alberts allowed me to take with him was very important for my dissertation work regarding Kalman filter estimation techniques. Third, many thanks go to all the faculty, staff, and fellow students in the Aerospace Engineering Department for giving me the opportunity to pursue the Ph.D. degree. In particular, I thank Dr. Colin Britcher, Chairman of the Aerospace Engineering Department, for working so hard to support and solve my financial difficulties. Lastly, I would like to express my deep thanks and love to my family. They are the source of the good things in my life.

NOMENCLATURE

i_X, i_Y, i_Z	Inertial axes unit vectors
i_x, i_y, i_z	Local vertical local horizontal (LVLH) axes unit vectors
$i_{x_b}, i_{y_b}, i_{z_b}$	Body axes unit vectors
$i_{x_g}, i_{y_g}, i_{z_g}$	Geometric axes unit vectors
R_c	Chaser position vector
R_t	Target position vector
ρ	Relative position vector of the chaser with respect to the target
x, y, z	Relative position vector components in LVLH frame
f_c, f_t	Chaser and target external acceleration vectors
f_g, f_a, f_c, f_w	Vehicle gravity gradient, aerodynamic, control, and unmodeled random acceleration vectors
R, R	Position vector and its magnitude
V, V	Velocity vector and its magnitude
$a, e, i, \Omega, \omega, f$	Semi-major axis, eccentricity, inclination, right ascension, argument of periapsis, and true anomaly
b, p	Semi-minor axis and semi-latus rectum
H, H	Angular momentum vector and its magnitude
X, Y, Z	Components of the spacecraft position vector in inertial frame
$\omega, \dot{\omega}$	Angular velocity and acceleration vectors
ρ_n	Normalized relative position vector
ρ_n', ρ_n''	Normalized relative position vector rates with respect to true anomaly

ρ', ρ''	Relative position vector rates with respect to true anomaly
x_n, y_n, z_n	Normalized relative position vector components
x_n', y_n', z_n'	Normalized relative position vector rate components
μ	Gravitational constant
C_D	Atmospheric drag coefficient
A	Cross sectional area
m	Spacecraft mass
ρ	Atmospheric density
x	State vector
ϕ	State transition matrix
I	Unity matrix
E	Eccentric anomaly
Δt	Time step
t	Current time
t_0	Initial time
T	Transfer time
ΔV	Classical incremental velocity
r	Glideslope position vector
$r, \dot{r}$	Glideslope magnitude and its rate
$\gamma, \lambda, c_{r_1}, c_{r_2}, c_{r_3}$	Glideslope constants
$\hat{u}_r$	Glideslope unit direction
N	Number of impulses
θ	Angle

$\Delta\theta$	Angle step
w_i	Process noise vector
v_i	Measurement noise vector
i_{los}	Unit line of sight vector
q	Quaternion vector
I_c, I_t	Chaser and target inertia tensor
τ	Total vehicle torque vector
b, ϵ, f, v	Sensor bias, misalignment, scale factor, and noise vectors
ρ, α, β	Range, azimuth, and elevation
K_k, P_k, Q_k	Kalman filter gain, error covariance, and process noise matrices
H_k, R_k	Kalman filter sensitivity, and measurement covariance matrices
K_q, K_ω	Proportional and derivative rotational control gain matrices
$K_\rho, K_{\dot{\rho}}$	Proportional and derivative translational control gain matrices
$[.]^I, [.]^{LVLH}$	Inertial and LVLH coordinate frames
$(\dot{\,}), (\ddot{\,})$	Derivatives with respect to time
$(\cdot)', (\cdot)''$	Derivatives with respect to true anomaly

TABLE OF CONTENTS

LIST OF TABLES

LIST OF FIGURES

1. INTRODUCTION AND LITERATURE REVIEW

1.1 Introduction

Autonomous rendezvous and docking of satellites in orbit is one of the most essential technologies for future space transportation missions such as International Space Station (ISS) supply and repair, and automated inspection, servicing, and assembly of space systems. However, in most space programs, the rendezvous and docking functions are currently achieved by manual operations. Autonomous proximity operations are required for a large number of future mission concepts but cannot be achieved routinely at present. For the docking of two satellites, highly precise and robust position and attitude control is required, which further requires precise measurements of the relative position and attitude of the docking satellite.[1-3]

Several research projects dealing with autonomous rendezvous and docking of orbiting satellites have been conducted over the past several decades. The Russians and Americans each independently performed successful on-orbit docking maneuvers between space vehicles in the 1960's. The Russians employed a standardized, largely automated system that could operate with humans only having a supervisory role, but it also had a complete set of pilot controls to allow human intervention if necessary.[4] The Americans, on the other hand, opted for a series of "one-off" docking schemes that were unique to each mission, rather than using a standard system design. American docking operations also required a human to be in the control loop at all times and the systems used a low level of automation.[5-7] This trend has continued to the present day in American satellite docking operations, as a human-controlled satellite docking is performed each time a Space Shuttle visits the ISS (see Figure 1.1).
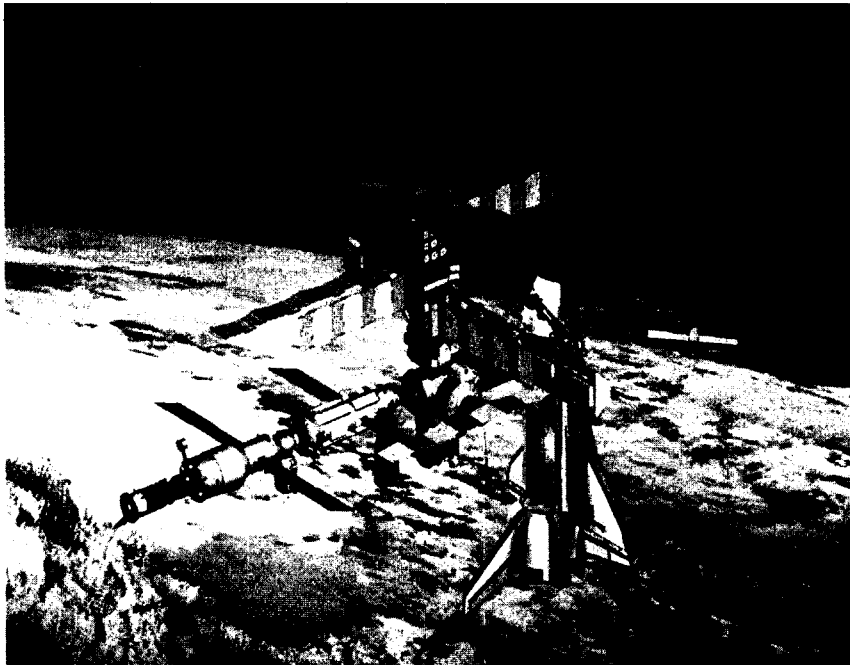
Figure 1.1 Space Shuttle and International Space Station Docking

The Russians first demonstrated automated docking, which is conducting a docking maneuver without a human in the control loop, by performing an automated docking of unmanned Cosmos vehicles 186 and 188 in October 1967 (see the illustration in Figure 1.2). The vehicles successfully docked and remained in that configuration for three and a half hours, then separated and successfully executed their respective re-entry commands.[8] The Russians continue to have success in conducting on-orbit automated satellite dockings, even to the present day. Recently, they docked various vehicles with the Mir space station while it orbited, and the ISS is also regularly visited by Russian Progress vehicles that dock automatically.[1]

Japan became the second nation with a space program to successfully perform an on-orbit automated dock. In 1998, Mitsubishi Electric successfully docked two unmanned satellites under the funding and direction of Japan's National Space Development Agency (JAXA). Their investigation established confidence in the feasibility of

autonomous docking of satellites and provided insights related to overcoming the various mishaps that can occur.[9,10] While the Japanese have attempted to repeat this on-orbit automated docking success, they are re-using some of the technology demonstrated in the development of an automated shuttle called the H-II Transfer Vehicle (HTV) that was launched on September 10, 2009.[11]
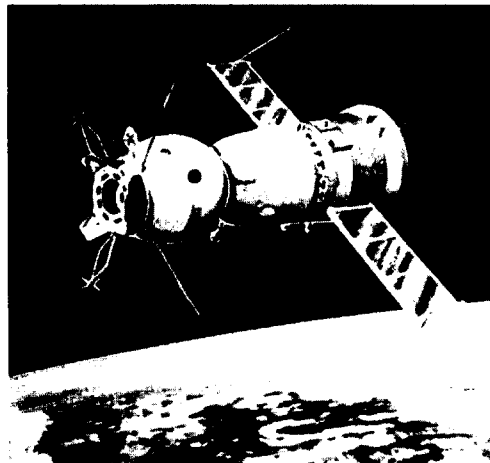
Figure 1.2 Cosmos 186 and 188

NASA was not successful in its attempted proximity operations demonstration mission in 2005, illustrated in Figure 1.3 and called DART (Demonstration of Autonomous Rendezvous Technology), but partnered with the Defense Advanced Research Projects Agency (DARPA) for a successful and more comprehensive rendezvous and docking demonstration named Orbital Express in 2007 (see Figure 1.4).[12,13] The European Space Agency launched an unmanned ISS re-supply shuttle, named the Automated Transfer Vehicle (ATV), in March 2008. The ATV docked to the ISS on April 3, 2008. Due to extensive redundancy and fault tolerance, the ATV is largely autonomous as well as completely automated, having no pilot controls; the only means of human intervention are remote emergency interrupt and abort capabilities.[14]

Figure 1.3 DART Orbital Rendezvous

Figure 1.4 Orbital Express Rendezvous

Various navigation sensors are used to determine the target satellite's best estimated location and orientation state, and then to feed the estimated relative state information to an automated rendezvous and docking operation controller. Highly accurate relative navigation is required to face the environmental conditions or poor scenario geometry, for successful docking. The relative navigation (consisting of both relative position and relative orientation) information between two satellites must be accurately measured in real-time, and successfully relayed to the command computer, in order to accomplish safe maneuvering of the vehicles relative to each other. This maneuvering requires a sensor package onboard the vehicles that can estimate the

instantaneous 6-DOF (degree of freedom) relative navigation quantities at a useful rate and accuracy.

The most common system used to accomplish this in near-Earth situations is the Global Positioning System (GPS). Basically, this system uses a constellation of several satellites to triangulate the current position of a receiver unit. The accuracy and solution rate using GPS varies widely depending on the application and especially the processing done on the received satellite signals, but real-world on-orbit errors are generally on the order of meters. Thus, relative GPS (RGPS), currently the most accurate type of GPS, is considered to be an acceptable relative navigation solution for general automated relative satellite maneuvers in low Earth orbit. However, RGPS is not accurate enough by itself to be used for docking. Another class of relative navigation sensors rely primarily on pattern or image recognition capabilities to provide the relative 6-DOF estimate. This type of sensor often pairs a camera with software that extracts and tracks features from successive images, by which an estimate of the motion of the vehicle relative to its target can be derived. A third major technique for estimating relative navigation information is to use laser range finders. As the name implies, laser beams are emitted from one vehicle to another, which reflects back to a receiver on the first vehicle. A relative position estimate can then be determined at long range, with full 6-DOF capability at shorter ranges.

Concerning the characteristics and performance required in the different ranges from a few hundred meters down to contact, a combination of laser finder and camera sensor types would provide optimal performance. The laser range finder type would provide range and line of sight information over the entire range, whereas the camera

sensor would provide all navigation parameters, including relative attitude, with increasing accuracy in the terminal phase of the approach.

Beside accurate sensing, controller design is also a key technology which needs to be solved. Autonomous satellite rendezvous and docking require very precise controlled translational and rotational maneuvers. These requirements frequently necessitate the use of nonlinear satellite dynamic models for control system design. To date, most control designs are based on the proportional-integral-derivative (PID) or linear-quadratic regulator (LQR) controller methodology.[15-17] Recently, some elements of robust control have been utilized in the controller design. Other methods utilizing Lyapunov control theory and sliding mode control techniques have been used to develop a nonlinear feedback control law.[18,19]

The complexity of the rendezvous and docking process results from the multitude of conditions and constraints which must be fulfilled: functions required by abroad chaser and target vehicles, monitoring and high level control by their respective control centers on the ground, together with the infrastructure for communication and navigation in orbit and on the ground. Primarily, what makes automated docking so difficult is the sheer complexity of replacing human senses, training, common sense, and decision-making ability with computerized systems. This complexity replacement must be accomplished while at the same time making the entire docking system robust and fault-tolerant enough to succeed on its own in a real-time scenario.

1.2 Literature Review

In this section, previous works associated with the dynamics and control of satellite relative motion have been reviewed. Three categories are considered in this

literature survey: relative motion dynamics, relative motion guidance, and relative motion control.

1.2.1 Relative Motion Dynamics

The simplest model governing the dynamics of relative motion in a planetary gravitational field is given by the Clohessy-Wiltshire (CW) equations.[20] The reference satellite orbit was assumed to be circular and the reference relative orbit coordinate distances were small compared to the reference orbit radius, so that the resulting equation of motion was linearized. These equations were derived in the absence of perturbation forces. In 1963, Lawden[21] found an improved form for relative motion including reference orbit eccentricity, and Carter[22] later extended Lawden's solution. These equations and their corresponding solutions were based on the Tschauner-Hempel (TH) model.[23] This model used reference orbit true anomaly as an independent variable instead of time. State transition matrices that reflect the effect of eccentricity have also been derived, and they were presented in Melton,[24] Broucke,[25] and Yamanaka and Ankersen[26] but they were implicit in time. Next, Kechichian[27] developed an exact formulation of a general elliptic orbit to analyze the relative motion in the presence of J_2 potential and atmospheric drag. In this study however, the resulting equations required numerical integration over time. Sedwick et al[28] applied the J_2 potential forcing function to the right hand side of the CW equations. Schweighart[29] followed these equations and found analytic solutions. Melton[24] later developed an approximate solution expanding the state transition matrix in powers of eccentricity with time explicit representation. Recently, Vadali[30] achieved an exact analytical expression in terms of differential orbital elements for relative motion problems. His method was called the unit sphere approach and it was

employed in a long term prediction of mean orbital elements, including nonlinear J_2 effects, and then in transforming Hill's relative coordinate frame.[31-33]

1.2.2 Relative Motion Guidance

A glideslope is a straight path from the current location of the chaser satellite to its intended destination, which may be a target satellite center of mass, a docking port, or a location of interest in space near the target. The history, motivation, and analysis of the glideslope technique in the context of the Space Shuttle are given in Reference 34, where the glideslope analysis therein is limited to the guidance of the chaser in the orbit plane, using canted thrusters. Pearson[34] formulated a relationship between the glideslope angle, thruster cant angle, range and range rate. For analysis, the CW equations in rectilinear coordinates were transformed into polar coordinates. Reference 35, which generalizes this algorithm using a matrix formulation instead of the polar transformation of Reference 34, provides a general multipulse guidance algorithm to move a chaser vehicle in the vicinity of a target vehicle, decelerating if approaching the target and accelerating if receding away from it. This motion is not limited to the tangential direction (V-bar) or radial direction (R-bar), nor restricted to the target orbit plane. Furthermore, it is assumed that, unlike the canted thruster in Reference 34, six independent thrusters are available to produce an incremental momentum vector in any direction.

Reference 36 is concerned with guidance algorithms for flying around a target spacecraft autonomously. A chaser satellite can circumnavigate a target satellite in an in-plane elliptic path in one orbit period, with the target at its center. Under ideal conditions, this elliptic path, once established with proper initial conditions, persists without any additional thruster firing. The largest distance of the chaser from the target is along the

local horizontal, this distance being twice the shortest distance along the local vertical. This elliptic geometry and one complete orbit period for circumnavigation, however, may not always be compatible with the mission requirements. The mission designer may instead require a faster, circular flyaround, perhaps also not necessarily in the orbit plane.[35]

All of these algorithms can be implemented only if the target's orbit and the relative location of the chaser are known. Furthermore, real rendezvous operations with docking, though lately commonplace with the ongoing logistical support of International Space Station, are extraordinarily complex events because they include, among other things, sensing of the target by sensors onboard the chaser, inertial navigation of the chaser and target vehicles, chaser-target relative navigation, Kaman filtering with or without global position system receivers on the two vehicles, attitude determination of both vehicles, and more. References 37 and 38 describe these complexities for rendezvous and docking of the Space Shuttle with Mir when astronauts were in the loop. References 39 and 40, in contrast, detail autonomous rendezvous and docking using combined GPS and inertial navigation systems (INS), and visible/infrared and video guidance sensors.

1.2.3 Relative Motion Control

Numerous investigations have been conducted on relative motion regulation and tracking problems. The focus in this literature survey will be on the control problems of translational and rotational motion of the chaser with respect to the target vehicle.

With respect to the translational control problems, Battin[41] dedicated a whole chapter of his astrodynamics text to determine the orbital trajectory between two position

vectors, given the time of flight and the gravitational parameter, μ. This problem is well-known as Lambert's problem.[42] The technique of solving Lambert's problem for a given scenario finds extensive use as the catch-all of rendezvous trajectory design. Given the current chaser position and a desired relative position some specified time later, it is possible to use the Lambert algorithm to connect the two points in the desired time.[43] A very simple and elegant solution to Lambert's problem can be found for the case of circular or near-circular orbits. This algorithm is based on the CW equations of relative motion for orbits with small eccentricity.[35] A recent study proposed for close-in proximity operations, such as inspection and docking, employment of a proportional-derivative controller for translation control. The translation control algorithm computes the required ΔV to track the required trajectory specified by the guidance algorithms.[17] Recent nonlinear control techniques based on Lypunov analysis and Matrosov's theorem for satellite proximity operations can be found in References 18 and 19.

Unlike translational control, the rotational control problems for relative motion are typically solved by a traditional feedback system. The chaser vehicle needs to track the target vehicle for visual inspections, docking port alignment and also to orient itself to perform a variety of thruster burns for different translational maneuvers. The task of the control system is to orient the attitude and angular velocity of a satellite with that of the target. This system has been addressed in previous studies in Refenernces 44-48. For the concept of relative motion, satellite tracking control systems have also been developed with the coordinated attitude control of each satellite for simultaneous pointing and tracking to a target.[49-52] A recently presented study proposed multi-target attitude tracking of formation flying.[53] A chaser satellite had a camera for tracking a ground target and an

antenna for tracking a target satellite. To compute angular velocity and acceleration, the study introduced a method to increase the efficiency of tracking the camera, while the attitude of the antenna was measured in the body-fixed frame. The robust tracking controller was developed by deriving a desired inverse system, which converts the attitude tracking problem into a regulator problem, using sliding mode techniques.

1.3 Dissertation Objectives and Contributions

The objectives of this dissertation are to thoroughly exploit the guidance, navigation, and control system in order to analyze and design satellite relative motion in proximity operations and to ensure successful autonomous rendezvous and docking of the chaser with the target vehicle.

The dissertation is divided into three main problems associated with relative motion: dynamics, guidance, and control. Specifically, first in the portion pertaining to dynamics, the contribution of the study will focus on developing a coupled, nonlinear relative orbit and attitude dynamic model for satellite relative motion between the target and the chaser vehicles. This model should take into account the most dominant types of perturbations that could have an effect on the trajectory motion. Second, as a basis of design, the model will be linearized in order to understand such motions, and analytic solutions will be established to determine the degree of system nonlinearity. This type of analysis will enhance knowledge of inherent characteristics and dimensions of the model, which in turn will be emphasized while applying control techniques. Finally, with reference to the dynamics problem, this investigation will examine certain types of model uncertainties in terms of their impact on the robustness of controller design. The proposed numerical and analytical dynamics models are evaluated through different examples and

scenarios showing how they are useful as an effective tool for addressing the problems of satellite relative motion.

As a primary goal of the portion pertaining to the guidance system, several proposed guidance algorithms have been developed for autonomous rendezvous to approach, to flyaround, and to depart from a target vehicle in any orbit. The algorithms are based on the proposed analytical and numerical models of the relative motion. They are an extension of previously published guidance algorithms for rendezvous and proximity operations of the Space Shuttle with other vehicles employing astronauts in the guidance loop. The implementations of these algorithms require estimation of the position and velocity of the chaser relative to the target. This relative navigation is performed with an extended Kalman filter using range and angle measurements of the target relative to the chaser and the satellite attitude estimates from an inertial navigation system. Several scenarios are simulated to illustrate the guidance algorithms and relative navigation.

In the portion of the dissertation covering the control problem, the study will focus on developing a relative translational and rotational control system for the two satellites. The control system should be able to compensate for the effect of perturbations and to be robust against uncertainties in the model. The translational control system has been designed by applying the analytical and numerical solution of satellite relative motion. Two types of translational controllers are developed and evaluated in terms of convergence rate, stability, and accuracy. The first controller is based on the analytical solution and it is open loop discrete control, while the second controller is based on the numerical solution and it is closed loop continuous control. Regarding the rotational

control, relative tracking control systems have been developed and evaluated for the two satellites. Based on the evaluation, the research proposes an appropriate tracking control system and estimation technique for autonomous rendezvous and docking of satellite relative motions.

1.4 Dissertation Overview

In this section, the organization of this dissertation, as well as the specific topics that are dealt with, will be discussed. This chapter serves as an introduction to the contents of the dissertation.

Chapter 2 consists of three main sections. In the first section, the system models for relative motion of rendezvous problem are developed and explored in different coordinate frames based on the Gauss and Cowell methods. The CW and TH models are derived, starting from the nonlinear model, in the absence of various disturbance forces. In addition, a proposed linear high fidelity model is derived, considering J_2 and atmospheric drag perturbation forces. The closed form analytical solutions of the TH model are obtained and numerical evaluations of the model are examined. In the second section, autonomous guidance algorithms to move the chaser in close proximity to the target are presented. These algorithms are based on the closed form solution of the TH model and they are used to approach, to flyaround, and to depart from a target vehicle. In the last section, open loop control techniques are considered to move the chaser from any location to its intended one governed by the guidance algorithms. These open loop techniques are based on the classical two-impulse rendezvous targeting. Simulations are performed by using the TH model in different scenarios to validate and verify the guidance algorithms and the open loop control methods.

Chapter 3 will introduce the standard Kalman filter and provide a summary of the main theory and equations behind this filter to serve as a reference for the work in this dissertation. A summary filter flow chart, state propagation equations, and measurement update equations of the filter are also presented with the application for the space navigation system.

Chapters 4 and 5 will present the development of relative navigation, guidance, and control algorithms of an autonomous space rendezvous and docking system. These algorithms are based on using the proposed solution of relative motion and guidance algorithms presented through Chapter 2 in a rotating, orthogonal coordinate frame fixed on the target in an arbitrary elliptic orbit. The navigation model and an extended Kalman filter are presented for relative motion and attitude estimations along with the relative attitude controller. The relative navigation, guidance, and control algorithm's performance and accuracy are illustrated and validated through different scenarios.

Finally, the dissertation is summarized in Chapter 6, and concluding remarks on future work are presented.

2. RELATIVE MOTION DYNAMICS

2.1 Introduction

Spacecraft relative motion concepts have been studied since the beginning of the manned space program. The challenge was to have two spacecraft rendezvous and dock onto each other.[1,43,54] The Clohessy-Wiltshire (CW) equations of motion describe the relative proximity motion for circular orbits.[20] The CW equations are valid if two conditions are satisfied: (1) the distance between the chaser and the target is small compared with the distance between the target and the center of the attracting planet, and (2) the target orbit is near circular. The CW equations consist of three simple differential equations, which can be solved analytically. These solutions have been widely used for circular orbit rendezvous in practice. However, the target orbits are not necessarily circular. The Tschauner-Hempel (TH) equations describe the relative motion of a spacecraft in an arbitrary elliptic orbit.[23] The expressions generalize the CW equations and are similar to them in their derivation and types of applications. Tschauner and Hempel derived these equations from the viewpoint of the rendezvous of a spacecraft with an object in an elliptical orbit. They found complete solutions for elliptical orbits in terms of the eccentric anomaly. This advancement was followed by additional papers that present the complete analytical solution explicitly in time, expanding the state transition matrix in terms of eccentricity.[24-26,36,55,56] This form of solution is used to analyze the relative motion between the chaser and the target vehicles in the relative frame of motion more efficiently and rapidly than solving the exact nonlinear differential equations in the inertial coordinate system.

Algorithms for autonomous guidance of spacecraft to approach, to flyaround, and to depart from a target vehicle in circular orbits are found in References 35 and 57, and they are based on CW assumptions. This body of work is extended herein for elliptical orbits based on TH exact analytical solutions. By using a matrix formulation, a general multipulse guidance algorithm is used to move the chaser in the vicinity of the target vehicle, decelerating if approaching the target, and accelerating if receding away from it, which in turn is a desirable feature to ensure safety and collision avoidance behavior. In the case of flying around the target vehicle, increasing the number of pulses helps to decrease the errors between the virtual flyaround trajectory and the actual achieved one. The motion can be in a general direction and is not limited to the radial or the tangential direction, nor restricted to the target orbital plane. By using the closed form solution and the proposed guidance algorithms, fast mission analysis could be easily done and a good estimation of the total fuel required to complete the mission can be determined.

The analysis in the chapter is summarized as follows. First, in Section 2.2, the coordinate frames needed to describe the relative motion dynamics are defined. In Section 2.3, the relative dynamics equations of motion are presented for the chaser with respect to the target in a general perturbed orbit based on Gauss' and Cowell's variational equations. These equations of motion are developed in the inertial coordinate frame as well as in the relative coordinate frame. In Section 2.4, a linear high fidelity relative motion model is derived to describe relative motion in proximity operations, taking into account the gravitational J_2 perturbation and environmental atmospheric drag perturbation. In addition, the general TH and CW analytical solution of the linearized relative motion is obtained explicitly as a function of time in a rotating orthogonal

coordinate frame fixed to the target in an arbitrary elliptic orbit for the TH model and in a circular orbit for the CW model. The effect of target orbit eccentricity on relative motion is investigated and demonstrated in this section through simulation examples. These proposed linearized models can be used to study the relative motion dynamics insightfully. In Section 2.5, the guidance algorithms concerned with approaching, flying around, and departing from the target autonomously are developed with the help of a matrix formulation for classical two-impulse rendezvous. These guidance algorithms are illustrated through different numerical examples. Results demonstrate the brevity of the method and the accuracy of the analytical solution (TH Model) presented in the current chapter. Finally, in Section 2.6, conclusion of the work is presented and suggestions are made for future chapters.

2.2 Frames of Reference

In order to define the orbital motion, the absolute and relative trajectories, and the attitude motions, generally three types of coordinate frames are needed.[1]

- Orbit reference frames: to describe the orientation of the orbit relative to inertial space and to the Earth, and to describe the motion of a spacecraft within an orbit.

- Spacecraft local orbital reference frames: to describe the motion relative to a particular point in orbit or to another spacecraft.

- Spacecraft attitude and body frames: to describe dynamic and kinematic processes of the spacecraft relative to its center of mass.

2.2.1 Earth Centered Inertial Frame (ECI)

This coordinate frame will be used to describe the orbital motion around the center of the Earth and with respect to inertially fixed directions. The Earth is assumed to

be truly spherical and the origin of the frame is assumed to be located at its center. This frame is shown in Figure 2.1, with orthonormal basis $\{i_X, i_Y, i_Z\}$. The vectors i_X and i_Y lie in the equatorial plane, with i_X coinciding with the line of equinoxes, and with i_Z passing through the North Pole.
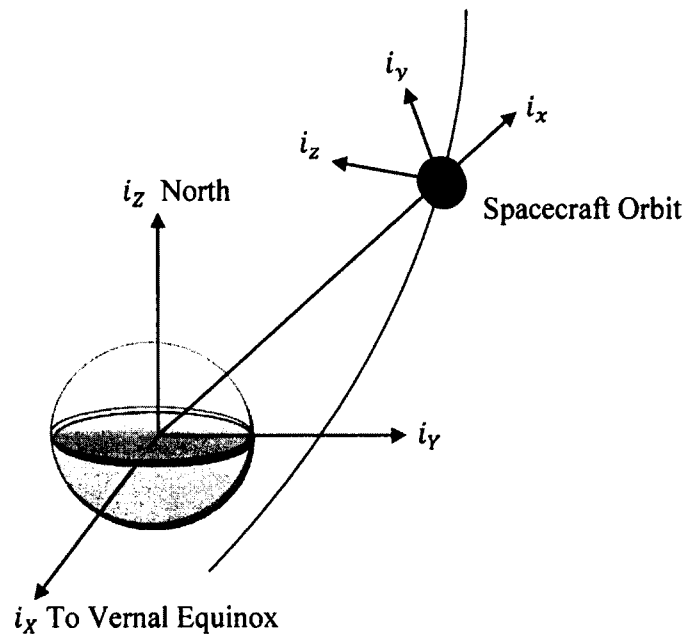
Figure 2.1 ECI and LVLH Frames

2.2.2 Local Vertical Local Horizontal Frame (LVLH)

As shown in Figure 2.1, this coordinate frame is used to describe motions with respect to the moving position and direction towards the center of the Earth of an orbiting body. The origin of this coordinate is located at the center of mass of the spacecraft and it has basis $\{i_x, i_y, i_z\}$, with i_x lying along the radius vector from the Earth's center to the spacecraft, i_z coinciding with the normal to the plane defined by the position and velocity vectors of the spacecraft, and $i_y = i_z \times i_x$.

2.2.3 Body Attitude Frame

The body attitude frame, with orthonormal basis $\{i_{x_b}, i_{y_b}, i_{z_b}\}$, is used to describe all rotations of the body of a spacecraft as shown in Figure 2.2. The nominal direction of this frame depends on the maneuver strategy of the mission. For example, in the final phase of a rendezvous and docking mission, one of the axes is usually pointing in the direction of the docking axis and the lateral axis is often aligned with the positive or negative of the angular momentum vector of the orbit.
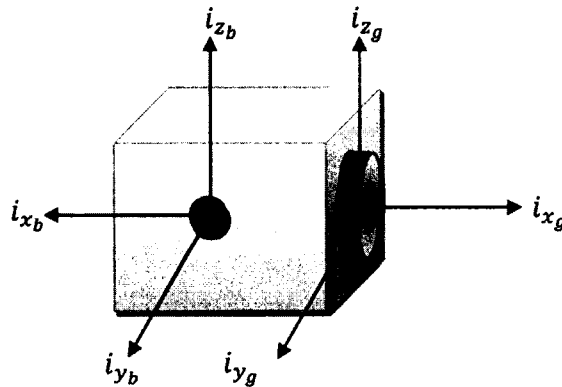
Figure 2.2 Body and Geometry Frames

2.2.4 Geometric Frames

These coordinate frames are used to describe translations and rotations of the spacecraft with respect to location and direction of equipment, such as sensors, thrusters, or the docking mechanism. The origin of these frames is defined by the equipment and their axes are aligned with or under a fixed angle to the attitude frame. An example of the orthonormal basis of these frames is illustrated in Figure 2.2 and it is denoted by $\{i_{x_g}, i_{y_g}, i_{z_g}\}$. The transformation from the spacecraft attitude frame to one of the geometric frames is a parallel shift from the center of mass of the spacecraft and a fixed rotation around the origin of the frame.

2.3 Orbit Dynamics

The dynamics for the relative motion of the chaser with respect to the target on an eccentric orbit can be described using the coordinate systems and notation shown in Figure 2.3. The location of the chaser denoted R_c is given by

$$R_c = R_t + \rho \qquad (2.1)$$

where R_t and ρ correspond to the location of the target and the relative position of the chaser spacecraft with respect to the target. These vectors ρ and R_t can be expressed in the target LVLH reference frame as

$$\rho = x i_x + y i_y + z i_z \qquad (2.2)$$

$$R_t = R i_x \qquad (2.3)$$

where x, y, and z denote the components of the relative position vector ρ along the radial, transverse, and out-of-plane directions, respectively, and R is the magnitude of the target position vector R_t. By use of kinematics, the most general equations modeling relative motion are given by the following expression

$$\ddot{\rho} = [f_c]^{LVLH} - [f_t]^{LVLH} - 2\omega \times \dot{\rho} - \omega \times \omega \times \rho - \dot{\omega} \times \rho \qquad (2.4)$$

where $[f_c]^{LVLH}$ and $[f_t]^{LVLH}$ are the external acceleration forces acting on the chaser and the target, respectively, in the LVLH frame of the target vehicle. In Equation (2.4), $(\dot{})$ and $(\ddot{})$ denote the first and second derivatives with respect to time.

An assumption in this dissertation is that the external forces arise due to two basic groups of forces defined by the following equation.

$$f = f_g + f_a + f_c + f_w \qquad (2.5)$$

i_y

i_x

i_z

Relative Orbit

i_z

Target

R_t

ρ

Chaser

R_c

i_Y

i_X
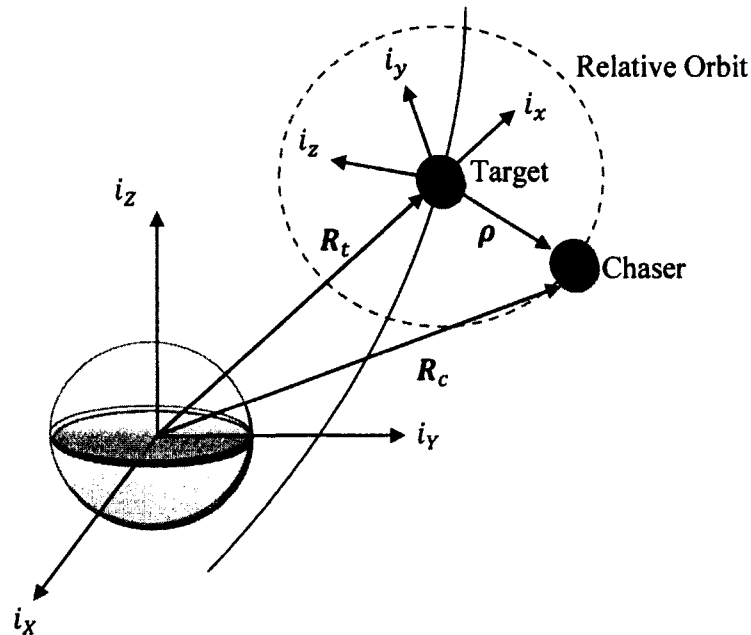
Figure 2.3 Relative Motion Coordinates

The first group of forces is due to gravitational effects, f_g, atmospheric drag, f_a, and control, f_c. Since the Earth isn't perfectly spherical, more accurate gravity models exist that take into account the Earth's irregular shape. One irregularity that has a significant influence on space missions is the Earth's bulge at the equator. This phenomenon is captured in the J_2 gravity model.[43,54] The second group of forces, f_w, is considered to be small forces caused by the gravity fields of other planets, solar pressure, or venting which also perturbs the spacecraft's motion. These small forces are grouped together and modeled as zero mean normally distributed random variables.[58]

In the literature, the most popular methods to model the spacecraft orbit are known as Cowell's method and Gauss' method.[43,54] Cowell's method is basically defined by specifying the position vector R and velocity vector V of the spacecraft in the inertial coordinate frame while Gauss' method is defined by an equivalent set of elements called

orbital elements $(a, e, i, \Omega, \omega, f)$ which correspond to the semi-major axis, eccentricity, inclination, right ascension of the ascending node, argument of periapsis, and true anomaly as shown in Figures 2.4 and 2.5. The symbols b and p denote the semi-minor axis and the semi-latus rectum of the orbit, respectively.
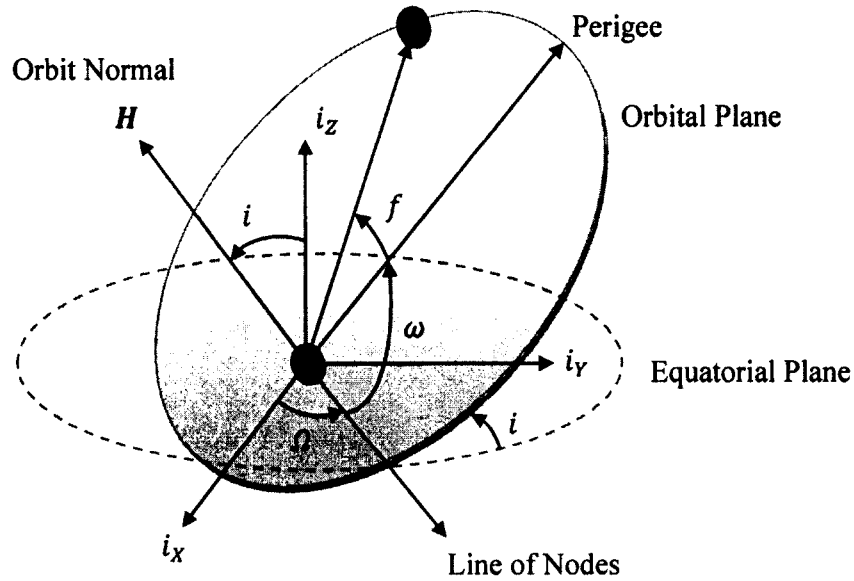
Figure 2.4 Orbital Angles
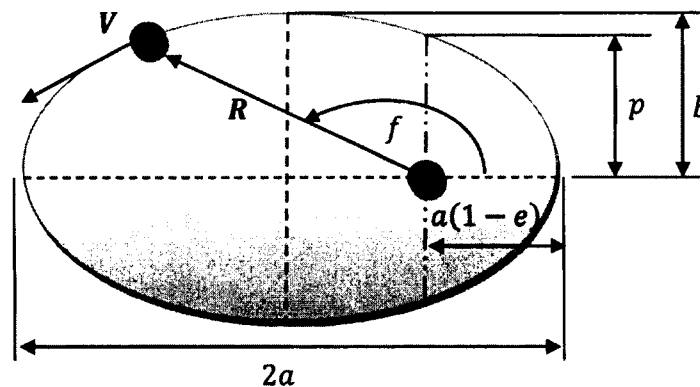
Figure 2.5 Elements in Orbital Plane

Table 2.1 summarizes the dynamic equations that are used to describe all of these methods. In this table, $[.]^I$ and $[.]^{LVLH}$ denote that the forces are defined in inertial and LVLH coordinate frames respectively; μ and $R_\oplus$ are the Earth gravitational constant and the radius of the Earth; the terms R and V refer to the magnitude of the position and velocity vectors respectively; the quantity H denotes the magnitude of the angular momentum vector defined by $\boldsymbol{H} = \boldsymbol{R} \times \boldsymbol{V}$; X, Y, and Z are the components of the spacecraft position vector; C_D is the atmospheric drag coefficient; A denotes the cross sectional area; m is the spacecraft mass; and finally, ρ is the atmospheric density. Exponential atmospheric behavior is used to model the Earth's atmospheric density. This model and its corresponding parameters are defined in Reference 43.

In order to use the generalized relative dynamic model defined by Equation (2.4), the angular velocity vector, ω, and angular acceleration vector, $\dot{\omega}$, of the LVLH frame with respect to the ECI frame, need to be determined. Table 2.2 summarizes the equations that can be used to compute these vectors. These equations are derived based on using either Cowell's method (position and velocity vectors) or Guass' method (orbital elements). In this table, the matrix T_I^{LVLH} denotes the direction cosine matrix of the LVLH coordinate frame with respect to the ECI coordinate frame. Using fundamental orbital mechanics describing planetary motion, the magnitude of the target position vector R, and the magnitude of the angular momentum vector H, can be written as

$$R = \frac{p}{1 + ec_f}, \qquad H = \sqrt{\mu p}, \qquad p = a(1 - e^2) \tag{2.6}$$

Table 2.1 Orbit Model Methods Summary

- Cowell's Method

$$\ddot{R} = f$$

$$f = f_g + f_a + f_c + f_w$$

$$f_g = a_{two-body} + a_{J_2}$$

$$a_{two-body} = -\left(\frac{\mu}{R^3}\right)R$$

$$[a_{J_2}]^I = -\frac{3}{2}J_2\frac{\mu R_\oplus^2}{R^4}\left[(1 - 5(Z/R)^2)\frac{X}{R} \quad (1 - 5(Z/R)^2)\frac{Y}{R} \quad (3 - 5(Z/R)^2)\frac{Z}{R}\right]^T$$

$$[f_a]^I = -\frac{1}{2}\frac{C_D A}{m}\rho VV$$

- Guass' Method

$$\frac{da}{dt} = \frac{2a^2}{H}\left[es_f a_x + \frac{p}{R}a_y\right]$$

$$\frac{de}{dt} = \frac{1}{H}\{ps_f a_x + [(p + R)c_f + Re]a_y\}$$

$$\frac{di}{dt} = \frac{Rc_{\omega+f}}{H}a_z$$

$$\frac{d\Omega}{dt} = \frac{Rs_{\omega+f}}{Hs_i}a_z$$

$$\frac{d\omega}{dt} = \frac{1}{He}\{-pc_f a_x + (p + R)s_f a_y\} - \frac{Rs_{\omega+f}c_i}{Hs_i}a_z$$

$$\frac{df}{dt} = \frac{H}{R^2} + \frac{1}{He}[pc_f a_x - (p + R)s_f a_y]$$

$$[a]^{LVLH} = [a_{J_2} + f_a + f_c + f_w]^{LVLH}$$

$$[a_{J_2}]^{LVLH} = -\frac{3}{2}J_2\frac{\mu R_\oplus^2}{R^4}\left[1 - 3\,s_i^2\,s_{\omega+f}^2 \quad s_i^2\,s_{2(\omega+f)}^2 \quad s_{2i}s_{(\omega+f)}\right]^T$$

$$[f_a]^{LVLH} = -\frac{1}{2}\frac{C_D A}{m}\rho V V^{LVLH}$$

$$V^{LVLH} = \frac{H}{p}[esinf \quad p/R \quad 0]^T$$

Table 2.2 LVLH Coordinate Frame Orientation

- Given Inertial Position and Velocity

$$T_I^{LVLH} = [i_x \quad i_y \quad i_z]^T$$

$$i_x = \frac{R}{R}, \qquad i_z = \frac{H}{H}, \qquad i_y = i_z \times i_x$$

$$\omega = \begin{pmatrix} R[f_z]^{LVLH}/H \\ 0 \\ H/R^2 \end{pmatrix}, \qquad \dot{\omega} = \begin{pmatrix} \dfrac{\left(\dot{R}[f_z]^{LVLH} + R[\dot{f}_z]^{LVLH}\right)H - R[f_z]^{LVLH}\dot{H}}{H^2} \\ 0 \\ \dfrac{\dot{H}R - 2H\dot{R}}{R^3} \end{pmatrix}$$

$$[f]^{LVLH} = T_I^{LVLH}[f]^I - \omega \times T_I^{LVLH}[f]^I$$

$$\dot{H} = Rf_y, \qquad \dot{R} = \frac{R \cdot V}{R}, \qquad H = R \times V$$

- Given Orbital Elements

$$T_I^{LVLH} = T^3(\omega + f)T^1(i)T^3(\Omega) = \begin{bmatrix} c_\Omega c_{\omega+f} - s_\Omega s_{\omega+f}c_i & s_\Omega c_{\omega+f} + c_\Omega s_{\omega+f}c_i & s_{\omega+f}s_i \\ -c_\Omega s_{\omega+f} - s_\Omega c_{\omega+f}c_i & -s_\Omega s_{\omega+f} + c_\Omega c_{\omega+f}c_i & c_{\omega+f}s_i \\ s_\Omega s_i & -c_\Omega s_i & c_i \end{bmatrix}$$

$$\omega = T^3(\omega+f)T^1(i)\begin{bmatrix} 0 \\ 0 \\ \dot{\Omega} \end{bmatrix} + T^3(\omega+f)\begin{bmatrix} i \\ 0 \\ 0 \end{bmatrix} + \begin{bmatrix} 0 \\ 0 \\ \dot{\omega}+\dot{f} \end{bmatrix} = \begin{pmatrix} s_{\omega+f}s_i\dot{\Omega} + c_{\omega+f}\dot{i} \\ 0 \\ c_i\dot{\Omega} + (\dot{\omega}+\dot{f}) \end{pmatrix}$$

$$T^1(\theta) = \begin{bmatrix} 1 & 0 & 0 \\ 0 & c_\theta & s_\theta \\ 0 & -s_\theta & c_\theta \end{bmatrix}, \quad T^2(\theta) = \begin{bmatrix} c_\theta & 0 & -s_\theta \\ 0 & 1 & 0 \\ s_\theta & 0 & c_\theta \end{bmatrix}, \quad T^3(\theta) = \begin{bmatrix} c_\theta & s_\theta & 0 \\ -s_\theta & c_\theta & 0 \\ 0 & 0 & 1 \end{bmatrix}$$

2.4 Approximate Linear Models

Three approximate linear models are presented for relative motion dynamics, which assume certain chaser-target architectures. All of these models are mainly based on a linear approximation of Equation (2.4). In the development, the first model takes into account the gravitational and aerodynamic forces while the two other models consider only the two-body main gravitational force. Analytical expressions for propagating relative motion have been developed and the state transition matrix is provided for the solution of the linearized relative motion.

2.4.1 Linear Time Varying Relative Model (LTV)

In this section, a linear time varying high fidelity model is obtained to describe the relative motion dynamics. This model is derived based on two main assumptions. The first assumption is that the relative distance between the chaser and the target vehicles is much less than the target orbital radius. Secondly, it is assumed that the main disturbance accelerations that affect both vehicles are the gravitational acceleration and the atmospheric drag acceleration. Based on these assumptions, all terms mentioned in the general relative dynamic expression (Equation (2.4)) are expanded considering only first order terms to obtain the new proposed model. Table 2.3 summarizes the procedures that have been followed to obtain this model. In this table, the linear time varying model reduces to the following form

$$\dot{x} = Ax \tag{2.7}$$

where x is the state vector. This model can be used to approximate the time varying state transition matrix ϕ, by expanding the time invariant exponential matrix solution in a Taylor series to fourth-order as follows

$$\phi = e^{A\Delta t} \approx I + A\Delta t + \frac{A^2 \Delta t^2}{2!} + \frac{A^3 \Delta t^3}{3!} + \frac{A^4 \Delta t^4}{4!} \tag{2.8}$$

where I is the 6×6 unity matrix and Δt is the difference between the current time, t, and initial time, t_0. ϕ is used in the next chapters as a part of the extended Kalman filter to propagate the states forward in time and to compute the filter parameters.

2.4.2 Analytical Solution to TH Relative Motion

The primary force to be considered here is the main gravitational force of the attracting body, which is the two-body force, and all other perturbation forces are neglected. In this case, the relative model is reduced to

Table 2.3 Relative Orbit Model Summary

- Relative Nonlinear Model

$$\ddot{\rho} = [\mathbf{f}_c]^{\text{LVLH}} - [\mathbf{f}_t]^{\text{LVLH}} - 2\omega \times \dot{\rho} - \omega \times \omega \times \rho - \dot{\omega} \times \rho$$

- Linear Time Varying Model

$$-2\omega \times \dot{\rho} - \omega \times \omega \times \rho - \dot{\omega} \times \rho = \begin{bmatrix} \omega_z^2 & \dot{\omega}_z & -\omega_x\omega_z & 0 & 2\omega_z & 0 \\ -\dot{\omega}_z & \omega_x^2+\omega_z^2 & \dot{\omega}_x & -2\omega_z & 0 & 2\omega_x \\ -\omega_x\omega_z & -\dot{\omega}_x & \omega_x^2 & 0 & -2\omega_x & 0 \end{bmatrix} \begin{pmatrix} x \\ y \\ z \\ \dot{x} \\ \dot{y} \\ \dot{z} \end{pmatrix}$$

$$[\mathbf{f}_c]^{\text{LVLH}} - [\mathbf{f}_t]^{\text{LVLH}} \approx \left[\Delta\mathbf{f}_g + \Delta\mathbf{f}_a\right]^{\text{LVLH}}$$

$$[\Delta a_{two-body}]^{\text{LVLH}} \approx \frac{\mu}{R^3}\begin{pmatrix} 2 & 0 & 0 \\ 0 & -1 & 0 \\ 0 & 0 & -1 \end{pmatrix}\begin{pmatrix} x \\ y \\ z \end{pmatrix}$$

$$[\Delta a_{J_2}]^{\text{LVLH}} \approx -\frac{3}{2}J_2\frac{\mu R_\oplus^2}{R^5}\begin{bmatrix} -4(1-3i_{x_3}^2) & -8i_{x_3}i_{y_3} & -8i_{x_3}i_{z_3} \\ -8i_{x_3}i_{y_3} & 1-7i_{x_3}^2+2(1-i_{z_3}^2) & 2i_{y_3}i_{z_3} \\ -8i_{x_3}i_{z_3} & 2i_{y_3}i_{z_3} & 3-5i_{x_3}^2-2(1-i_{z_3}^2) \end{bmatrix}\begin{pmatrix} x \\ y \\ z \end{pmatrix}$$

$$[\Delta\mathbf{f}_a]^{\text{LVLH}} \approx \begin{bmatrix} C_c\omega_z R & 0 & 0 \\ 0 & C_c\omega_z R & 0 \\ 0 & 0 & C_c\omega_z R \end{bmatrix}\begin{pmatrix} \dot{x} \\ \dot{y} \\ \dot{z} \end{pmatrix}$$

$$\dot{x} = Ax, \quad x = [x \quad y \quad z \quad \dot{x} \quad \dot{y} \quad \dot{z}]^{\text{T}}, \quad A = \begin{bmatrix} A_{11} & A_{12} \\ A_{21} & A_{22} \end{bmatrix}$$

$$A_{11} = 0_{3\times 3}, \quad A_{12} = I_{3\times 3}, \quad A_{22} = \begin{bmatrix} C_c\omega_z R & 2\omega_z & 0 \\ -2\omega_z & C_c\omega_z R & 2\omega_x \\ 0 & -2\omega_x & C_c\omega_z R \end{bmatrix}$$

$$A_{21}(:,1:2) = \begin{bmatrix} \omega_z^2 + 2C_1 - 4C_2(1-3i_{x_3}^2) & \dot{\omega}_z - 8C_2i_{x_3}i_{y_3}-C_c\omega_z^2 R \\ -\dot{\omega}_z - 8C_2i_{x_3}i_{y_3} + C_c\omega_z^2 R & (\omega_x^2+\omega_z^2) - C_1 + C_2\left(1-7i_{x_3}^2+2(1-i_{z_3}^2)\right) \\ -\omega_x\omega_z - 8C_2i_{x_3}i_{z_3} & -\dot{\omega}_x+2C_2i_{y_3}i_{z_3} + C_c\omega_x\omega_z R \end{bmatrix}$$

$$A_{21}(:,3) = \begin{bmatrix} -\omega_x\omega_z - 8C_2i_{x_3}i_{z_3} \\ \dot{\omega}_x + 2C_2i_{y_3}i_{z_3} - C_c\omega_x\omega_z R \\ \omega_x^2 - C_1 + C_2\left(3-5i_{x_3}^2-2(1-i_{z_3}^2)\right) \end{bmatrix}$$

$$C_1 = \frac{\mu}{R^3}, \quad C_2 = -\frac{3}{2}J_2\frac{\mu R_\oplus^2}{R^5}, \quad C_c = -\frac{1}{2}\frac{C_D A}{m}\rho$$

$$\ddot{x} - (\omega_z^2 + 2C_1)x - \dot{\omega}_z y - 2\omega_z \dot{y} = 0$$

$$\ddot{y} - (\omega_z^2 - C_1)y + \dot{\omega}_z x + 2\omega_z \dot{x} = 0 \tag{2.9}$$

$$\ddot{z} + C_1 z = 0$$

and

$$\frac{da}{dt} = \frac{de}{dt} = \frac{di}{dt} = \frac{d\Omega}{dt} = \frac{d\omega}{dt} = 0, \quad \frac{df}{dt} = \frac{H}{R^2} \tag{2.10}$$

where

$$\omega_z = \frac{n(1 + ec_f)^2}{(1 - e^2)^{\frac{3}{2}}}, \quad \dot{\omega}_z = \frac{-2\mu es_f}{R^3}, \quad n = \sqrt{\frac{\mu}{a^3}} \tag{2.11}$$

When f is used as the free variable, the relative equations of motion Equation (2.9) can be transformed using the relationships

$$(\dot{\cdot}) = (\cdot)'\dot{f}, \quad (\ddot{\cdot}) = (\cdot)''\dot{f}^2 + \dot{f}\dot{f}'(\cdot)' \tag{2.12}$$

$$\rho_n = \frac{\rho}{R} = \frac{1 + ec_f}{a(1 - e^2)}\rho = \begin{bmatrix} x_n \\ y_n \\ z_n \end{bmatrix}$$

$$\rho_n' = \frac{1 + ec_f}{a(1 - e^2)}\rho' - \frac{es_f}{a(1 - e^2)}\rho \tag{2.13}$$

$$\rho_n'' = \frac{1 + ec_f}{a(1 - e^2)}\rho'' - \frac{2es_f}{a(1 - e^2)}\rho' - \frac{ec_f}{a(1 - e^2)}\rho$$

where x_n, y_n, and z_n are the components of the normalized relative position using R as the normalization factor, and $(\cdot)'$ and $(\cdot)''$ denote the derivatives with respect to f. With these transformations, the set of linear time varying equations describing the relative motion for a target eccentric orbit can be written as

$$x_n'' - 2y_n' - \frac{3x_n}{1 + ec_f} = 0$$

$$y_n'' + x_n' = 0$$

$$z_n'' + z_n = 0$$

(2.14)

These homogenous relative motion equations are known as the Tschauner-Hempel equations, which are normalized for both position and velocity. The TH model is thus concisely written as three second-order, linear ordinary differential equations with periodic coefficients, and is valid for all eccentricities of the reference orbit. An early attempt to solve the TH equations can be found in Reference 59, in which e is treated as a small parameter. References 21 and 60 developed analytical solutions that are valid for all eccentricities, in terms of a special integral known as Lawden's integral.

Equation (2.14) has the following general homogenous solution for the normalized relative position and velocity components

$$
\begin{bmatrix} x_n \\ y_n \\ z_n \\ x_n' \\ y_n' \\ z_n' \end{bmatrix} =
\begin{bmatrix}
c_f(1 + ec_f) & s_f(1 + ec_f) & \frac{2}{\eta^2}\left[1 - \frac{3e}{2\eta^3}s_f(1 + ec_f)K(f)\right] & 0 & 0 & 0 \\
-s_f(2 + ec_f) & c_f(2 + ec_f) & -\frac{3}{\eta^5}(1 + ec_f)^2 K(f) & 1 & 0 & 0 \\
0 & 0 & 0 & 0 & c_f & s_f \\
-(s_f + es_{2f}) & (c_f + ec_{2f}) & -\frac{3e}{\eta^2}\left[\frac{s_f}{(1 + ec_f)} + \frac{1}{\eta^3}(c_f + ec_{2f})K(f)\right] & 0 & 0 & 0 \\
-(2c_f + ec_{2f}) & -(2s_f + es_{2f}) & -\frac{3}{\eta^2}\left[1 - \frac{e}{\eta^3}(2s_f + es_{2f})K(f)\right] & 0 & 0 & 0 \\
0 & 0 & 0 & 0 & -s_f & c_f
\end{bmatrix}
\begin{bmatrix} c_1 \\ c_2 \\ c_3 \\ c_4 \\ c_5 \\ c_6 \end{bmatrix}
$$

$$
\begin{bmatrix} c_1 \\ c_2 \\ c_3 \\ c_4 \\ c_5 \\ c_6 \end{bmatrix} =
\begin{bmatrix}
-\frac{3}{\eta^2}(e + c_{f_0}) & 0 & 0 & -\frac{1}{\eta^2}s_{f_0}(1 + ec_{f_0}) & -\frac{1}{\eta^2}(2c_{f_0} + e + ec_{f_0}^2) & 0 \\
-\frac{3}{\eta^2}\frac{s_{f_0}(1 + ec_{f_0} + e^2)}{(1 + ec_{f_0})} & 0 & 0 & \frac{1}{\eta^2}(c_{f_0} - 2e + ec_{f_0}^2) & -\frac{1}{\eta^2}s_{f_0}(2 + ec_{f_0}) & 0 \\
(2 + 3ec_{f_0} + e^2) & 0 & 0 & es_{f_0}(1 + ec_{f_0}) & (1 + ec_{f_0})^2 & 0 \\
-\frac{1}{\eta^2}(2 + ec_{f_0})\frac{3es_{f_0}}{(1 + ec_{f_0})} & 1 & 0 & -\frac{1}{\eta^2}(2 + ec_{f_0})(1 - ec_{f_0}) & -\frac{1}{\eta^2}(2 + ec_{f_0})es_{f_0} & 0 \\
0 & 0 & c_{f_0} & 0 & 0 & -s_{f_0} \\
0 & 0 & s_{f_0} & 0 & 0 & c_{f_0}
\end{bmatrix}
\begin{bmatrix} x_{n_0} \\ y_{n_0} \\ z_{n_0} \\ x_{n_0}' \\ y_{n_0}' \\ z_{n_0}' \end{bmatrix}
$$

(2.15)

where

$$\eta = \sqrt{1 - e^2}, \quad K(f) = n\Delta t = (E - e\sin E) - (E_0 - e\sin E_0)$$

(2.16)

$$\Delta t = t - t_0, \quad tan\frac{E}{2} = \sqrt{\frac{1-e}{1+e}} tan\frac{f}{2} \qquad (2.17)$$

Note the solution requires the use of the target eccentric anomaly E computed from time t, which in turn leads to true anomaly f. In Equation (2.15), c_i denotes an integration constant determined from the initial conditions $\{x_{n_0}, y_{n_0}, z_{n_0}, x'_{n_0}, y'_{n_0}, z'_{n_0}\}$ corresponding to the initial true anomaly f_0. Let the initial conditions be denoted by vector x_{n_0}. Then it can be shown that the state transition matrix for the TH equations is easily formulated by

$$x_n(f) = \phi(f, f_0)x_{n_0} \qquad (2.18)$$

so the state transition matrix is thus defined as

$$\phi(f, f_0) = L(f)M(f_0) = \begin{bmatrix} \phi_{\rho\rho}(f, f_0) & \phi_{\rho\rho'}(f, f_0) \\ \phi_{\rho'\rho}(f, f_0) & \phi_{\rho'\rho'}(f, f_0) \end{bmatrix} \qquad (2.19)$$

where matrices $L(f)$ and $M(f_0)$ are defined from Equation (2.15). When combining Equations (2.13), (2.15) and (2.18), the linearized relative motion response dynamics with respect to an eccentric orbit can be expressed in the time frame as

$$\rho(t) = \phi_{\rho\rho}(t, t_0)\rho_0 + \phi_{\rho\dot{\rho}}(t, t_0)\dot{\rho}_0$$
$$\dot{\rho}(t) = \phi_{\dot{\rho}\rho}(t, t_0)\rho_0 + \phi_{\dot{\rho}\dot{\rho}}(t, t_0)\dot{\rho}_0 \qquad (2.20)$$

where

$$\phi_{\rho\rho}(t, t_0) = \frac{\{A_0\phi_{\rho\rho}(f, f_0) + B_0\phi_{\rho\rho'}(f, f_0)\}}{A}$$

$$\phi_{\rho\dot{\rho}}(t, t_0) = \frac{C_0\phi_{\rho\rho'}(f, f_0)}{A}$$

$$\phi_{\dot{\rho}\rho}(t, t_0) = \frac{\left\{\left(A_0\phi_{\rho'\rho}(f, f_0) + B_0\phi_{\rho'\rho'}(f, f_0)\right) - B\phi_{\rho\rho}(t, t_0)\right\}}{C} \qquad (2.21)$$

$$\phi_{\dot{\rho}\dot{\rho}}(t, t_0) = \{C_0\phi_{\rho'\rho'}(f, f_0) - B\phi_{\rho\dot{\rho}}(t, t_0)\}/C$$

and

$$A = \frac{1 + ec_f}{a(1 - e^2)}, \quad B = \frac{-es_f}{a(1 - e^2)}, \quad C = \frac{A}{f} \tag{2.22}$$

2.4.3 Analytical Solution to CW Relative Motion

If the target satellite orbit is assumed to be circular $(e = 0)$, then the relative equations of motion (Equation (2.9)) reduce to the simple form known as Clohessy-Wiltshire equations.[4]

$$\ddot{x} - 3n^2x - 2n\dot{y} = 0$$

$$\ddot{y} + 2n\dot{x} = 0 \tag{2.23}$$

$$\ddot{z} + n^2z = 0$$

These equations of motion are valid only if the target orbit is circular and the relative distances are small compared with the target orbit radius. The simple form of the differential equations in Equation (2.23) allows them to analytically integrate to find closed form solutions to the relative equations of motion. The state transition matrix for the CW model has been determined to be

$$\phi(t, t_0) = \begin{bmatrix} 4 - c_{n\Delta t} & 0 & 0 & \frac{1}{n}s_{n\Delta t} & \frac{2}{n}(1 - c_{n\Delta t}) & 0 \\ 6(s_{n\Delta t} - n\Delta t) & 1 & 0 & -\frac{2}{n}(1 - c_{n\Delta t}) & \frac{1}{n}(4s_{n\Delta t} - 3n\Delta t) & 0 \\ 0 & 0 & c_{n\Delta t} & 0 & 0 & \frac{1}{n}s_{n\Delta t} \\ 3ns_{n\Delta t} & 0 & 0 & c_{n\Delta t} & 2s_{n\Delta t} & 0 \\ -6n(1 - c_{n\Delta t}) & 0 & 0 & -2s_{n\Delta t} & 4c_{n\Delta t} - 3 & 0 \\ 0 & 0 & -ns_{n\Delta t} & 0 & 0 & c_{n\Delta t} \end{bmatrix} \tag{2.24}$$

Similar to the TH model, this matrix can be used to propagate the relative orbit forward in time, given the initial relative orbit (Equation (2.20)) .

2.4.4 TH Numerical Simulation

To verify the exactness of Equation (2.20), the solution is compared with the numerical solution of the nonlinear equations. The nonlinear solution was obtained via numerical integration of the relative model of target and chaser in the LVLH coordinate system and the relative state vector is evaluated in the target reference frame. Simulation initial conditions are summarized in Table 2.4 for motion about the Earth. Simulation results for two cases of $e = 0$ and 0.5 were considered.

Table 2.4 Simulation Initial Conditions

Parameter	Value
Target Eccentricity	0 and 0.5
Target Perigee Height	500 km
Target Inclination	0 deg
Target Argument of Perigee	0 deg
Target True Anomaly	0 deg
Target Ascending Node	0 deg
Chaser Initial Relative Position	[-0.1 -0.1 -0.1] km
Chaser Initial Relative Velocity	[-0.0001 0.0001 -0.0001] km/s

By using the Matlab/Simulink environment, a Simulink model was designed based on the block diagram shown in Figure 2.6. The purpose of this model is to compare the analytical TH model and the nonlinear relative model for a general orbit, either circular or elliptic. Basically, this diagram consists of two parts. The first part is based on modeling the relative motion using the nonlinear equations in the LVLH target coordinate frame (Equation (2.4) considering only the two-body gravitational forces for both target

and chaser vehicles) while the second part is based on the closed form analytical solution of TH model (see Equation (2.20)).

Figures 2.7 and 2.8 show the error between nonlinear numerical and linear analytical solutions in the radial, transverse, and normal directions for a chaser with respect to a target in low Earth orbit. Two types of target orbits will be considered and simulation will be carried out for two orbital periods. First, in the circular orbit case $e = 0$, Figure 2.7 presents the error in relative motion (radially, transversely, and normally) between the numerical and analytical solutions during simulation over time. In addition, in-plane and out-of-plane motions of the chaser with respect to the target are also shown. It can be seen that the relative errors increase with time, but they are very small compared to the relative distance itself. Second, in the elliptic orbit case $e = 0.5$, simulation results are presented in Figure 2.8. It can be seen from the results that the analytical solution is accurate as long as the main assumption of linearization $|\rho| \ll |R|$ is satisfied. Comparing Figures 2.7 and 2.8 shows the reference orbit eccentricity has a great effect on the propagation of the relative trajectory motion.
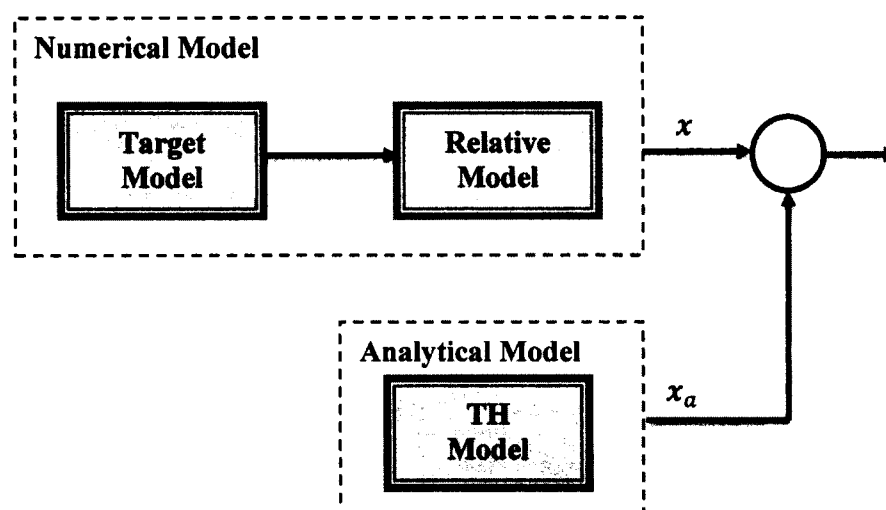

Figure 2.6 Nonlinear and Analytical TH Model Block Diagram
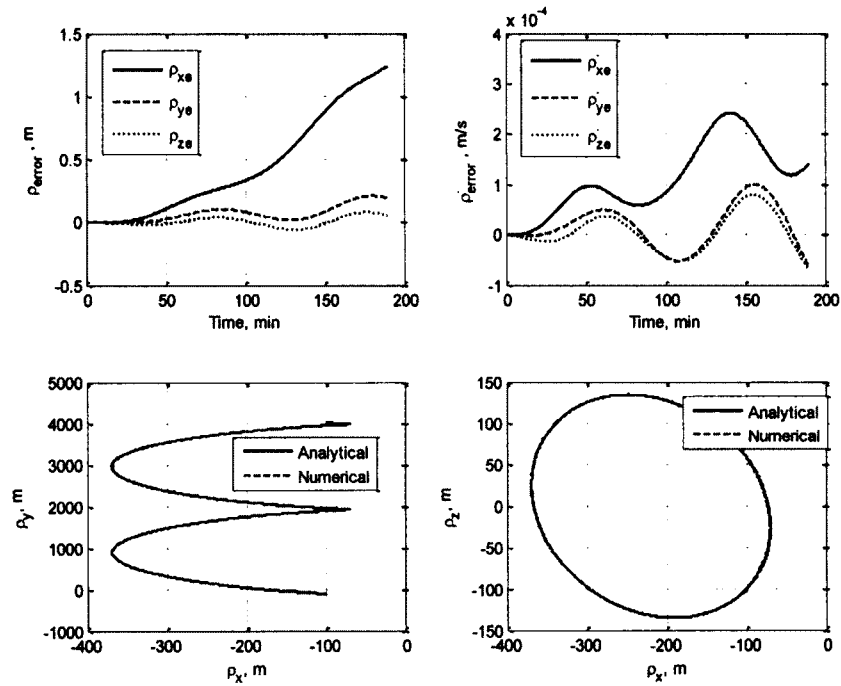
Figure 2.7 Relative Motion Analytical and Numerical Solution Errors for _e_ = 0
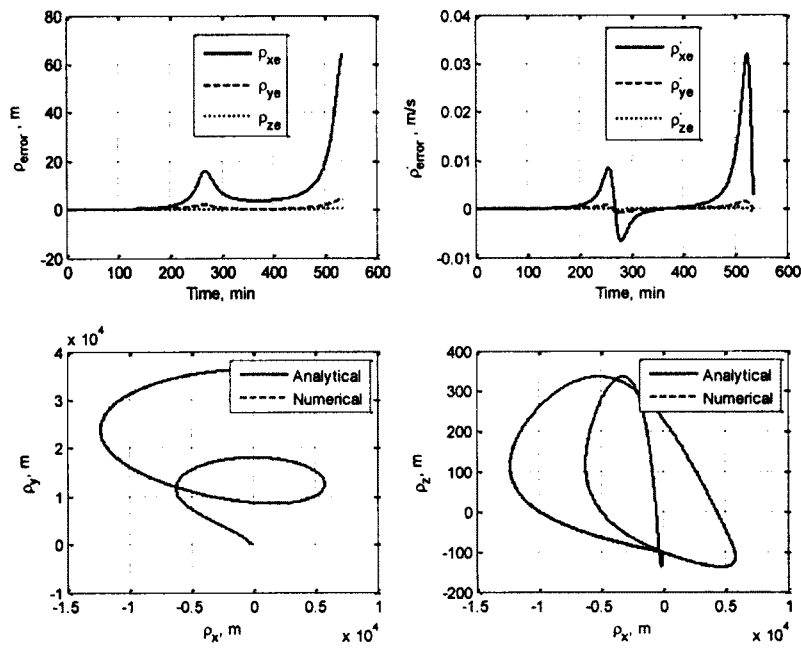
Figure 2.8 Relative Motion Analytical and Numerical Solution Errors for _e_ = 0.5

2.5 TH Based Multipulse Glideslope Transfer

By use of the TH analytical solution as given by Equation (2.20) and utilizing Figure 2.9, the velocity $\dot{\rho}_0^+$ required at ρ_0 and time t_0 to arrive at a specific location, ρ_T , in a period of time T, is obtained from Equation (2.20).

$$\dot{\rho}_0^+ = \phi_{\rho\dot{\rho}}^{-1}(T, 0)\left(\rho_T - \phi_{\rho\rho}(T, 0)\rho_0\right) \tag{2.25}$$

The initial velocity at ρ_0 is changed instantaneously to $\dot{\rho}_0^+$ by adding an incremental velocity equal to

$$\Delta V_0 = \dot{\rho}_0^+ - \dot{\rho}_0^- \tag{2.26}$$

where $\dot{\rho}_0^- = \dot{\rho}_0$ is the current initial velocity. The arrival velocity $\dot{\rho}_T$ occurring at $\rho(T) = \rho_T$ when $t = T$ is also given by Equation (2.20).

$$\dot{\rho}_T = \phi_{\dot{\rho}\rho}(T, 0)\rho_0 + \phi_{\dot{\rho}\dot{\rho}}(T, 0)\dot{\rho}_0^+ \tag{2.27}$$

If the chaser is commanded to arrive at the specified station at $t = T$ with zero relative velocity, the arrival velocity $\dot{\rho}_T$ must be counteracted by adding a pulse ΔV_T equal to

$$\Delta V_T = -\dot{\rho}_T \tag{2.28}$$

so that, to effect docking, the net relative velocity at ρ_T is zero.
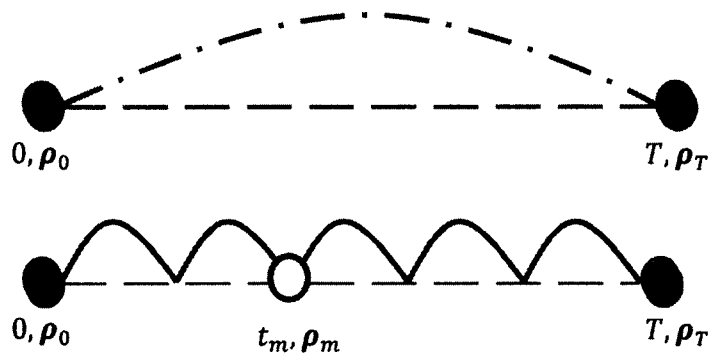
Figure 2.9 Single and Multipulse Glideslope Transfer

References 35 and 57 present several profiles for a chaser to approach or retreat from a target vehicle. During these flight profiles, thrust activity near the target needs to

be minimized to avoid plume contamination of the surfaces of the target vehicle. Furthermore, as a safety precaution, the relative speed should be small enough to avoid an uncontrolled collision. These proximity guidance schemes are discussed next.

2.5.1 Inbound Glideslope

First, an inbound approach along a specified glideslope is considered. As shown in Figure 2.10, the chaser vehicle is required to arrive at $\rho = \rho_T$ in a transfer time T with a velocity specified hereafter. A straight line from ρ_0 to ρ_T, denoted by the vector r, is the most natural commanded path for this transfer. At any instant of time, vector r can be expressed as $r(t) = \rho(t) - \rho_T = r\hat{u}_r$, where r and $\hat{u}_r$ are the magnitude and unit direction of the vector respectively. The following linear relationship between r and $\dot{r}$ is proposed for the inbound transfer

$$\dot{r} = \gamma r + \lambda \tag{2.29}$$

where γ and λ are constants to be determined. The boundary conditions for r and $\dot{r}$, at $t = 0$ and at $t = T$, are

$$\begin{aligned} t = t_0 : \quad & r = r_0 \;, & \dot{r} = \dot{r}_0 < 0 \\ t = T : \quad & r = 0 \;, & \dot{r} = \dot{r}_T < 0 \end{aligned} \tag{2.30}$$

The solution for r is

$$r = c_{r_1} e^{c_{r_2} t} + c_{r_3} \tag{2.31}$$

where c_{r_1}, c_{r_2}, and c_{r_3} are three constants of integration related to γ and λ. If the transfer time T is also considered an unknown constant, the four unknowns can be determined by applying the boundary conditions in Equation (2.30). Because it is more useful to specify T, the boundary condition $\dot{r}_T$ is relaxed and only the other three are used to compute c_{r_1},

c_{r_2}, and c_{r_3}. The initial rate condition $\dot{r}_0$ can be chosen or specified to achieve certain trajectory requirements.
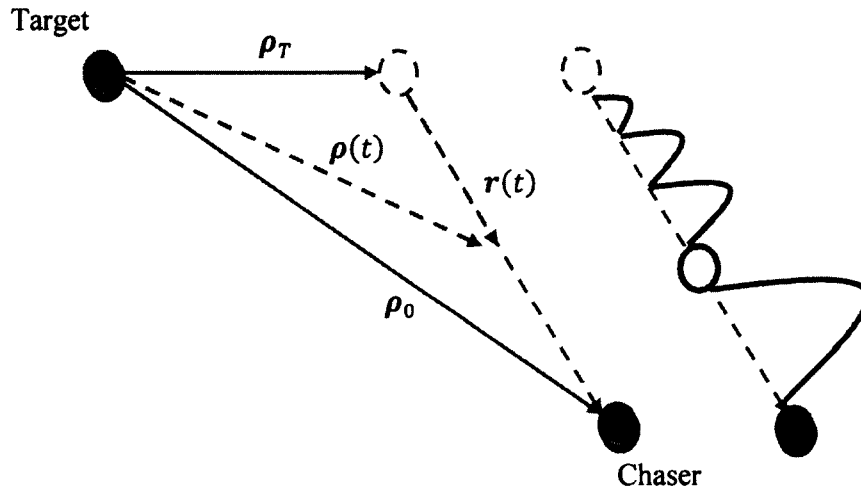
Figure 2.10 Inbound Glideslope

For a two-impulse transfer, Equation (2.31) is used to compute $r(t)$, from which $\rho(t)$ is generated for a given ρ_T (see Figure 2.10). Equations (2.25)-(2.28) are then used to implement the impulses. Note the exponential approach along the rectilinear path is an idealization; the actual path of the chaser is governed by Equation (2.20) which will not yield the exponential-rectilinear trajectory, except at the boundary conditions where an exact match will occur. This path difference results from the linearized gravity force model in the TH equations which results in a curvilinear path. To keep the path deviation small, as well as the required velocity impulses, a multipulse strategy is considered.

Let the number of thruster firings to travel from $\rho_0(r = r_0)$ to $\rho_T(r = 0)$ in time T be N and the uniform interval between any two successive pulses be $\Delta t = T/N$. The thrusters are thus fired at time $t_m = m\Delta t$, and the mth pulse pushes the chaser from ρ_m to ρ_{m+1}, where

$$\boldsymbol{\rho}_m = \boldsymbol{\rho}_T + r_m \hat{u}_r$$

$$r_m = r(t_m) = c_{r_1} e^{c_{r_2} t_m} + c_{r_3}$$

(2.32)

Following Equations (2.25)-(2.28), the required incremental velocity can be calculated in such a way to move the chaser toward any specified location nearby the target by applying the mth pulse.

2.5.2 Outbound Glideslope

Now consider an outbound approach along the specified glideslope. Figure 2.11 shows the geometry of this glideslope. The chaser in this case needs to be moved away from the target from initial relative position $\boldsymbol{\rho}_0(r = 0)$ to $\boldsymbol{\rho}_T(r = r_T)$ in T time. The boundary conditions for this glideslope path $r(t) = \rho(t) - \rho_o = r\hat{u}_r$ are defined as

$$t = t_0 : \quad r = 0 , \quad \dot{r} = \dot{r}_0 > 0$$

$$t = T : \quad r = r_T , \quad \dot{r} = \dot{r}_T > 0$$

(2.33)
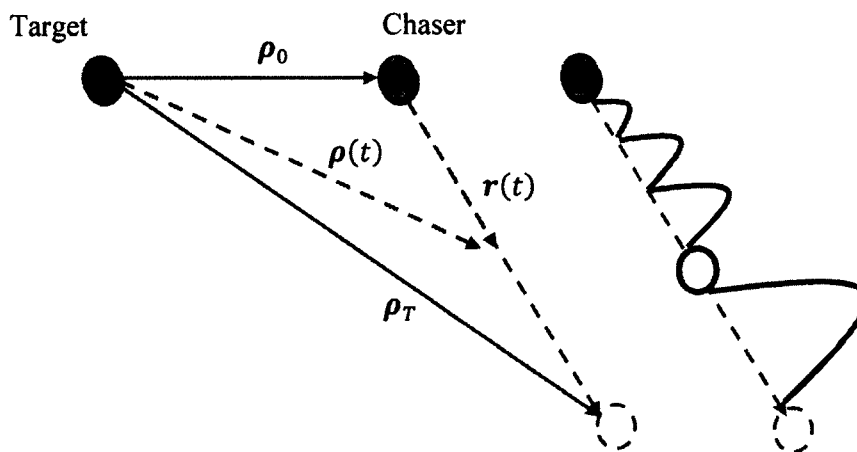
Figure 2.11 Outbound Glideslope

The algorithm to transfer the vehicle from ρ_0 to ρ_T is similar to that for the inbound glideslope. N thruster firings effect the transfer, as before, with the mth firing taking place at ρ_m, where

$$\rho_m = \rho_0 + r_m \hat{u}_r$$
$$r_m = c_{r_1} e^{c_{r_2} t_m} + c_{r_3}$$

(2.34)

Constants of integration c_{r_1}, c_{r_2}, and c_{r_3} are determined by applying the boundary conditions. Similarly, the calculation of incremental velocities for each firing proceeds as in Equations (2.25)-(2.28).

2.5.3 Simple Flyaround (Circular and Elliptic)

In Reference 36, the initial condition for a periodic natural elliptical flyaround is specified as follows.

$$\frac{\dot{y}(0)}{x(0)} = -\frac{n(2+e)}{(1+e)^{1/2}(1-e)^{3/2}}$$

(2.35)

Under this initial condition, the chaser will continue to travel around the target with an elliptical periodic trajectory lying in the target orbital plane. Sometimes according to the rendezvous scenario, it is required for the chaser to perform a flyaround in a circular in-plane orbit as shown in Figure 2.12. If the circular flyaround of radius ρ_c has period T and the circumnavigation is effected with N pulses, then the angle traveled between two pulses m and $m + 1$, $m = 0,1, ..., N - 1$, is $\Delta\theta = 2\pi/N$. At $t = 0$, the chaser is at angle θ_0, subsequently, the angle θ varies linearly as $\theta = \theta_0 + 2\pi t/T$, and the commanded location of the chaser is

$$x = \rho_c c_\theta$$
$$y = -\rho_c s_\theta$$

(2.36)
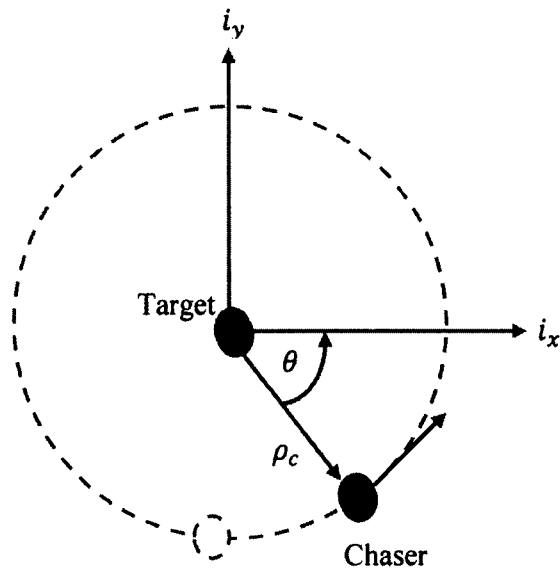
Figure 2.12 In-Plane Circular Flyaround

The mth pulse takes place at $\theta_m = \theta_0 + m\Delta\theta$, and the corresponding chaser location is defined by

$$\rho_m = \rho_c[c_{\theta_m} \quad -s_{\theta_m} \quad 0]^T \tag{2.37}$$

It is straightforward to calculate the departure velcoity $\dot{\rho}_m^+$ at ρ_m and the arrival velocity $\dot{\rho}_{m+1}^-$ at ρ_{m+1} using Equations (2.25)-(2.28).

2.5.4 Numerical Examples

To demonstrate the open loop guidance transfer of the chaser to approach, to flyaround, and to depart from the target vehicle in any Keplerian orbit, either circular or elliptic, the following examples are presented. Simulation will be presented for previous types of glideslope trajectories considering an eccentric orbit of the target.

Figure 2.13 shows the block diagram that is used to design the open loop guidance and control system of relative motion based on the closed form solution of the TH model. The TH model will be used in propagation of the relative state vector and in

the design of guidance and control algorithms. In this figure, the guidance and control block is used to compute the desired relative vector, x_d, which is based upon glideslope type (inbound, outbound or flyaround), and the required relative velocity change vector ΔV (see Equations (2.25)-(2.28)) that is used to move the chaser from its current location to the desired one. In order to check the accuracy of ΔV in moving the chaser to its intended location, the same vector increment was used in both the nonlinear and TH models. The error between relative motion simulation based on the numerical model (x) and relative motion based on the analytical propagation (x_a) is compared through different scenarios.

Figure 2.13 Relative Motion Guidance and Control Based on TH Model

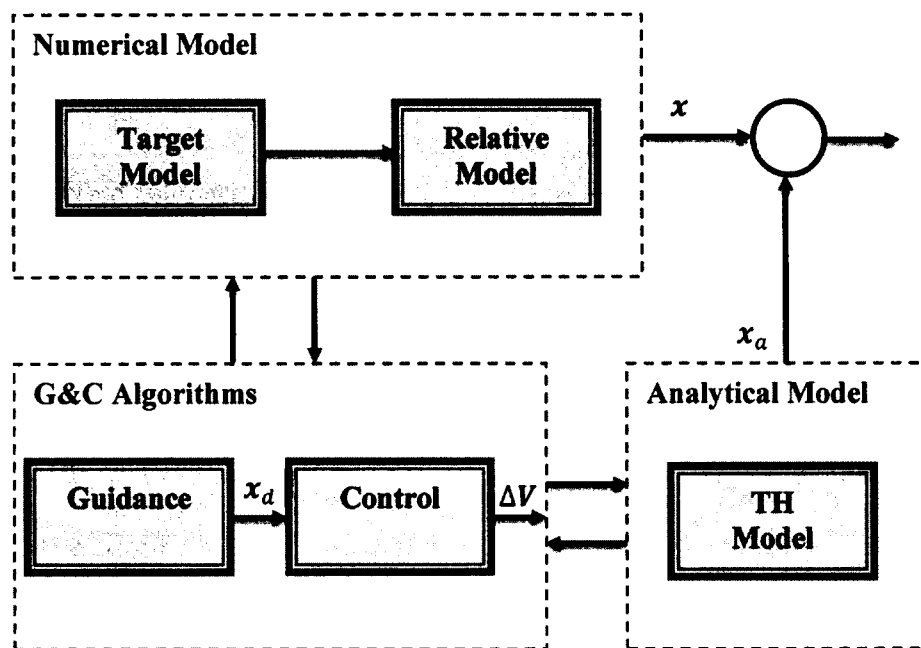The initial conditions for simulation are listed in Tables 2.5 and 2.6. First, the inbound glideslope is shown in Figures 2.14 and 2.15. In these figures, the chaser starts to approach the target vehicle from 500m behind and 100m below the target and is guided either by one pulse, as shown in Figure 2.14, or by 10 pulses as shown in Figure 2.15,

during a 20 minute time interval. At the end of this time, the chaser will be 100m behind the target. These figures also show the relative motion and relative velocity of the chaser with respect to the target and the required ΔV to achieve this trajectory maneuver. In both Figures 2.14 and 2.15, although the number of pulses is different, the chaser was able to reach its destination. Increasing the number of pulses gave more control over the trajectory, but with the price of increasing the total ΔV, which means increasing fuel consumption.

Table 2.5 Target Orbit

Parameter	Value
Target Eccentricity	0.1
Target Semi-Major Axis	6723.2576 km
Target Inclination	51.6467 deg
Target Argument of Perigee	188. 0147 deg
Target True Anomaly	174.3022 deg
Target Ascending Node	270.0882 deg

Second, the flyaround glideslope has been demonstrated through Figures 2.16 and 2.17. The chaser performs a 100m circular flyaround affected by 4 pulses as in Figure 2.16 or 20 pulses as in Figure 2.17 over a period of 20 minutes. It is noted from these figures that, as the number of pulses increase, the chaser was able to circumnavigate the target along an almost perfect circle. Third, the outbound glideslopes are shown in Figures 2.18 and 2.19. In these figures, the chaser starts to depart from 100m behind the target with 1 pulse as in Figure 2.18 or 10 pulses as in Figure 2.19 in a period of 20 minutes leading to a new location 1000m behind the target. The same conclusion can be

written about the effect of number of pulses over the trajectory as in the inbound glideslope case.

In all of the above figures, there are humps in the trajectory during inbound, outbound, and flyaround glideslope maneuvers. These humps are multipulse segmented deviations from the idealized rectilinear and circular glideslopes. Depending on the available fuel and the level of accuracy to control the glideslope trajectory, the number of pulses can be specified. In all of the above glideslopes, the overall performance of the rendezvous and proximity guidance is satisfactory.

Table 2.6 Glideslope Simulation Initial Conditions

Parameter	Value
Simulation Step	0.1 s
Inbound Chaser Relative Initial Position	[-0.1 -0.5 -0.1] km
Inbound Chaser Relative Initial Velocity	[-0.0001 0.0001 -0.0001] km/s
Inbound Number of Pulses	1,10
Inbound Transfer Time	20 min
Circular Chaser Relative Initial Position	[0 -0.1 0] km
Circular Chaser Relative Initial Velocity	[0 0 0] km/s
Circular Number of Pulses	4,20
Circular Transfer Time	20 min
Outbound Chaser Relative Initial Position	[0 -0.1 0] km
Outbound Chaser Relative Initial Velocity	[0 0 0] km/s
Outbound Number of Pulses	1,10
Outbound Transfer Time	20 min

Figure 2.14 Relative Motion Analytical Single Pulse Inbound Glideslope

Figure 2.15 Relative Motion Analytical Multipulse Inbound Glideslope

Figure 2.16 Relative Motion Analytical Four Pulse Flyaround Glideslope

Figure 2.17 Relative Motion Analytical Twenty Pulse Flyaround Glideslope
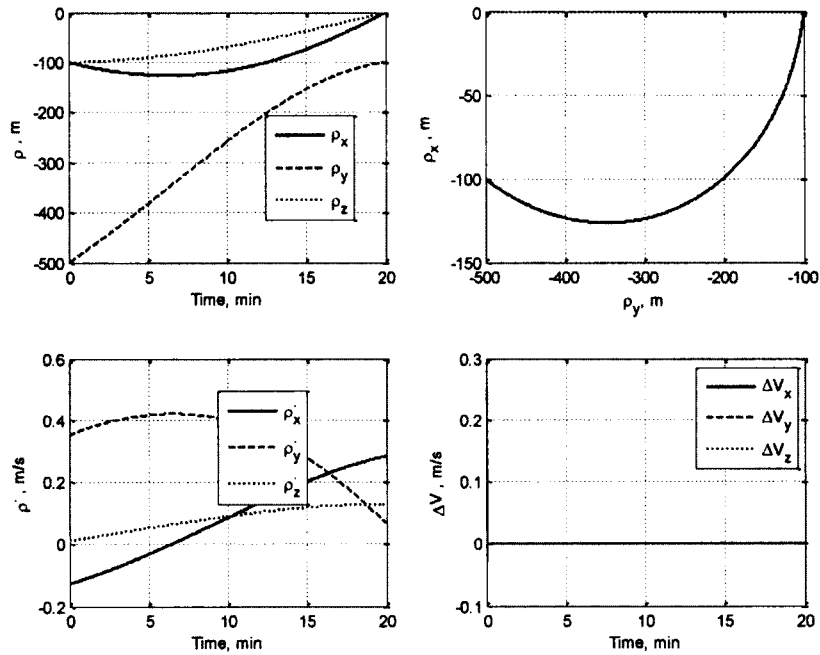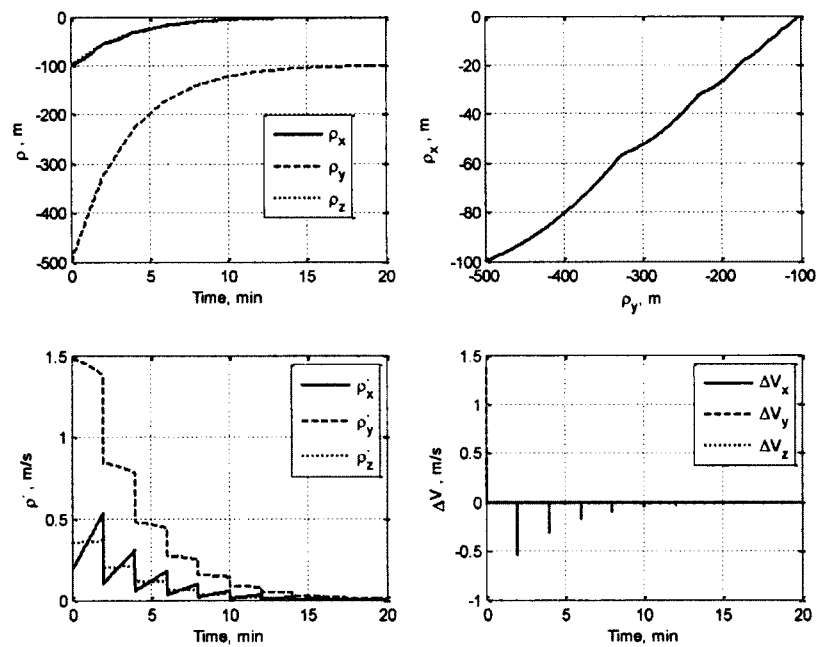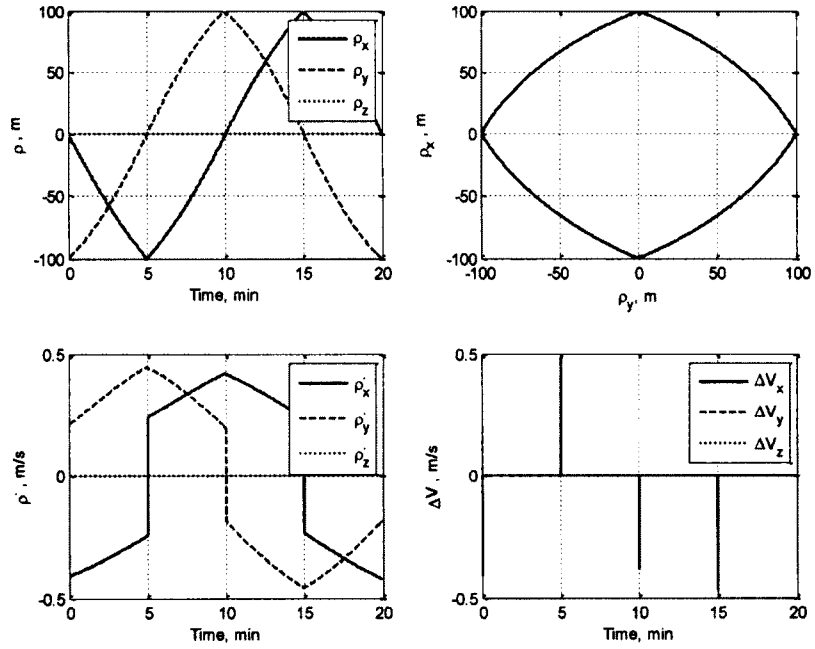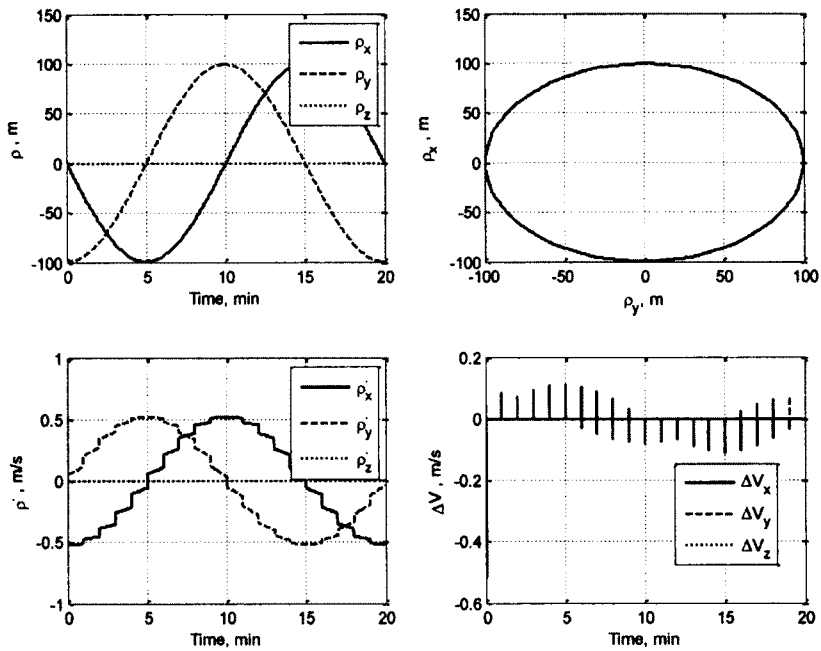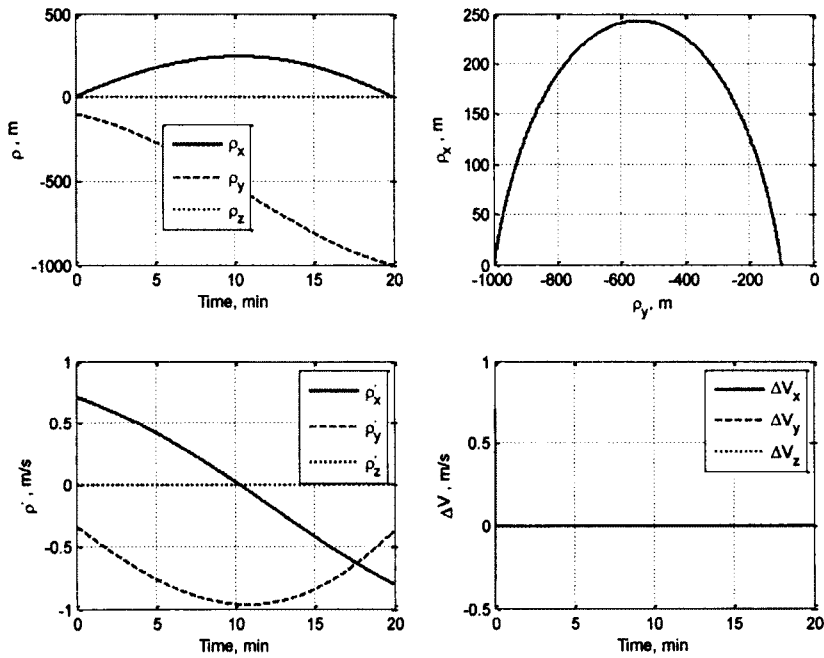
Figure 2.18 Relative Motion Analytical Single Pulse Outbound Glideslope
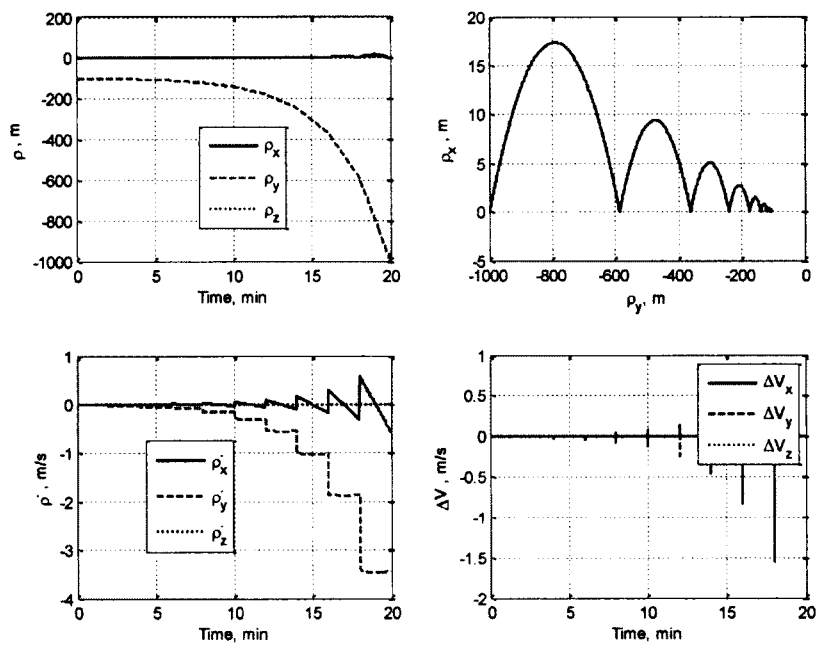
Figure 2.19 Relative Motion Analytical Multipulse Outbound Glideslope

Finally, two complete scenarios are presented in Figures 2.20- 2.23. Each scenario demonstrates the previous segments of inbound, flyaround and outbound. Each glideslope is followed by three minutes of zero rate station keeping. Figure 2.20 presents the relative motion trajectory and the required ΔV based on the TH model. In this scenario, only one pulse is used for both inbound and outbound glideslopes over a period of 20 minutes and 4 pulses for the flyaround glideslope within the same period of time. In order to estimate the accuracy of the TH model, the computed ΔVs are applied to the nonlinear chaser-target model, taking into account the two-body gravitational force only. Figure 2.21 shows the error between the analytical solution based on the TH model and the numerical solution based on the integration of the two-body problem. Figures 2.22 and 2.23 show the results of another scenario that uses 10 pulses for both inbound and outbound glideslopes and 20 pulses for flyaround glideslope. In all of these figures, different segments of the glideslope are shown and the variations of in-plane relative motion of the chaser with respect to target vehicle are presented. It is shown from these scenarios that increasing the number of pulses provides more control over the glideslope trajectory of the TH model and it also reduces the accumulated errors in relative position and relative velocity between the nonlinear model and the analytical closed form solution (see Figures 2.21 and 2.23). The next chapters will introduce how to use these guidance and analytical models with the navigation system.

2.6 Summary

Autonomous guidance algorithms are developed and illustrated based on the closed form analytical solution of the Tschauner-Hempel equations of relative motion in any Keplerian elliptic orbit. The algorithms can be used to approach, flyaround, and

depart from a target vehicle. Simulation results show how these algorithms are successful and efficient for the purpose of mission analysis and planning phases, as well as on-orbit guidance. The effects of disturbances (including orbital disturbances, navigation errors, and others uncertainties that could be found in the model) on the performance of these algorithms still needs to be analyzed. These topics and others will be addressed in the subsequent chapters.
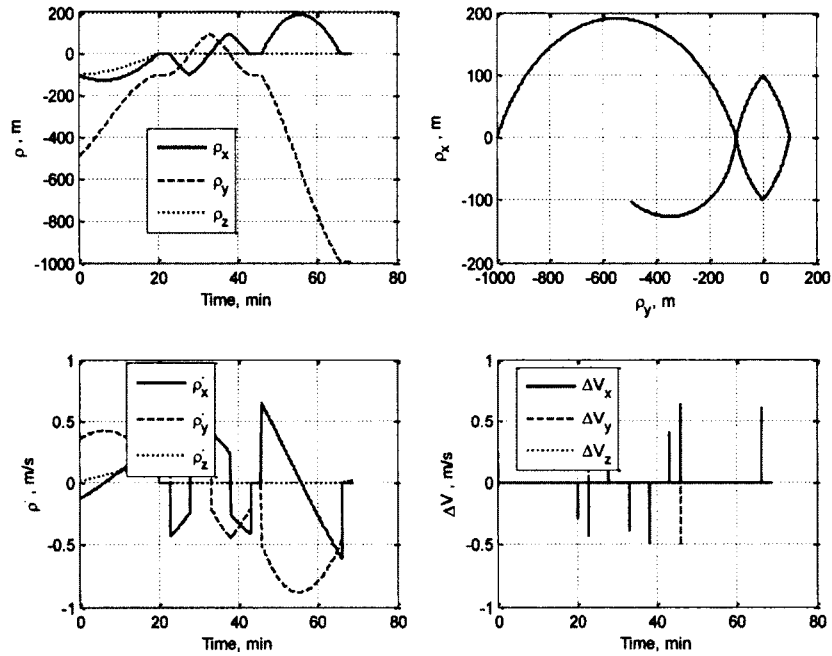
Figure 2.20 Relative Motion Analytical Multipulse (Scenario 1)
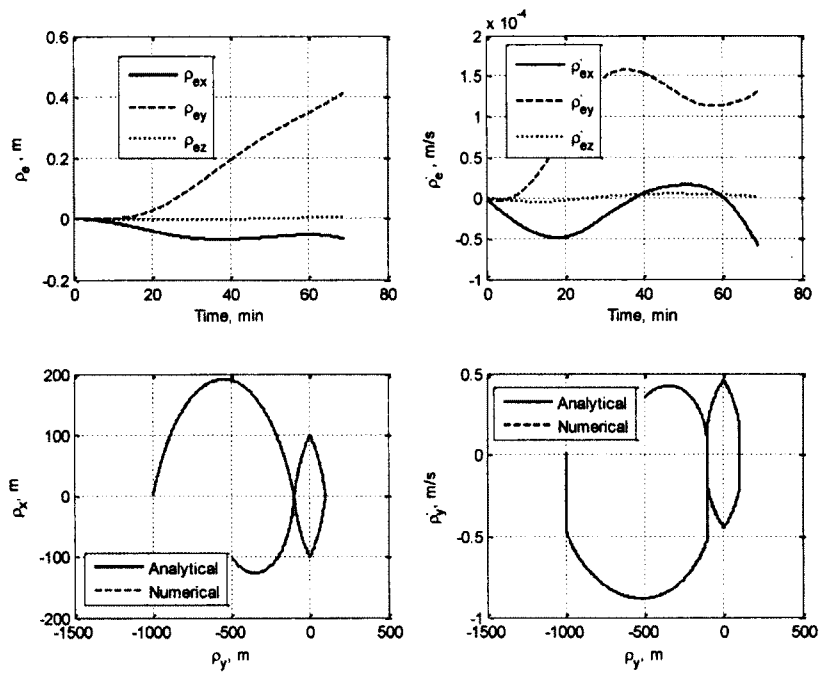
Figure 2.21 Relative Motion Analytical and Numerical Solution (Scenario 1)
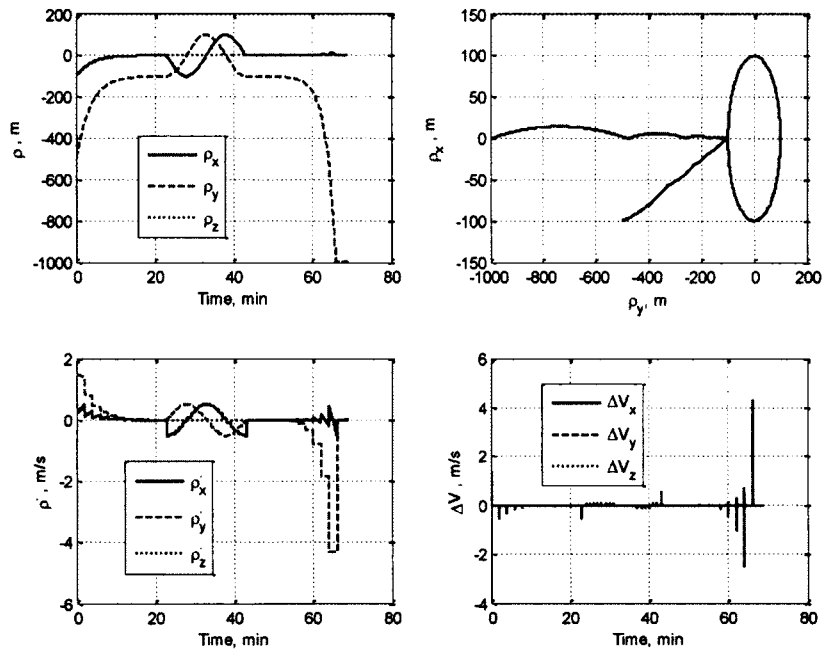
Figure 2.22 Relative Motion Analytical Multipulse (Scenario 2)
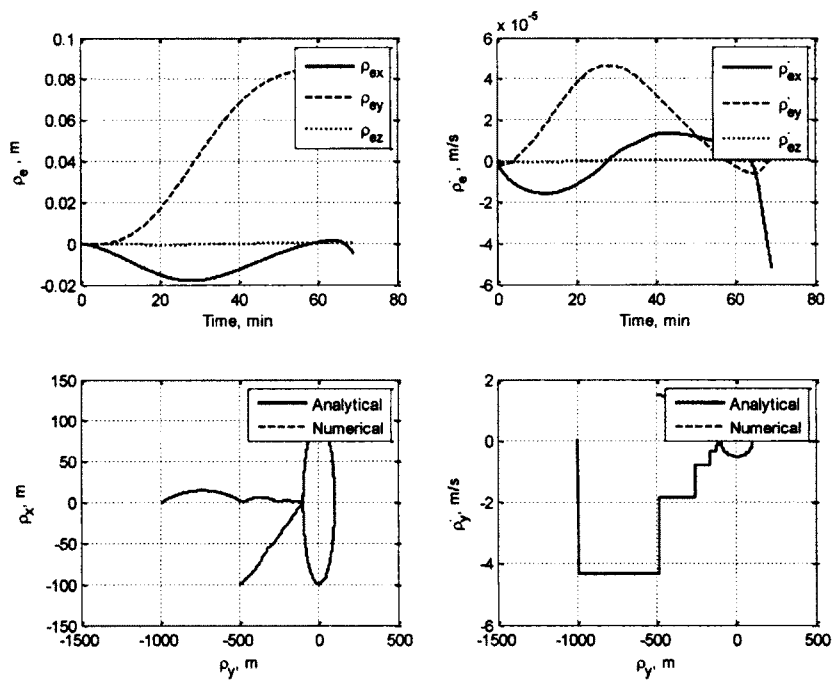
Figure 2.23 Relative Motion Analytical and Numerical Solution (Scenario 2)

3. KALMAN FILTER DESIGN

3.1 Introduction

The Kalman Filter is a computer algorithm that is used to process error corrupted measurement data.[61] More technically, the Kalman filter is a recursive, optimal, linear, least square estimator that is used in many modern applications.[62] While most real systems are in fact nonlinear, the Kalman filter can still be applied with reasonable success by linearizing the model about some expected state.[63-66]

The goal of this chapter is to introduce the standard discrete Kalman filter background information and to provide a summary of the main theory and equations behind the basic Kalman filter to serve as a reference for the work developed in this dissertation. The analysis in this chapter is summarized as follows. First, in Section 3.2 the basic notation and definitions needed to describe the Kalman filter are defined. This section includes the state dynamics, measurement equations, and state error covariance definitions. State propagation, error covariance, and state update using measurements are the subject of Section 3.3. Section 3.4 introduces another version of the Kalman filter known as the extended Kalman filter in which the linearization process is taken around a reference point different from the one used in the standard Kalman filter. The extended Kalman filter has demonstrated much better performance for a wide class of nonlinear systems. Summary tables and flow charts of the Kalman filter are presented in Section 3.5. Section 3.6 presents one of the most popular application areas of the Kalman filter. In this section, the Kalman filter concepts were applied to the space dynamical system in which the dynamic equations are continuous functions of time. Finally, the conclusion of the chapter is presented in Section 3.7.

3.2 Definition

This chapter will follow the Kalman filter derivation as presented by References 61 and 62. The Kalman filter is generally a two-step process diagramed in Figure 3.1. The filter predicts or propagates the states to some future time using a model of the system's dynamics, and also updates the state estimate and statistical properties when measurements are available. Table 3.1 summarizes the variables that will appear in the following sections.
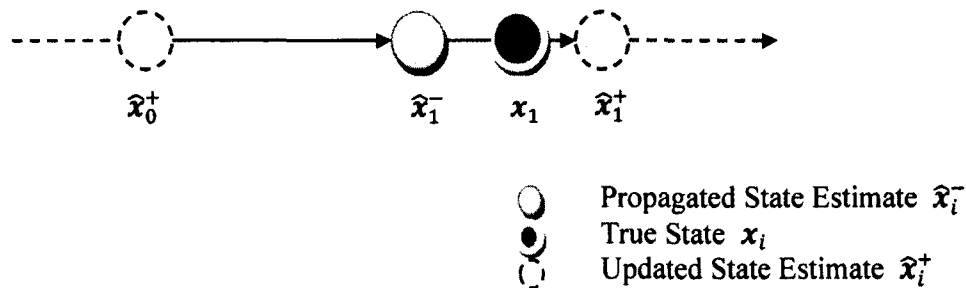
Figure 3.1 Kalman Filter Process

3.2.1 Measurements and State

The dynamics and measurement vectors can be formulated as follows for discrete time

$$x_{i+1} = g(x_i, t_i, \Delta t) + w_i \tag{3.1}$$

$$\tilde{z}_i = h(x_i, t_i) + v_i \tag{3.2}$$

where w_i is the process noise vector and v_i is the measurement noise vector. The measurement equation term $h(x_i, t_i)$ is a nonlinear function of the state variables. If the measurements are a linear combination of the elements of the state, then Equation (3.3) holds and can be substituted into Equation (3.2).

$$h(x_i, t_i) = H_i x_i \tag{3.3}$$

Table 3.1 Discrete Kalman Filter Notations

Parameter	Description
x	True state vector
$\hat{x}$	Estimated state vector
$\tilde{x}$	State vector error
x^*	Nominal state vector
δx	Perturbation of state vector
$\widehat{\delta x}$	Estimated perturbed state
$\tilde{z}$	True measurement vector
$\hat{z}$	Estimated measurement vector
ϕ	State transition matrix
w	Process noise vector
v	Measurement noise vector
H	Measurement sensitivity matrix
Q	Process noise covariance matrix
R	Measurement noise covariance matrix
P	Error covariance matrix
K	Kalman gain matrix

The process noise vector, w_i, is assumed to have zero mean and variance Q_i, and is uncorrelated with the measurement noise vector. The matrix Q_i is called the process noise covariance matrix. The statistics of the process noise include

$$E[w_i] = 0$$

$$E[w_i v_i^T] = 0 \qquad (3.4)$$

$$E[w_i w_i^T] = \begin{cases} 0 & i \neq j \\ Q_i & i = j \end{cases}$$

where E refers to the expectation of a random variable. The measurement noise vector, v_i, is assumed to have zero mean and variance R_i, where the matrix R_i is called the measurement noise covariance matrix.

$$E[v_i] = 0$$

$$E[v_i v_i^T] = \begin{cases} 0 & i \neq j \\ R_i & i = j \end{cases} \qquad (3.5)$$

If the measurement noise is known to have a nonzero mean, then the bias part of that noise should be added to the state.

The state vector x can be defined in terms of a nominal state x^* and a perturbation δx from the nominal state as

$$x = x^* + \delta x \qquad (3.6)$$

Now let $\hat{x}$ be an unbiased estimate of the state x. Then, the state estimate can also be expressed as a sum of the nominal state and an estimated perturbation $\widehat{\delta x}$

$$\hat{x} = x^* + \widehat{\delta x} \qquad (3.7)$$

These equations will be used in the linearization process required for the derivations below.

3.2.2 Error Covariance

The state error vector $\tilde{x}_i$ can be defined in terms of the state and state estimate, and equivalently, the perturbed state and its estimate

$$\tilde{x}_i = \hat{x}_i - x_i = \widehat{\delta x}_i - \delta x_i \qquad (3.8)$$

It is assumed that the measurement noise vector and process noise vector are uncorrelated with the state error $\tilde{x}_i$

$$E[\tilde{x}_i v_i^T] = 0$$

$$E[\tilde{x}_i w_i^T] = 0$$

(3.9)

The state error covariance matrix P_i can now be defined using the expectation function

$$P_i = E[\tilde{x}_i \tilde{x}_i^T]$$

(3.10)

In Equation (3.1), the state dynamics have been presented as a general function of state and time. No restrictions are thus placed on whether $g(x_i, t_i, \Delta t)$ is a linear or nonlinear function. In fact, formulating an estimator based on nonlinear dynamics is very difficult, and the most common approach is to linearize the dynamics. Specifically, there are two trajectories that are used frequently in this linearization: a nominal trajectory, and the filter's best estimate of the actual trajectory. These approaches will be explored in detail in the subsequent sections.

3.3 State and Covariance Propagation

This section describes the methods and equations that can be used to propagate the state and covariance matrix ahead one time step in a discrete Kalman filter.

3.3.1 State

The discrete true state is propagated ahead one time step using Equation (3.1). If the state dynamics are linear, then Equation (3.11) describes the transition from x_i to x_{i+1}, where $\phi_{i+1,i}$ is called the state transition matrix from t_i to t_{i+1}.

$$g(x_i, t_i, \Delta t) = \phi_{i+1,i} x_i$$

(3.11)

For most real systems, the state dynamics are not linear and a numerical integrator must be used to propagate the state. In this case, $g(x_i, t_i, \Delta t)$ is truly an algorithm and not

simply an equation. Process noise is added to the state propagation because it is very unlikely that the mathematical model of the system is a perfectly accurate representation.

The state estimate is propagated in a similar fashion, where now the algorithm $g(\hat{x}_i, t_i, \Delta t)$ operates on the state estimate instead of the true state, and the noise term w is not included since $\hat{w} = 0$.

$$\hat{x}_{i+1} = g(\hat{x}_i, t_i, \Delta t) \tag{3.12}$$

3.3.2 Error Covariance

The error covariance matrix must also be propagated forward in time between measurements. By substituting Equation (3.6) into Equations (3.1) and (3.12), the true and estimated state updates can be found in terms of the nominal state and the perturbed state vector

$$x_{i+1} = g(x_i^* + \delta x_i, t_i, \Delta t) + w_i \tag{3.13}$$

$$\hat{x}_{i+1} = g(x_i^* + \hat{\delta x}_i, t_i, \Delta t) \tag{3.14}$$

Taylor series expansions can be used to expand these equations around the nominal states assuming the perturbation is small

$$x_{i+1} = g(x_i^*, t_i, \Delta t) + \frac{\partial g}{\partial x_i}\Big|_{x_i^*} \delta x_i + O(\delta x_i^2) + w_i \tag{3.15}$$

$$\hat{x}_{i+1} = g(x_i^*, t_i, \Delta t) + \frac{\partial g}{\partial \hat{x}_i}\Big|_{x_i^*} \hat{\delta x}_i + O(\hat{\delta x}_i^2) \tag{3.16}$$

The propagation of the state error is obtained by subtracting Equation (3.15) from Equation (3.16) and utilizing Equation (3.8) (neglecting higher order terms).

$$\hat{x}_{i+1} - x_{i+1} = \phi_{i+1,i}(\hat{\delta x}_i - \delta x_i) - w_i$$

$$\tilde{x}_{i+1} = \phi_{i+1,i}\tilde{x}_i - w_i \tag{3.17}$$

When the state perturbation is small, the state transition matrix, $\phi_{i+1,i}$, defined in Equation (3.11) has the following general form for linear or nonlinear dynamics.

$$\phi_{i+1,i} = \frac{\partial g}{\partial x_i}\bigg|_{x_i^*} = \frac{\partial g}{\partial \hat{x}_i}\bigg|_{x_i^*} = \frac{\partial x_{i+1}}{\partial x_i}\bigg|_{x_i^*} \tag{3.18}$$

By using the definition of the error covariance matrix from Equation (3.10), an equation for the propagated covariance matrix can be formed.

$$P_{i+1} = E[\tilde{x}_{i+1}\tilde{x}_{i+1}^T] = E\left[\left(\phi_{i+1,i}\tilde{x}_i - w_i\right)\left(\phi_{i+1,i}\tilde{x}_i - w_i\right)^T\right]$$

$$= E\left[\phi_{i+1,i}\tilde{x}_i\tilde{x}_i^T\phi_{i+1,i}^T - w_i\tilde{x}_i^T\phi_{i+1,i}^T - \phi_{i+1,i}\tilde{x}_iw_i^T + w_iw_i^T\right] \tag{3.19}$$

Since the state error and process noise are uncorrelated as shown above in Equation (3.9), the middle terms drop out, leaving the following simplified form of the error covariance matrix propagation equation.

$$P_{i+1} = \phi_{i+1,i} P_i\phi_{i+1,i}^T + Q_i \tag{3.20}$$

3.3.3 Measurement Update

The only external information that is available to make a state update are the measurements. Thus, it seems reasonable to try to improve the state estimate by using feedback from the measurement data, thus the measurement update equation will be formulated as follows

$$\hat{x}_i^+ = \hat{x}_i^- + K_i(\tilde{z}_i - \hat{z}_i) \tag{3.21}$$

Equation (3.21) states that the new estimate of the state will be the old estimate of the state, plus a correction directly related to the difference between the actual measurement data and what the filter expected that data to be. The matrix K_i is a weighting matrix that specifies how much weight will be given to each measurement, with respect to each state. This gain matrix will be found to optimize the state update.

The estimated measurement can be found by operating the measurement equation on the state estimate as

$$\hat{z}_i = h(\hat{x}_i, t_i) \tag{3.22}$$

By using Taylor expansions, and with the help of Equations (3.3), (3.6), (3.7), and (3.22), the true and estimated measurement equations can be expanded around the nominal states, assuming the perturbation is small.

$$\tilde{z}_i = h(x_i^*, t_i) + \frac{\partial h}{\partial x_i}\bigg|_{x_i^*} \delta x_i + O(\delta x_i^2) + v_i \tag{3.23}$$

$$\hat{z}_i = h(x_i^*, t_i) + \frac{\partial h}{\partial \hat{x}_i}\bigg|_{x_i^*} \widehat{\delta x}_i + O(\widehat{\delta x}_i^2) \tag{3.24}$$

The measurement error is obtained by subtracting Equation (3.24) from Equation (3.23) and neglecting higher order terms

$$\tilde{z}_i - \hat{z}_i = -H_i \tilde{x}_i + v_i \tag{3.25}$$

where H_i is called the measurement sensitivity matrix, defined by

$$H_i = \frac{\partial h}{\partial x_i}\bigg|_{x_i^*} \tag{3.26}$$

Back substituting from Equation (3.25) into Equation (3.21) and rearranging leads to the following updated equation for the state error

$$\tilde{x}_i^+ = (I - K_i H_i)\tilde{x}_i^- + K_i v_i \tag{3.27}$$

Now, the covariance update can be found by defining of Equation (3.10) (utilizing Equation (3.9)) to be

$$P_i^+ = E\left[\tilde{x}_i^+ \tilde{x}_i^{+T}\right]$$

$$= E\left[\left((I - K_i H_i)\tilde{x}_i^- + K_i v_i\right)\left((I - K_i H_i)\tilde{x}_i^- + K_i v_i\right)^T\right] \tag{3.28}$$

$$= (I - K_i H_i) P_i^- (I - K_i H_i)^\mathsf{T} + K_i R_i K_i^\mathsf{T}$$

In Equation (3.28), the measurement gain matrix K_i is arbitrary. The optimal gain matrix can be found by choosing it such that the update state estimate will be a minimum variance estimate of the state. In order to do that, it is required to minimize the following cost quadratic form

$$
\begin{aligned}
J &= a^T P_i^+ a \\
&= a^T [(I - K_i H_i) P_i^- (I - K_i H_i)^T + K_i R_i K_i^T] a
\end{aligned}
\tag{3.29}
$$

where a is any arbitrary nonzero vector. To determine the optimal gain, the partial of J with respect to K_i must be set equal to zero, noting that special attention needs to be made when taking a partial with respect to a vector.

$$
0 = \frac{\partial J}{\partial K_i} = \left[\frac{\partial J}{\partial a^T K_i}\right] \left[\frac{\partial a^T K_i}{\partial K_i}\right] = \left[\frac{\partial J}{\partial a^T K_i}\right] a^T
\tag{3.30}
$$

Substituting Equation (3.29) into Equation (3.30) and reducing it, the following formula must equal zero for any vector a.

$$
0 = 2a^T[-(I - K_i H_i) P_i^- H_i^T + K_i R_i] a^T
\tag{3.31}
$$

By setting the interior terms of Equation (3.29) to zero and rearranging, the inner term, is finally revealed the optimal gain K_i that minimizes the updated state covariance.

$$
K_i = P_i^- H_i^T (H_i P_i^- H_i^T + R_i)^{-1}
\tag{3.32}
$$

Interestingly, the optimal gain form Equation (3.32) can be substituted into Equation (3.28) to yield a more streamlined form of the covariance update equation.

$$
P_i^+ = (I - K_i H_i) P_i^-
\tag{3.33}
$$

Now, a full state update (Equation (3.21)) can be performed with measurement data utilizing Equations (3.32) and (3.33).

3.4 Extended Kalman Filter

The extended Kalman filter is the upgraded version of a standard Kalman filter with only a few modifications. In this filter, the linearization process is around the state estimate rather than a nominal trajectory state, and the propagation and updating equations are found to be the same.

The first order Taylor series expansion around the estimated state using Equations (3.1), (3.8), and (3.12) results in

$$x_{i+1} = g(\hat{x}_i - \tilde{x}_i, t_i, \Delta t) + w_i$$

$$= g(\hat{x}_i, t_i, \Delta t) - \frac{\partial g}{\partial x_i}\bigg|_{\hat{x}_i} \tilde{x}_i + O(\tilde{x}_i^2) + w_i \qquad (3.34)$$

$$= \hat{x}_{i+1} - \frac{\partial g}{\partial x_i}\bigg|_{\hat{x}_i} \tilde{x}_i + O(\tilde{x}_i^2) + w_i$$

By arranging Equation (3.34) and neglecting the higher order terms, the following equation is obtained for the propagation of the state error

$$\tilde{x}_{i+1} = \phi_{i+1,i}\tilde{x}_i - w_i \qquad (3.35)$$

Here $\phi_{i+1,i}$ is the new state transition matrix as defined in Equation (3.36) for the extended filter

$$\phi_{i+1,i} = \frac{\partial g}{\partial x_i}\bigg|_{\hat{x}_i} = \frac{\partial x_{i+1}}{\partial x_i}\bigg|_{\hat{x}_i} \qquad (3.36)$$

A similar technique to that above can be applied to derive the measurement sensitivity matrix for the extended Kalman filter. The formulation of the sensitivity matrix is found to be identical with x_i^* replaced by $\hat{x}_i$ in Equation (3.26)

$$H_i = \frac{\partial h}{\partial x_i}\bigg|_{\hat{x}_i} \qquad (3.37)$$

Again, the error covariance matrix propagation and optimal gain matrix can be completed as before with the same results.

3.5 Filter Summary

This section has summarized the key equations used in the discrete Kalman filter loop. Table 3.2 lists the main equations involved in propagating the state estimate and covariance matrix between measurement times. Table 3.3 lists the main equations involved in updating the state estimate and covariance matrix with measurement.

Table 3.2 Discrete Kalman Propagation Equations

$$\hat{x}_i = g(\hat{x}_{i-1}, t_{i-1}, \Delta t)$$

$$g(x_{i-1}, t_{i-1}, \Delta t) = \phi_{i,i-1} x_{i-1}$$

$$P_i = \phi_{i,i-1} P_{i-1} \phi_{i,i-1}^T + Q_{i-1}$$

$$\phi_{i,i-1} = \left.\frac{\partial g}{\partial x_{i-1}}\right|_{x_{i-1}^*} = \left.\frac{\partial x_i}{\partial x_{i-1}}\right|_{x_{i-1}^*}$$

Table 3.3 Discrete Kalman Measurement Update Equations

$$\hat{x}_i^+ = \hat{x}_i^- + K_i(\hat{z}_i - \hat{z}_i)$$

$$\hat{z}_i = h(\hat{x}_i, t_i)$$

$$h(x_i, t_i) = H_i x_i \Rightarrow H_i = \left.\frac{\partial h}{\partial x_i}\right|_{x_i^*}$$

$$K_i = P_i^- H_i^T (H_i P_i^- H_i^T + R_i)^{-1}$$

$$P_i^+ = (I - K_i H_i) P_i^-$$

For the extended Kalman filter case, the state transition matrix, $\phi_{i,i-1}$, and the measurement sensitivity matrix, H_i, are evaluated around the estimated state instead of the nominal trajectory state. In summary, the basic flow of the navigation filter implementation is represented in the flow chart shown in Figure 3.2.

Initial $\hat{x}_{i-1}, P_{i-1}$

Propagate

$$\hat{x}_i = g(\hat{x}_{i-1}, t_{i-1}, \Delta t)$$

$$P_i = \phi_{i,i-1}\, P_{i-1} \phi_{i,i-1}^T + Q_{i-1}$$

Sensor Measurements

No

Yes

Update

$$K_i = P_i^- H_i^T \left(H_i P_i^- H_i^T + R_i\right)^{-1}$$

$$\hat{z}_i = h(\hat{x}_i, t_i)$$

$$\hat{x}_i^+ = \hat{x}_i^- + K_i(z_i - \hat{z}_i)$$

$$P_i^+ = (I - K_i H_i) P_i^-$$
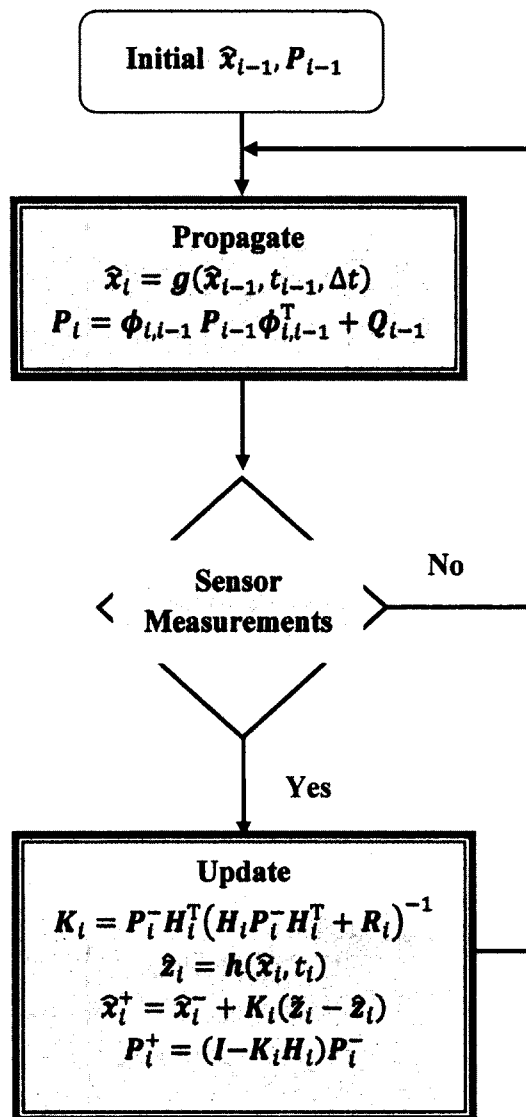
Figure 3.2 Filter Equations Flow Chart

3.6 Space Application

One of the primary applications of a Kalman filter is in the space navigation area.[61,62,67] The main objective of the filter is to estimate the spacecraft's position, velocity, and orientation given noisy sensor measurements, imperfect dynamic models, and uncertain initial conditions. The logic behind the navigation filter is to process information collected from sensors and various mathematical models to generate the best possible estimation of the states. The space navigation application of the Kalman filter is presented in this section.

3.6.1 Dynamic Models

The previous definitions and methodology of the Kalman filter technique are now applied to the following closed loop dynamic system, as illustrated in Figure 3.3. In this figure, the plant model is represented by the following differential equation

$$\dot{x} = g(x, \hat{u}, y, t) + w \tag{3.38}$$

where x is a vector of n_x true states, $\hat{u}$ is a vector of $n_{\hat{u}}$ actuator commands issued by the control system, y is a vector of n_y noiseless sensor continuous measurements, and w is a zero mean white noise vector process with covariance

$$E[w(t)w^T(t')] = S_w \delta(t - t') \tag{3.39}$$

The covariance matrix S_w represents the strength of the process noise and essentially defines the quality of the plant model itself. The continuous measurements $\tilde{y}$ are used to reduce the complexity of the state dynamic models and is given by

$$\tilde{y} = y + \eta \tag{3.40}$$

where η represents continuous measurement noise and is a zero mean white noise vector process with covariance
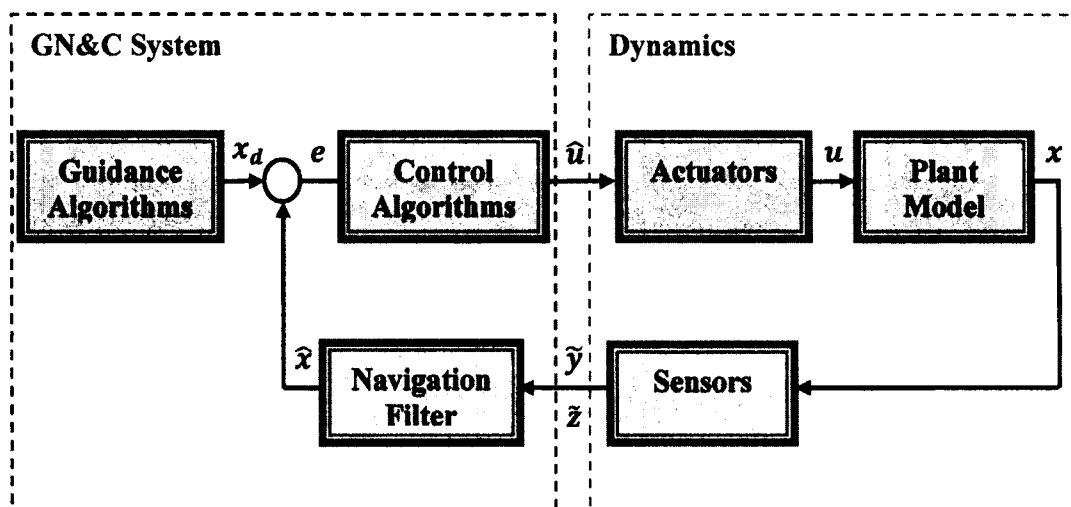
Figure 3.3 Closed Loop GN&C System

$$E[\eta(t)\eta^T(t')] = S_\eta \delta(t - t') \qquad (3.41)$$

The navigation filter is used to estimate the states of the plant model. Typically, only the key states are estimated such that the $n_{\hat{x}}$ dimensional navigation state $\hat{x}$ is derived from a subset of the true state vector ($n_{\hat{x}} < n_x$). The filter can only be used to propagate an estimated value of each state. In many applications, this is done in an extended Kalman filter where the differential equations of motion of the navigation state are integrated forward in time.

$$\dot{\hat{x}} = g(\hat{x}, \hat{u}, \tilde{y}, t) \qquad (3.42)$$

Equation (3.42) uses the actual measurements, $\tilde{y}$, which ultimately influence the accuracy of the state prediction.

3.6.2 Propagation and Correction

Applying the Kalman filter steps and procedures in the dynamic system described by Equation (3.38) leads to the following equation for state error propagation, keeping only the first-order terms of the Taylor series

$$\dot{\widetilde{x}} = G_{\hat{x}}\widetilde{x} + G_{\bar{y}}\eta - w$$

$$G_{\hat{x}} = \frac{\partial g}{\partial x}\bigg|_{\hat{x},\bar{y}}, \quad G_{\bar{y}} = -\frac{\partial g}{\partial y}\bigg|_{\hat{x},\bar{y}} \tag{3.43}$$

where $G_{\hat{x}}$ and $G_{\bar{y}}$ are partials of the state dynamics with respect to the states and continuous measurements respectively.

The solution to this well-known linear differential equation involves the exponential matrix, which is the state transition matrix $\phi(t, t_0)$.

$$\widetilde{x}(t) = \phi(t, t_0)\widetilde{x}(t_0) + \int_{t_0}^{t} \phi(t, \tau)\, G_{\bar{y}}\eta(\tau)d\tau - \int_{t_0}^{t} \phi(t, \tau)\, w(\tau)d\tau$$

$$\phi(t, t_0) = e^{G_{\hat{x}}(t-t_0)} \tag{3.44}$$

Also, the state covariance matrix can be expressed as

$$P(t) = \phi(t, t_0)P(t_0)\phi^{T}(t, t_0) + Q_\eta + Q_w$$

$$Q_\eta = \int_{t_0}^{t} \phi(t, \tau)\, G_{\bar{y}}S_\eta G_{\bar{y}}^{T}\phi^{T}(t, \tau)d\tau \tag{3.45}$$

$$Q_w = -\int_{t_0}^{t} \phi(t, \tau)\, S_w\phi^{T}(t, \tau)d\tau$$

This equation is known as a discrete Ricatti equation. Q_η is referred to as the continuous measurement error covariance matrix and it characterizes the added uncertainty of the propagated states due to errors with the sensor measurements. Q_w is known as the state process noise covariance matrix and it characterizes the added uncertainty due to the limitations in the system dynamic models.

When impulsive maneuvers, such as thrusters, are executed to reposition the spacecraft or change its orientation, it is convenient to express these changes as instantaneous corrections to the state vector.

$$x^+ = x^- + \Delta x + \Delta w \qquad (3.46)$$

where Δx is an instantaneous correction of the state issued by the actuator. A random execution error Δw with covariance $S_{\Delta w}$ is also experienced during the correction. This additional error source accounts for uncertainties associated with the actuator performance. The correction algorithm in the navigation filter computes the correction based on the latest update estimate while assuming the random execution errors are nominally zero.

$$\hat{x}^+ = \hat{x}^- + \Delta \hat{x} \qquad (3.47)$$

Due to this correction of the state vector, the final state covariance correction equation becomes[67]

$$P^+ = [I + D_{\hat{x}}]P^+[I + D_{\hat{x}}]^T + S_{\Delta w}$$

$$D_{\hat{x}} = \left.\frac{\partial \Delta x}{\partial x}\right|_{\hat{x}^-}, \quad S_{\Delta w} = E[\Delta w \Delta w^T] \qquad (3.48)$$

where $D_{\hat{x}}$ is the partial derivative of the correction function with respect to the state. The correction of the state vector and update of the covariance equation due to measurement updates is still exactly the same as in Equations (3.21) and (3.33) respectively.

The following algorithm that is shown in Table 3.4 summarizes the equations for the Kalman filter for the space navigation system described by Equation (3.42). Having defined the initial conditions, the states and covariance matrix are propagated forward in time to provide the most current estimate of the states. If an impulsive maneuver is executed, both the state and covariance matrix are corrected to account for this instantaneous change. When measurements are available, the predicted state values are updated and the filter outputs these new estimates as updated state values for that time period. The cycle continues as the time elapses. This flow of propagation, correction, and

updating the states and covariance matrix repeats until the estimation process is completed.

Table 3.4 Navigation Filter Summary

$$\dot{\hat{x}} = g(\hat{x}, \hat{u}, \hat{y}, t)$$

$$P(t) = \phi(t, t_0)P(t_0)\phi^{\mathrm{T}}(t, t_0) + Q_\eta + Q_w$$

$$\hat{x}^+ = \hat{x}^- + \Delta\hat{x}$$

$$P^+ = [I + D_{\hat{x}}]P^+[I + D_{\hat{x}}]^{\mathrm{T}} + S_{\Delta w}$$

$$\hat{x}_i^+ = \hat{x}_i^- + K_i(\tilde{z}_i - \hat{z}_i)$$

$$K_i = P_i^- H_i^{\mathrm{T}}\left(H_i P_i^- H_i^{\mathrm{T}} + R_i\right)^{-1}$$

$$P_i^+ = (I - K_i H_i)P_i^-$$

3.7 Summary

The Kalman filter algorithms are reviewed in this chapter. The summary filter flow chart, state propagation equations and measurement update equations are presented. Application of the filter for the space navigation system is developed for the case in which the state dynamic equations are a continuous function of time. The analysis of this chapter will be the basis for the next chapters.

4. ORBITAL SPACE RENDEZVOUS

4.1 Introduction

The interest in autonomous rendezvous and proximity operations has increased with the recent demonstration of XSS-11, Demonstration of Autonomous Rendezvous Technology (DART), and Orbital Express. Autonomous rendezvous and proximity operations have also been demonstrated by the Japanese EST-VII, and the Russian Progress vehicles. In addition, future missions to the ISS will require autonomous rendezvous and proximity operations.[2]

Some of the critical aspects of this problem are the development of autonomous navigation and guidance systems. First, the navigation system should have the capability to autonomously estimate the relative position and velocity between both vehicles. Although this problem has been addressed elsewhere,[58,68-70] this chapter approaches the problem from a different perspective. The navigation filter is based on the relative system, instead of an inertial system, and the analytical closed form solution of the TH equations. Further, the linearized high fidelity model developed in previous chapters, is used by the navigation filter. Second, algorithms for autonomous guidance of the spacecraft, described before in Chapter 2 to approach, to flyaround, and to depart from a target vehicle in a general orbit are implemented.

This chapter uses an extended Kalman filter formulation, described previously in Chapter 3, to estimate the relative motion position and velocity by using range and angle measurements from a LIDAR system. Thrusters are used for the purpose of translational control by expelling propellant. Both techniques of discrete and continuous thrust are investigated in this chapter. The filter basically consists of two main stages. The first

stage is the propagation stage where the states are propagated numerically. The second stage comes when the measurements from the LIDAR system are available and it is used to update the states from the first stage. The corresponding measurement models, process noise matrix, and other filter parameters are provided. The effects of the navigation filter and control algorithms are included in the analysis.

The objective of this chapter is as follows: (1) highlight the potential of analytical closed form solutions of the TH equations and the linearized high fidelity model in the context of autonomous orbital rendezvous and close proximity operations, (2) develop a navigation filter that can determine the relative position and velocity between target and chaser vehicles and support closed loop proximity operations and maneuvers, and (3) design autonomous guidance algorithms and a control system for chaser vehicle to approach, to flyaround, and to depart from a target vehicle in proximity operations in a general perturbed orbit.

The analysis in the current chapter is summarized as follows. First, Section 4.2 presents the true and navigation dynamic models of relative motion for the chaser with respect to the target on a general perturbed orbit. In Section 4.3, the relative navigation is presented based on the TH model closed form solution and the linear high fidelity model using range and angle measurements of the target and an extended Kalman filter. Section 4.4 presents open loop and closed loop controller design techniques. The open loop controller design techniques are based on single pulse or multipulse discrete thrust developed previously in Chapter 2 to move the chaser vehicle in the vicinity of the target vehicle, while the closed loop controller design techniques are based on continuous thrust feedback in a closed loop proportional-derivative (PD) controller. In Section 4.4, the

relative navigation, guidance, and control algorithm performance is illustrated through different numerical examples and comparisons are made with the true nonlinear model. Finally, in Section 4.5, conclusion of the work is presented and suggestions are made for future work.

4.2 True and Navigation Models

4.2.1 True Model

The true model states vector for the orbital rendezvous simulation is a 12-dimensional vector defined by 6 target orbital element states and 6 relative states. The 6 target states include the semi-major axis a, eccentricity e, inclination i, right ascension of the ascending node Ω, argument of periapsis ω, and true anomaly f. The 6 relative states include the relative position vector ρ, and the relative velocity vector $\dot{\rho}$ of the chaser, with respect to the target in the LVLH frame of the target vehicle. The dynamics for the true state vector which includes the target states and relative states are grouped together and modeled mathematically as

True Target
States:

$$\frac{da}{dt} = \frac{2a^2}{H}\left[es_f a_x + \frac{p}{R}a_y\right]$$

$$\frac{de}{dt} = \frac{1}{H}\{ps_f a_x + [(p+R)c_f + Re]a_y\}$$

$$\frac{di}{dt} = \frac{Rc_{\omega+f}}{H}a_z$$

$$\frac{d\Omega}{dt} = \frac{Rs_{\omega+f}}{Hs_i}a_z$$

$$\frac{d\omega}{dt} = \frac{1}{He}\{-pc_f a_x + (p+R)s_f a_y\} - \frac{Rs_{\omega+f}c_i}{Hs_i}a_z$$

$$\frac{df}{dt} = \frac{H}{R^2} + \frac{1}{He}[pc_f a_x - (p+R)s_f a_y]$$

$$(4.1)$$

where

$$[a]^{LVLH} = \left[a_{J_2} + \mathbf{f_a} + \mathbf{f_w}\right]^{LVLH}$$

and

True Relative Model :

$$\ddot{p} = [\mathbf{f_c}]^{LVLH} - [\mathbf{f_t}]^{LVLH} - 2\omega \times \dot{p} - \omega \times \omega \times p - \dot{\omega} \times p \quad (4.2)$$

The definitions of all terms of the true model were defined and explained in Chapter 2.

4.2.2 Navigation Model

Similar to the true model, the states for the navigation filter are represented by six state variables containing the relative position and relative velocity of the chaser vehicle with respect to the target vehicle. The target vehicle dynamic model used to propagate the navigation model are

$$\frac{d\hat{a}}{dt} = \frac{2\hat{a}^2}{\hat{H}}\left[\hat{e}s_f\hat{a}_x + \frac{\hat{p}}{\hat{R}}\hat{a}_y\right]$$

$$\frac{d\hat{e}}{dt} = \frac{1}{\hat{H}}\{\hat{p}s_f\hat{a}_x + [(\hat{p} + \hat{R})c_f + \hat{R}\hat{e}]\hat{a}_y\}$$

$$\frac{d\hat{\imath}}{dt} = \frac{\hat{R}c_{\hat{\omega}+f}}{\hat{H}}\hat{a}_z$$

Navigation Target States:

$$\frac{d\hat{\Omega}}{dt} = \frac{\hat{R}s_{\hat{\omega}+f}}{\hat{H}s_i}\hat{a}_z \quad (4.3)$$

$$\frac{d\hat{\omega}}{dt} = \frac{1}{\hat{H}\hat{e}}\{-\hat{p}c_f\hat{a}_x + (\hat{p} + \hat{R})s_f\hat{a}_y\} - \frac{\hat{R}s_{\hat{\omega}+f}c_i}{\hat{H}s_i}\hat{a}_z$$

$$\frac{d\hat{f}}{dt} = \frac{\hat{H}}{\hat{R}^2} + \frac{1}{\hat{H}\hat{e}}[\hat{p}c_f\hat{a}_x - (\hat{p} + \hat{R})s_f\hat{a}_y]$$

where

$$[\hat{a}]^{LVLH} = \left[\hat{a}_{J_2} + \hat{\mathbf{f}}_a\right]^{LVLH}$$

The orbit-perturbed acceleration term $\hat{a}$ is different from the term used in the true model in that it does not contain the unmodeled disturbance acceleration term $\mathbf{f_w}$. This navigation target model is used only to assist in the process of estimation. The dynamic relative navigation model states are

Navigation
Relative Model :
$$\begin{bmatrix} \hat{\rho}(t) \\ \hat{\dot{\rho}}(t) \end{bmatrix} = \phi(t, t_0) \begin{bmatrix} \hat{\rho}(t_0) \\ \hat{\dot{\rho}}(t_0) \end{bmatrix} \qquad (4.4)$$

where ϕ is the state transition matrix defined in Equation (2.8) for the linear time varying model and by Equation (2.21) for the Tschauner-Hempel model.[57]

4.3 Relative Navigation Filter

This section is concerned with the estimation of the position and velocity of the chaser relative to the target. The estimation is accomplished by using the range and angle measurements of the target from a LIDAR system in the LVLH frame of the chaser. The relative system uses an extended Kalman filter for estimation purposes and a discrete or continuous thrust controller based design methodology for maneuver targeting. Orbital elements of the target are maintained by numerically propagating the Gauss variational equations with J_2 and drag perturbations with respect to time. These orbital elements are used to compute the transformation matrix of the target vehicle with respect to the inertial frame and to assist in estimating LIDAR measurements.

4.3.1 Filter Parameters

An extended Kalman filter is derived from the nonlinear models (see Chapter 3) as illustrated in the equations below.[66]

$$\dot{x} = f(x, u, t) + w(t), \qquad w(t) \sim N(0, Q) \qquad (4.5)$$

$$\tilde{z}_k = h(x_k, t) + v_k, \qquad v_k \sim N(0, R_k) \qquad (4.6)$$

Here, the state vector x can represent relative position and velocity of the chaser as well as other parameters that need to be estimated for use by other flight algorithms. The time derivatives of the states $\dot{x}$ are a function of the states, inputs, time, and additive process noise w. This process noise is used to approximate unmodeled disturbances and other random disturbances to the dynamics. The measurements $\tilde{z}_k$ are modeled as functions of the states, time, and measurement noise v_k. The process noise and measurement noise are normally distributed with zero mean and covariance Q and R_k respectively.

The following steps summarize the Kalman filter equations that are used to estimate the relative motion states and are based on minimizing the mean square of the error.

1. Enter prior state estimate $\hat{x}_k^-$ and its error covariance P_k^- and compute the Kalman gain

$$K_k = P_k^- H_k^T (H_k P_k^- H_k^T + R_k)^{-1} \tag{4.7}$$

2. Update state estimate by measurement $\tilde{z}_k$

$$\hat{z}_k^- = h(\hat{x}_k^-) \tag{4.8}$$

$$\hat{x}_k = \hat{x}_k^- + K_k(\tilde{z}_k - \hat{z}_k^-) \tag{4.9}$$

3. Compute error covariance for updated state estimate

$$P_k = (I - K_k H_k)P_k^- \tag{4.10}$$

4. Project ahead

$$\hat{x}_{k+1}^- = \phi_k \hat{x}_k \tag{4.11}$$

$$P_{k+1}^- = \phi_k P_k \phi_k^T + Q_k \tag{4.12}$$

where I denotes the 6×6 identity matrix, ϕ_k is the state transition matrix, and H_k is the measurements partial matrix that represents the sensitivity of the measurements to changes in the states.

By following the line steps of References 35, 68, 71, and 72, the initial error

covariance matrix P_0^-, which represents how accurately the initial relative position and

velocity values of the target are known, is given by

$$P_0^- = \begin{bmatrix} \sigma_x^2 & 0 & 0 & 0 & \varepsilon\sigma_x\sigma_{\dot{y}} & 0 \\ 0 & \sigma_y^2 & 0 & \varepsilon\sigma_{\dot{x}}\sigma_y & 0 & 0 \\ 0 & 0 & \sigma_z^2 & 0 & 0 & 0 \\ 0 & \varepsilon\sigma_{\dot{x}}\sigma_y & 0 & \sigma_{\dot{x}}^2 & 0 & 0 \\ \varepsilon\sigma_x\sigma_{\dot{y}} & 0 & 0 & 0 & \sigma_{\dot{y}}^2 & 0 \\ 0 & 0 & 0 & 0 & 0 & \sigma_{\dot{z}}^2 \end{bmatrix} \qquad (4.13)$$

where σ_x, σ_y, and σ_z denote the standard deviation uncertainties of the relative position

components and $\sigma_{\dot{x}}$, $\sigma_{\dot{y}}$, and $\sigma_{\dot{z}}$ are the standard deviation uncertainties for the relative

velocity components. The coefficient ε refers to the uncertainty correlation coupling

between relative position and velocity components in the LVLH coordinate frame and it

ranges between plus and minus unity. The discrete process noise matrix Q_k of relative

motion can be approximated by

$$Q_k = \begin{bmatrix} \sigma_{w_x}^2\left(\dfrac{\Delta t^3}{3}\right) & 0 & 0 & \sigma_{w_x}^2\left(\dfrac{\Delta t^2}{2}\right) & 0 & 0 \\ 0 & \sigma_{w_y}^2\left(\dfrac{\Delta t^3}{3}\right) & 0 & 0 & \sigma_{w_y}^2\left(\dfrac{\Delta t^2}{2}\right) & 0 \\ 0 & 0 & \sigma_{w_z}^2\left(\dfrac{\Delta t^3}{3}\right) & 0 & 0 & \sigma_{w_z}^2\left(\dfrac{\Delta t^2}{2}\right) \\ \sigma_{w_x}^2\left(\dfrac{\Delta t^2}{2}\right) & 0 & 0 & \sigma_{w_x}^2(\Delta t) & 0 & 0 \\ 0 & \sigma_{w_y}^2\left(\dfrac{\Delta t^2}{2}\right) & 0 & 0 & \sigma_{w_y}^2(\Delta t) & 0 \\ 0 & 0 & \sigma_{w_z}^2\left(\dfrac{\Delta t^2}{2}\right) & 0 & 0 & \sigma_{w_z}^2(\Delta t) \end{bmatrix} \qquad (4.14)$$

Here, σ_{w_x}, σ_{w_y}, and σ_{w_z} are the standard deviations for the random unmodeled

acceleration disturbances that act on the relative motion and Δt is the sampling time

interval.

4.3.2 Measurement Model

One of the most important components of the filter is the measurement partial matrix H_k which is used in updating the states and error covariance matrix with the measurements. Figure 4.1 depicts the LIDAR line of sight measurements that are processed by the filter: $\tilde{\rho}$ (range), $\tilde{\alpha}$ (azimuth angle), and $\tilde{\beta}$ (elevation angle). In proximity operations, the models for these measurements are given below.[35,68]

$$\tilde{\alpha} = tan^{-1}\left(\frac{i_y}{i_x}\right) + v_\alpha, \quad v_\alpha \sim N(0, \sigma_\alpha^2) \tag{4.15}$$

$$\tilde{\beta} = sin^{-1}(i_z) + v_\beta, \quad v_\beta \sim N(0, \sigma_\beta^2) \tag{4.16}$$

$$\tilde{\rho} = \rho + v_\rho, \quad v_\rho \sim N(0, \sigma_\rho^2) \tag{4.17}$$

where v_α, v_β, and v_ρ are azimuth, elevation, and range measurement noises respectively. In the absence of any other more suitable model of noise, these noises are assumed to be white, with zero mean and the standard deviations are equal to σ_α, σ_β, and σ_ρ respectively.
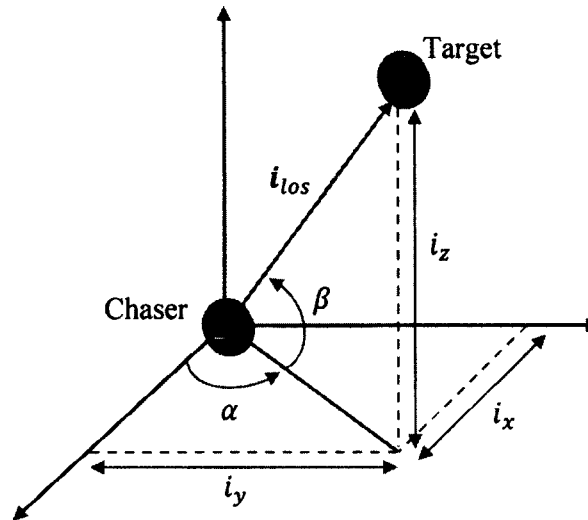
Figure 4.1 Line of Sight Vector

The unit line of sight vector can be written as a function of the relative position

vector in the chaser LVLH reference coordinate frame as

$$i_{los} = \begin{pmatrix} i_x \\ i_y \\ i_z \end{pmatrix} = \begin{pmatrix} c_\alpha c_\beta \\ s_\alpha c_\beta \\ s_\beta \end{pmatrix} = -\frac{\rho}{\rho} = -\frac{1}{\sqrt{x^2 + y^2 + z^2}} \begin{pmatrix} x \\ y \\ z \end{pmatrix} \qquad (4.18)$$

In particular, rewriting the measurement Equations (4.15)-(4.17) in the standard form of

Kalman filter vector notation leads to

$$\begin{pmatrix} \tilde{\alpha} \\ \tilde{\beta} \\ \tilde{\rho} \end{pmatrix} = \begin{pmatrix} tan^{-1}\left(\frac{i_y}{i_x}\right) \\ sin^{-1}(i_z) \\ \rho \end{pmatrix} + \begin{pmatrix} v_\alpha \\ v_\beta \\ v_\rho \end{pmatrix} \qquad (4.19)$$

Now the measurements partial matrix H_k is computed to be

$$H_k = \frac{\partial h}{\partial x}\bigg|_k = \begin{bmatrix} \dfrac{-y}{x^2 + y^2} & \dfrac{x}{x^2 + y^2} & 0 & 0 & 0 & 0 \\ \dfrac{xz}{\rho^2(x^2 + y^2)^{1/2}} & \dfrac{yz}{\rho^2(x^2 + y^2)^{1/2}} & -\dfrac{(x^2 + y^2)^{1/2}}{\rho^2} & 0 & 0 & 0 \\ \dfrac{x}{\rho} & \dfrac{y}{\rho} & \dfrac{z}{\rho} & 0 & 0 & 0 \end{bmatrix}_k \qquad (4.20)$$

and the associated measurement noise covariance matrix for the Kalman gain

computation is

$$R_k = \begin{bmatrix} \sigma_\alpha^2 & 0 & 0 \\ 0 & \sigma_\beta^2 & 0 \\ 0 & 0 & \sigma_\rho^2 \end{bmatrix} \qquad (4.21)$$

4.4 Guidance and Control Design

4.4.1 Guidance Algorithms

The guidance algorithms refer to the algorithms that specify the desired position

and velocity of the chaser during the given rendezvous scenario. Several guidance

algorithm approaches to move the chaser vehicle in the vicinity of the target vehicle were

described previously in Chapter 2. These algorithms are used to approach, to flyaround,

and to depart from a target vehicle in generalized orbits. The algorithms are general and able to transfer the chaser vehicle in any direction, decelerate while approaching the target vehicle, and accelerate when moving away. These algorithms are used to define the glideslope trajectory points and the required velocity change ΔV of the chaser to perform the required maneuver along the glideslope. The translation control algorithms compute the required ΔV to track the desired trajectory specified by the guidance algorithms. Two control techniques are presented in this section. The first technique is based on open loop control discrete thrust and the second technique is based on a continuous proportional-derivative controller in a closed loop GNC environment.

4.4.2 Open Loop Design

Let the uniform interval between any two successive pulses be $\Delta t = T/N$, where N is the number of thrust firings and T is the transfer time. The thrusters are thus fired at time $t_m = m\Delta t$ ($m = 0,1, ... N - 1$), and the mth pulse pushes the chaser from $\hat{p}(t_m)$ to $\hat{p}(t_{m+1})$, where

$$\begin{bmatrix} \hat{p}(t_{m+1}) \\ \dot{\hat{p}}(t_{m+1}) \end{bmatrix} = \begin{bmatrix} \phi_{pp}(t_{m+1}, t_m) & \phi_{p\dot{p}}(t_{m+1}, t_m) \\ \phi_{\dot{p}p}(t_{m+1}, t_m) & \phi_{\dot{p}\dot{p}}(t_{m+1}, t_m) \end{bmatrix} \begin{bmatrix} \hat{p}(t_m) \\ \dot{\hat{p}}(t_m) \end{bmatrix} \tag{4.22}$$

The arrival velocity at the mth location is $\dot{\hat{p}}^-(t_m)$, and the departure velocity to travel form $\hat{p}(t_m)$ to $\hat{p}(t_{m+1})$ is

$$\dot{\hat{p}}^+(t_m) = \phi_{p\dot{p}}^{-1}(t_{m+1}, t_m)\left(\hat{p}(t_{m+1}) - \phi_{pp}(t_{m+1}, t_m)\hat{p}(t_m)\right) \tag{4.23}$$

The incremental velocity at $\hat{p}(t_m)$ is then $\Delta V_m = \dot{\hat{p}}^+(t_m) - \dot{\hat{p}}^-(t_m)$, and the chaser will arrive at $\hat{p}(t_{m+1})$ with velocity equal to

$$\dot{\hat{p}}^-(t_{m+1}) = \phi_{\dot{p}p}(t_{m+1}, t_m)\hat{p}(t_m) + \phi_{\dot{p}\dot{p}}(t_{m+1}, t_m)\dot{\hat{p}}^+(t_m) \tag{4.24}$$

Now the chaser will arrive at its intended location given by

$$\widehat{p}(t_{m+1}) = \phi_{\rho\rho}(t_{m+1}, t_m)\widehat{p}(t_m) + \phi_{\rho\dot{\rho}}(t_{m+1}, t_m)\widehat{\dot{p}}^+(t_m) \qquad (4.25)$$

This dissertation presents two different methods to compute the state transition matrix ϕ. The first method is derived based on the TH model. In this derivation, the analytical closed form solution is developed to capture the target orbit eccentricity. The solution is valid under two conditions; first, the relative distance between the chase vehicle and the target vehicle is much less than the target orbit radius; and second, the environmental disturbances are considered absent. The second method to compute ϕ is based on the numerical approximate solution. Taylor series expansion was used to expand the matrix exponential and approximate the state transition matrix. The main benefit of this method is that the environmental disturbances such as J_2 and atmospheric drag perturbations can be considered in the development. Both methods to compute the state transition matrix in the navigation filter are evaluated in this chapter via numerical simulations.

4.4.3 Closed Loop Design

Instead of using discrete thrust for close proximity operations, a proportional-derivative controller is employed for the translation control. The translation control algorithm computes the required continuous thrust $\mathbf{f_c}$ produced by the chaser vehicle to track the desired trajectory specified by the guidance algorithm depending on the specified approach mode.[68]

$$\mathbf{U}_{\Delta V} = \mathbf{f_c} = K_\rho \delta\rho + K_{\dot{\rho}} \delta\dot{\rho}$$
$$\delta\rho = \rho_{des} - \widehat{\rho} \qquad (4.26)$$
$$\delta\dot{\rho} = \dot{\rho}_{des} - \widehat{\dot{\rho}}$$

The proportional and derivative control gains K_ρ and $K_{\dot{\rho}}$ are determined based on the desired natural frequency ω_ρ and damping ratio ζ_ρ of the translational control system.

$$K_\rho = \omega_\rho^2 I_{3\times3} \qquad K_{\dot{\rho}} = 2\zeta_\rho\omega_\rho I_{3\times3} \qquad\qquad (4.27)$$

Variables ρ_{des} and $\dot{\rho}_{des}$ are the desired relative position and relative velocity respectively, to be tracked by the chaser vehicle and they are defined by the guidance algorithms. It is worth noting that the equivalent continuous velocity increment ΔV, based on the continuous thrust, can be approximated for small Δt to be

$$\Delta V \approx U_{\Delta V}\Delta t \qquad\qquad (4.28)$$

4.5 Simulation Examples

The key metrics of the analysis fall into three main categories. The first is navigation performance, which is the how well the states are estimated by the filter. This is measured by the navigation error, the difference between the true states and the filter states. The second is trajectory control performance, which is a measure of how closely the chaser vehicle is able to follow the guidance algorithms. The third is fuel performance, or ΔV usage, and it is computed based on the proposed continuous or discrete thrust techniques described in the previous section.

4.5.1 Discrete Thrust Examples

The preceding guidance, navigation, and control algorithms are illustrated now through different examples. Initial conditions for the simulation are listed in Tables 4.1 and 4.2. A Simulink model is built using MATLAB software to demonstrate the multipulse open loop and continuous closed loop guidance transfer of the chaser to approach, to flyaround, and to depart from the target vehicle in any orbit, either circular or elliptic, given uncertain initial conditions, noisy measurements, and limited dynamics. This model consists of three main parts, guidance, navigation, and control, and it is based on the closed loop GN&C system block diagram shown in Chapter 3 (see Figure 3.3).

The TH and the LTV (Linear Time Varying) models are used separately in designing the navigation filter and in maneuver targeting of the guidance system.

Table 4.1 Navigation Filter Parameters

Parameter	Value
Initial Relative Position and Velocity Uncertainties	$\sigma_x = \sigma_y = \sigma_z = 33.3$ m $\sigma_{\dot{x}} = \sigma_{\dot{y}} = \sigma_{\dot{z}} = 0.01$ m/s
Process Noise	$\sigma_{w_x} = \sigma_{w_y} = 1 \times 10^{-7}$ km/s$^{3/2}$ $\sigma_{w_z} = 1 \times 10^{-8}$ km/s$^{3/2}$
Measurements Noise	$\sigma_\alpha = \sigma_\beta = 0.06$ deg, $\sigma_\rho = 0.5$ m
Simulation Step	0.1 s
Measurements Update	1 Hz

Table 4.2 Vehicles Orbital Elements

Parameter	Target	Chaser
a, km	6723.2576	6723.2576
e	0.1	0.1
i, deg	51.6467	51.6467
Ω, deg	188. 0147	188. 0147
ω, deg	174.3022	174.3022
f, deg	270.0882	270.0832

Considering the TH model, the performance of the navigation system is shown in Figures 4.2 and 4.3. In these figures, the thrusters are off and both target and chaser vehicles are in the same neighborhood initially (see Table 4.2). Figure 4.2 shows the relative position and relative velocity between the vehicles during simulation. Figure 4.3 depicts how accurately the navigation system can estimate the chaser's relative position and velocity. From this figure, the filter is able to converge within a few seconds and the

relative position and velocity can be accurately estimated to within 0.5m and 0.005m/s respectively.
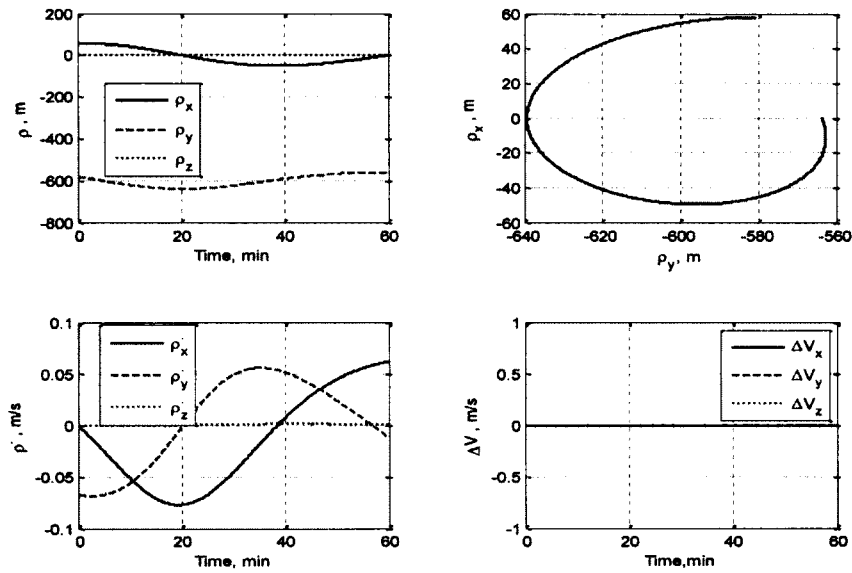

Figure 4.2 Relative Motion Without ΔV using TH Model
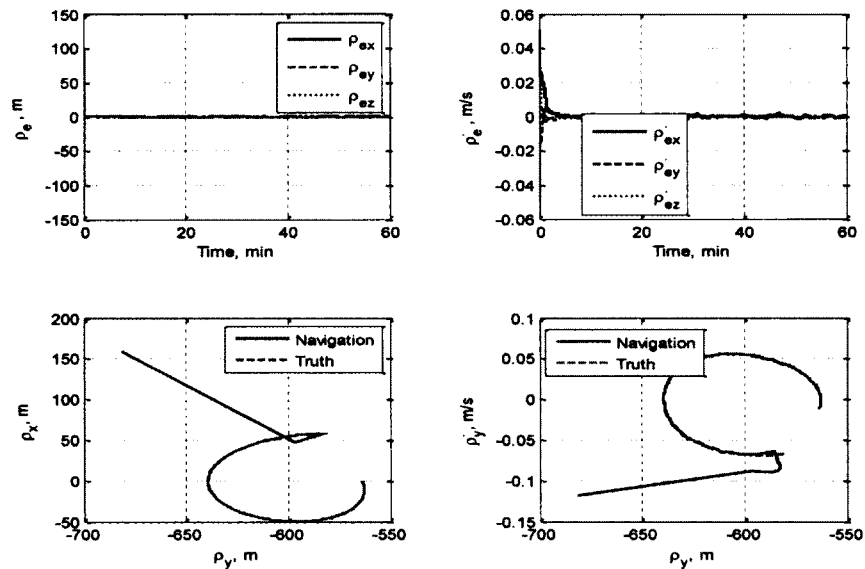
Figure 4.3 Navigation Performance Without ΔV using TH Model

All previous segments of the glideslope, inbound, flyaround, and outbound are now demonstrated through the following scenario. Inbound glideslope starts at [58 -580 0]m behind the target and ends at [0 -100 0]m, effected by 10 pulses in 20 minutes, decelerating the chaser from several meters per seconds to rest. After three minutes of station keeping at -100m behind the target, the chaser performs a 100m 20 pulse flyaround in 20 minutes. The chaser then stationkeeps behind the target for 3 minutes, followed by an outbound accelerating glideslope from -100m to -1000m in 10 pulses over 20 minutes. The chase then stays at rest at that location for another 3 min. The results of this scenario are shown in Figures 4.4-4.11. In all of these figures, different segments of the glideslope are shown, and the variations of in-plane relative motion of the chaser with respect to target vehicle are presented.

One observation here is that there are humps in the trajectory during the inbound, outbound, and flyaround phases. These humps are multipulse segmented deviations from the idealized rectilinear and circular glideslopes. These deviations can be reduced by increasing the number of pulses. The higher the number of pulses, the better the approximation to the glideslope. In all of the above glideslopes, the overall performance of the rendezvous and proximity operations are satisfactory.

The impulses ΔV are calculated using the estimated position, either from the Kalman filter or from knowledge of initial conditions, not the true position of the chaser. As such, the chaser is not expected to reach its intended destination exactly, but in the neighborhood thereof. Aided by the sensors, the initial estimation errors subside to an optimal level determined by the ratio of the process noise matrix Q_k and the measurement noise matrix R_k, defined earlier. Because of active range and angle measurements from

the LIDAR system and relatively small measurement errors, the true and estimated

relative position and velocity states are almost indistinguishable as seen in the figures.
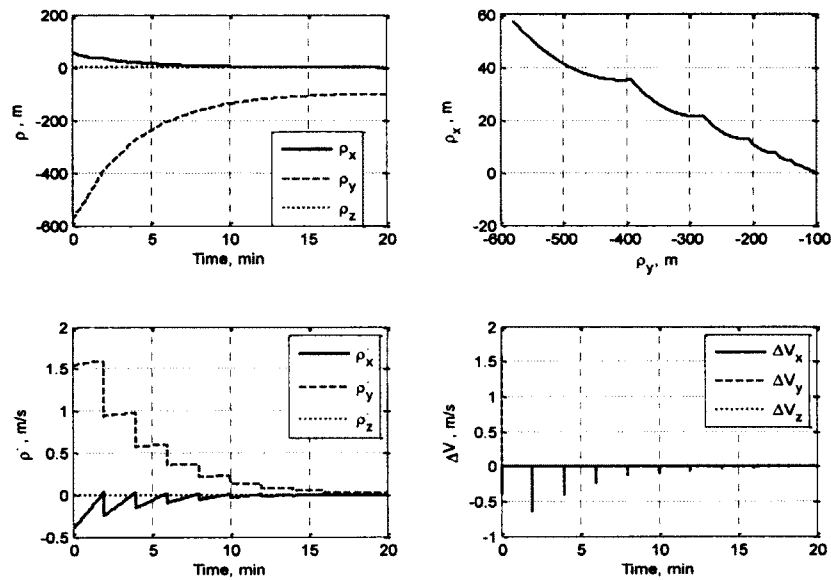
Figure 4.4 Relative Motion Multipulse Inbound Glideslope using TH Model
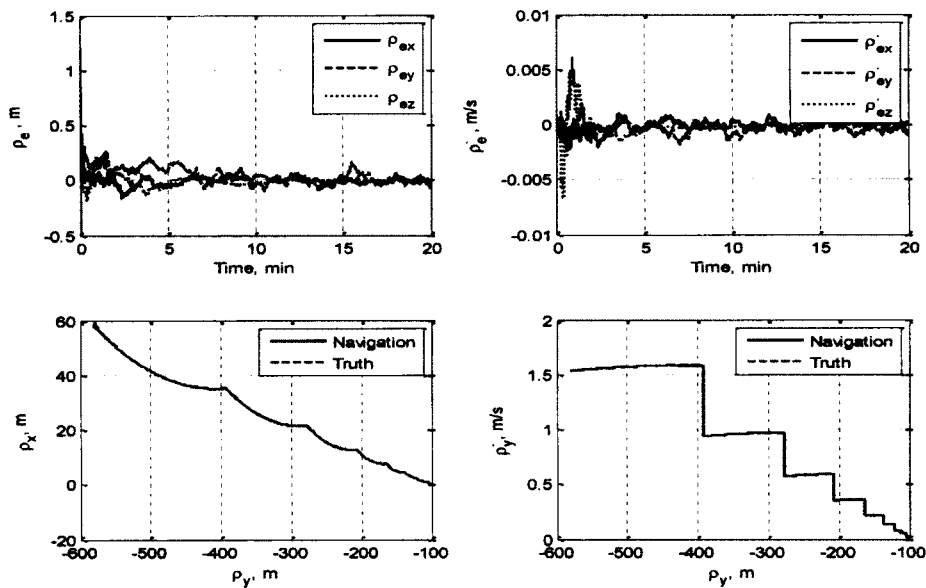
Figure 4.5 Inbound Navigation and Control Performance using TH Model
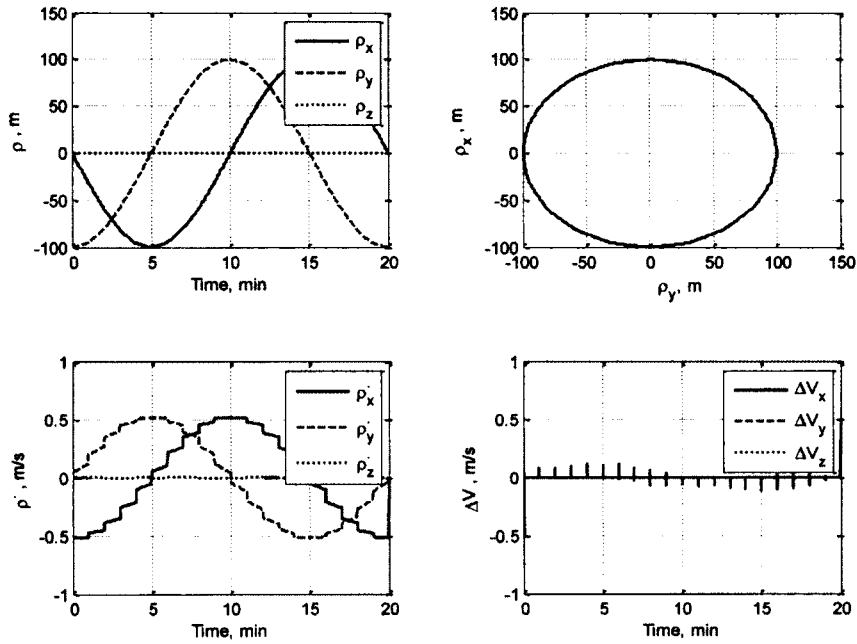
Figure 4.6 Relative Motion Multipulse Flyaround Glideslope using TH Model
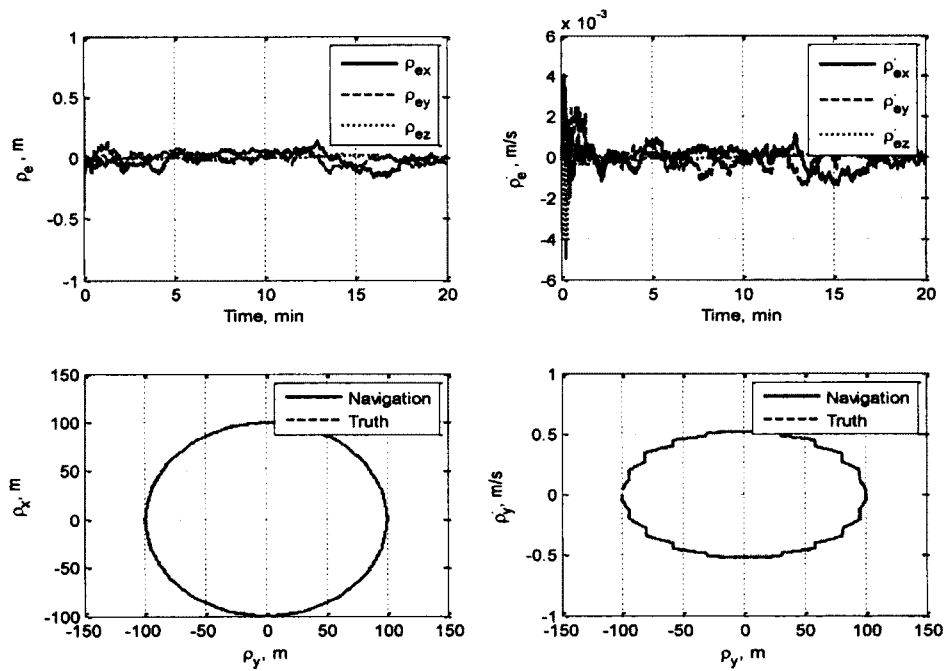
Figure 4.7 Flyaround Navigation and Control Performance using TH Model
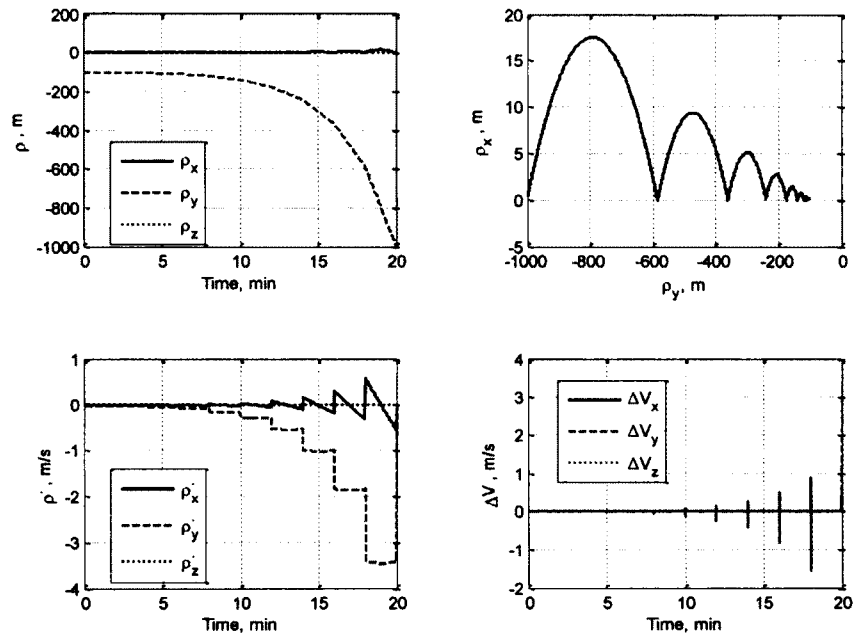
Figure 4.8 Relative Motion Multipulse Outbound Glideslope using TH Model
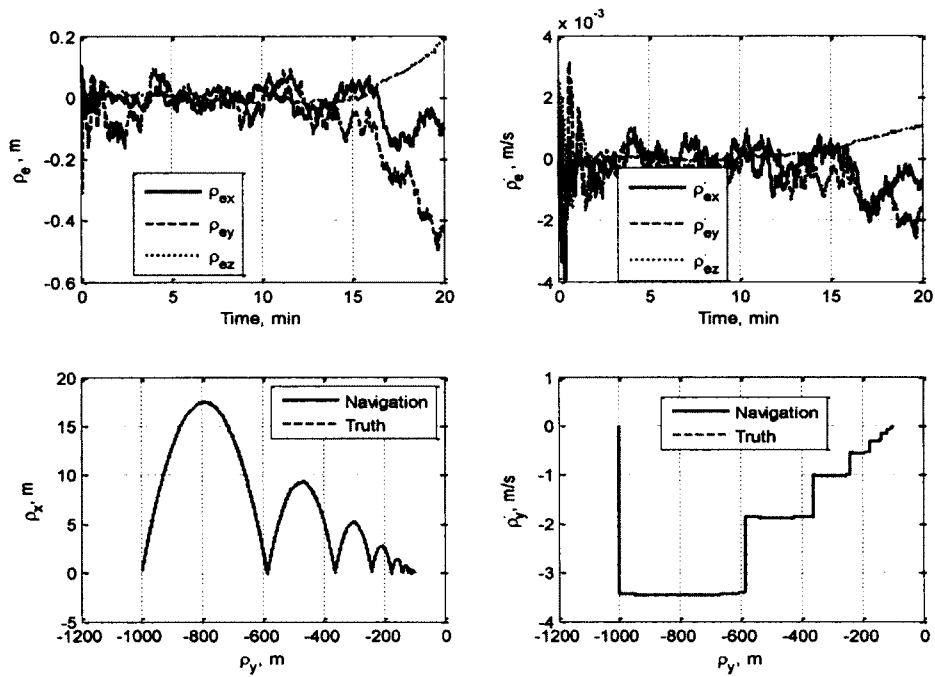
Figure 4.9 Outbound Navigation and Control Performance using TH Model
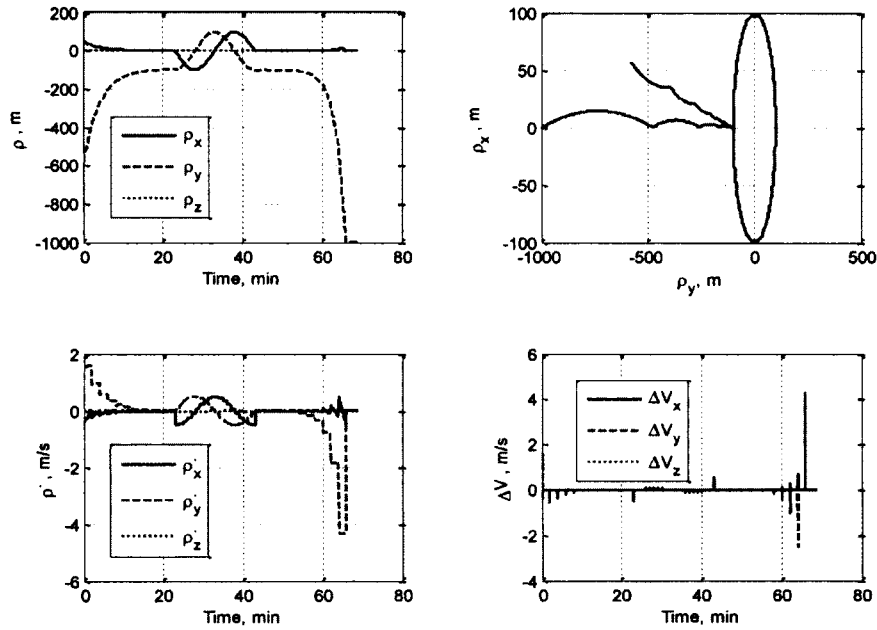
Figure 4.10 Relative Motion Multipulse Glideslope Scenario using TH Model
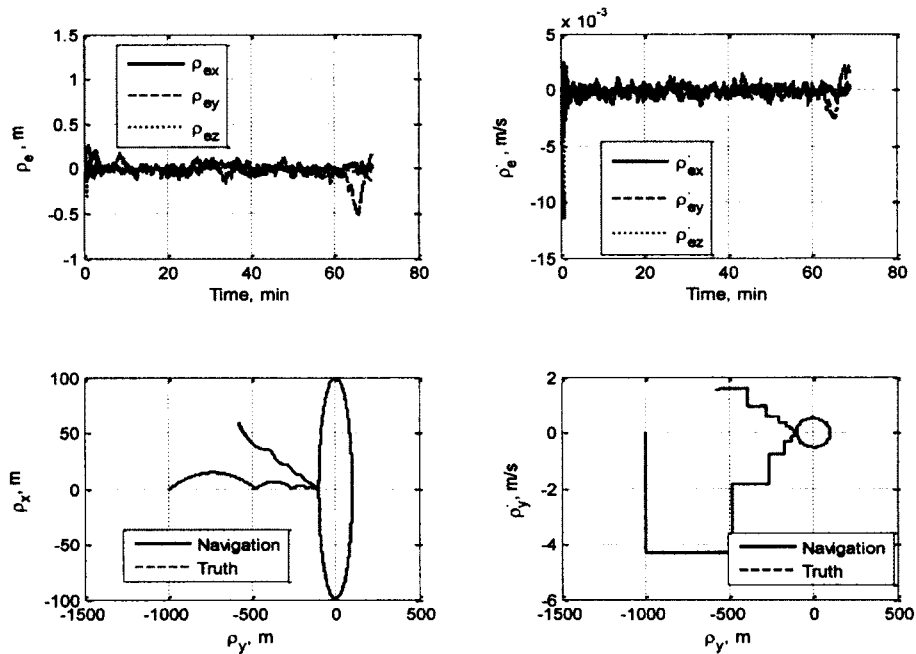
Figure 4.11 Scenario Navigation and Control Performance using TH Model

Like the TH model, the LTV model is considered here for simulation. The guidance, navigation, and control performance for the same inbound-flyaround-outbound scenario employed for this simulation are exactly the same as the first case, but use the LTV model. Figures 4.12-4.15 show the performance of this model. The filter navigation performance is presented in Figures 4.12 and 4.13 and the guidance and control performance is shown in Figures 4.14 and 4.15. From these figures, the proposed LTV, as well as TH models, are good candidates for designing the relative motion navigation system from the performance standpoint during different scenario segments.
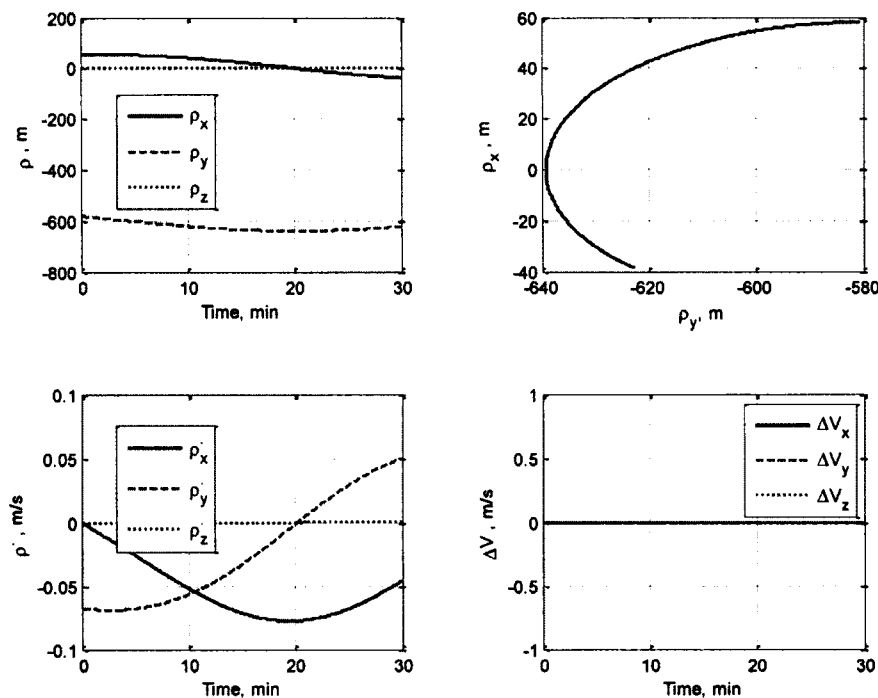
Figure 4.12 Relative Motion Without ΔV using LTV Model
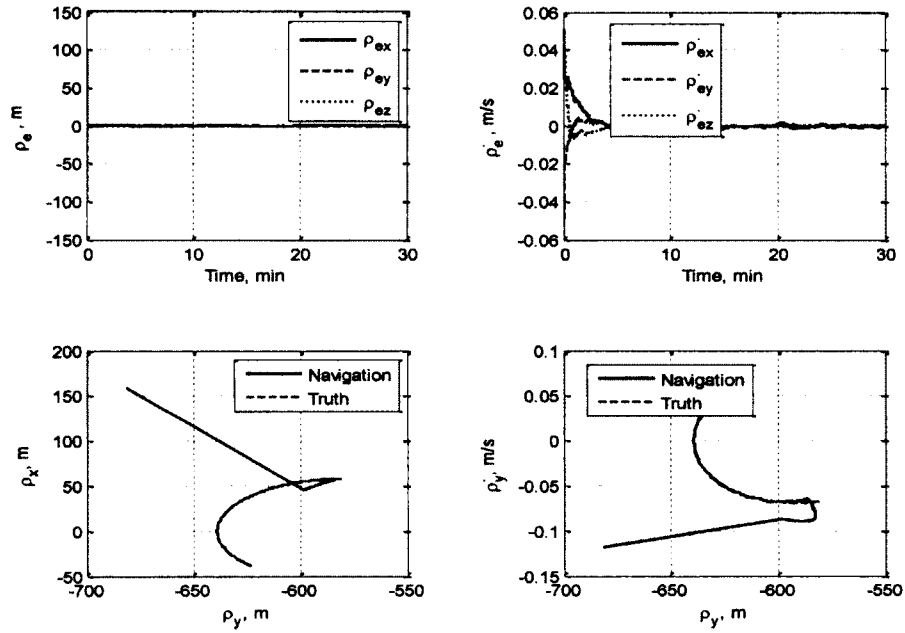
Figure 4.13 Navigation Performance Without ΔV using LTV Model
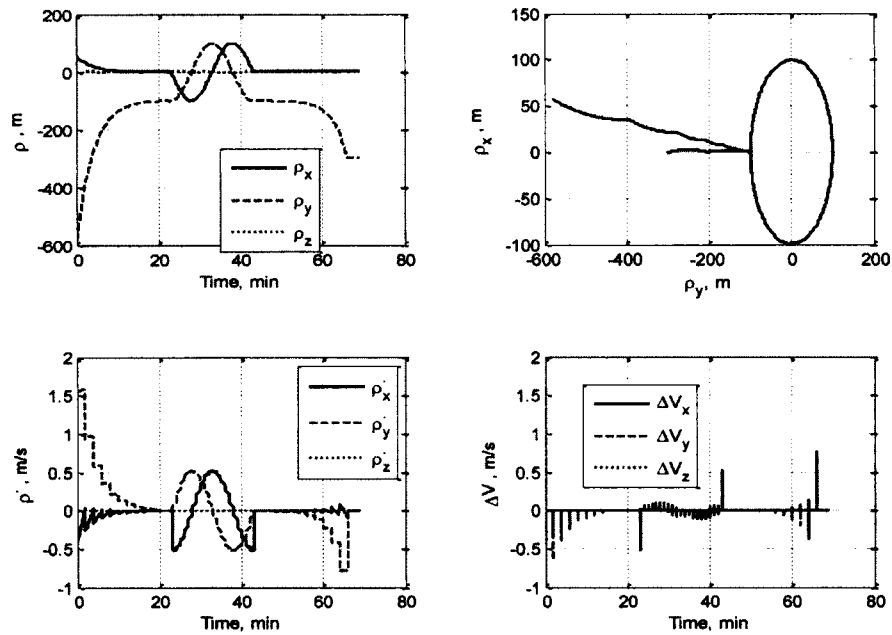
Figure 4.14 Relative Motion Multipulse Glideslope Scenario using LTV Model
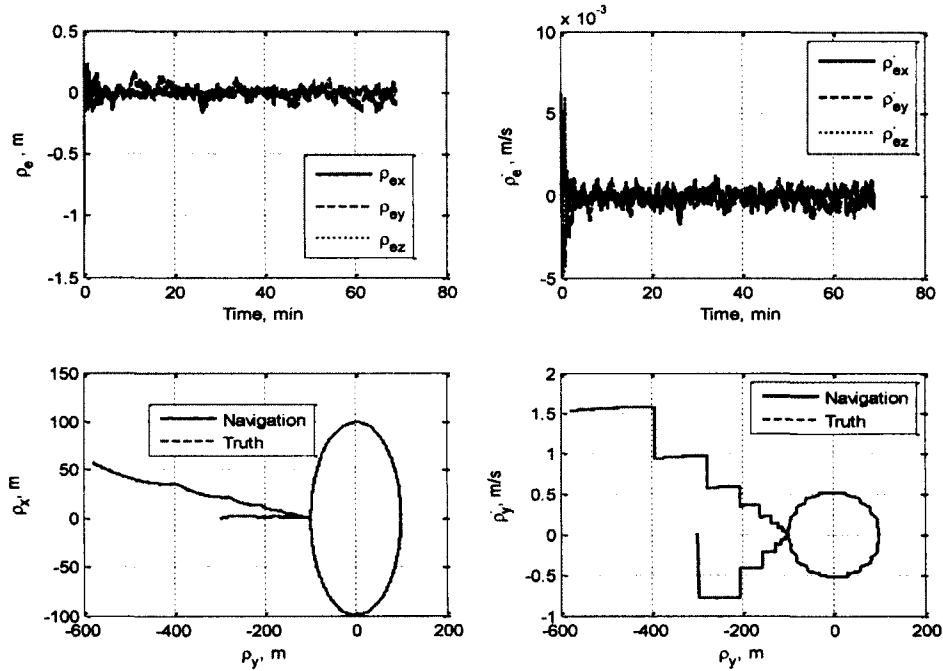
Figure 4.15 Scenario Navigation and Control Performance using LTV Model

4.5.2 Continuous Thrust Examples

Similar to the discrete thrust design approach to track a specific guidance algorithm, a continuous thrust design approach is considered in the following examples. In these examples, the required control thrust is produced based on a PD closed loop GN&C system. The controller parameters that were used in numerical simulation to compute the PD controller gains are listed in Table 4.3.

Table 4.3 PD Controller Parameters

Parameter	Value
Natural frequency	$\omega_\rho = 1/50 \ s^{-1}$
Damping ratio	$\zeta_\rho = 0.7$

A Simulink model is built using MATLAB software to demonstrate the closed loop guidance transfer of the chaser to approach and/or to depart from the target vehicle

in any orbit given uncertain initial conditions, noisy measurements, and limited dynamics. The proposed LTV model is used in designing the navigation filter and in maneuver targeting of the guidance system.

Simulations will be presented for two types of glideslope trajectories considering an eccentric orbit of the target under perturbations. First, the inbound glideslope in which the chaser is approaching the target vehicle is shown in Figures 4.16 and 4.17. In these figures, the chaser is located at station [58 -580 0]m, and from there it is commanded to approach the target at [0 -100 0]m. The relative position and velocity errors and ΔV continuous burns of the chaser are also shown in these figures. Second, the outbound glideslope is presented in the same figures in which the chaser is departing from the target. In these figures, the chaser starts to depart from 100m behind the target, leading to a new location 1000m behind the target. The corresponding performances of the guidance, navigation, and control for the outbound accelerating glideslope are shown also in these figures. Each segment of the glideslope is followed by 3 minutes of station keeping in which no thrust force is applied. From these figures, it is obvious that the PD design approach is a successful alternative approach to track a specific guidance trajectory.

It is worth noting that, like the discrete thrust, the continuous thrust ΔV is calculated using the estimated relative position and velocity, either from the Kalman filter or from knowledge of initial conditions, not the true relative position and velocity of the chaser. As such, the chaser is not expected to reach its intended place exactly, but in the neighborhood thereof.
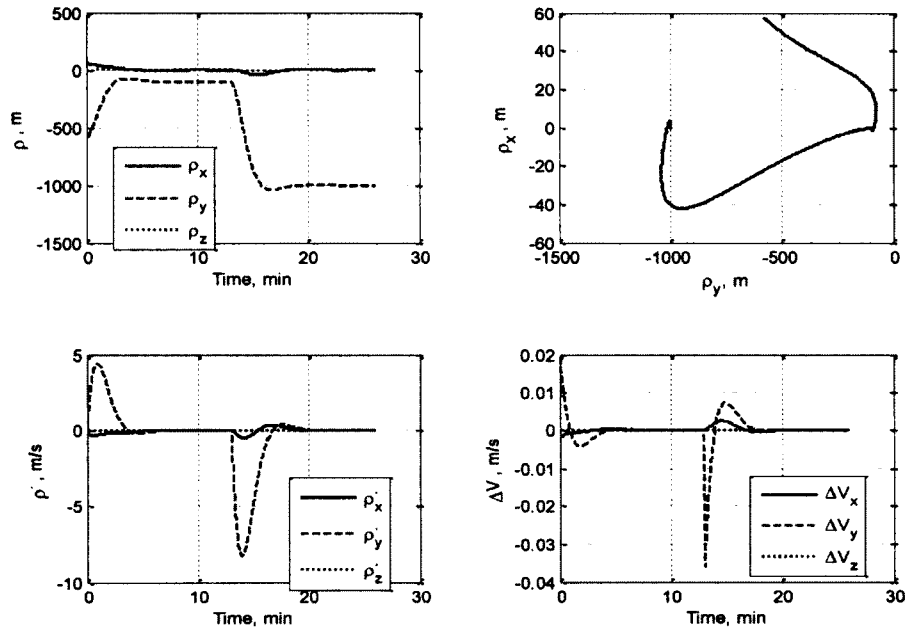
Figure 4.16 Relative Motion Inbound/Outbound Scenario using PD Control
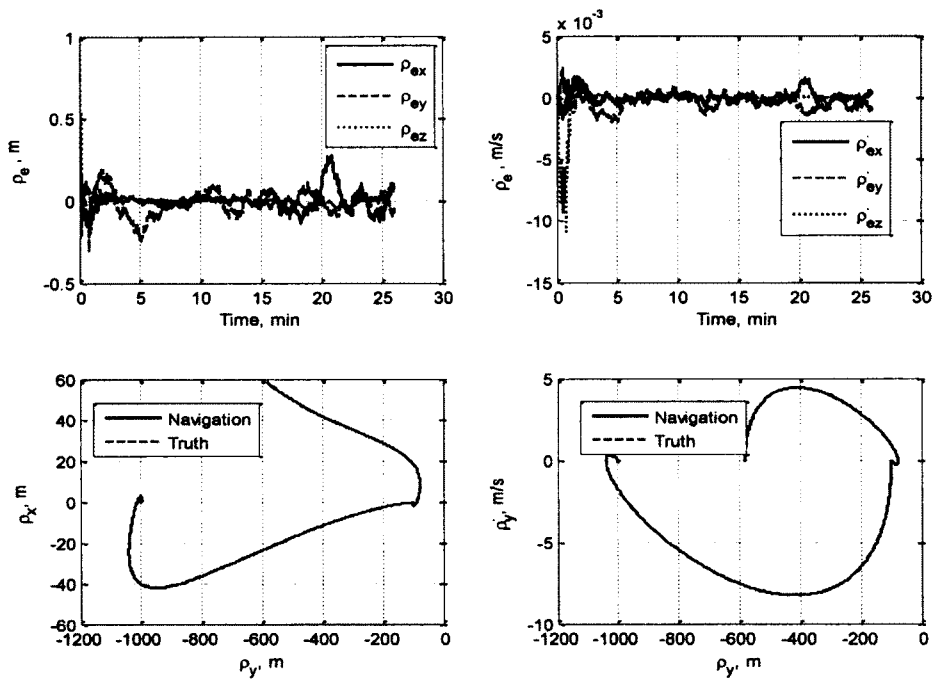
Figure 4.17 Scenario Navigation and Control Performance using PD Control

4.6 Summary

The results of this study indicate that the TH and the LTV models are clearly effective at estimating the relative position and velocity and controlling the relative trajectory. In addition, these models are not restricted to circular orbits but can be used as well for eccentric orbits. Furthermore, by using these models, simple guidance algorithms for glideslope and circumnavigation are developed to autonomously approach, flyaround and depart from a target vehicle. The relative navigation in this chapter utilizes range, azimuth, and elevation measurements from a LIDAR system and an extended Kalman filter. However, uncertainties like measurement biases and sensor misalignments are not considered here. The analyst must consider, in addition, attitude dynamics of the chaser and target, their attitude determination, and attitude control of the chaser to fire the thrusters in the right direction. These topics and others will be addressed in the next chapter.

5. GUIDANCE, NAVIGATION, AND CONTROL FOR SATELLITE PROXIMITY OPERATIONS

5.1 Introduction

During the mission scenarios, the chaser vehicle may need to track the attitude of the target vehicle to achieve proper docking maneuvers and or visual inspection tasks. The purpose of this chapter is to extend the work presented in previous chapters by expanding the plant true model, sensor and actuator dynamics, navigation system, and control system. [73,74] The plant true model is expanded to include states used to model the target and chaser attitude dynamics. Sensor and actuator models, biases, and misalignments are presented in the analysis. The state vector of the navigation system includes not only the relative states used to describe the relative motion between the target and chaser vehicles, but also the orientation states for both vehicles as well as parameter states that represent misalignments and biases. Unlike the translational motion control, the relative rotational control is a traditional feedback PD control system. In this chapter, an extended Kalman filter formulation is used also as in Chapter 4 to estimate the relative motion and chaser attitude using range and angle measurements for a LIDAR system, coupled with gyro and star tracker measurements of the chaser. Momentum wheels are assumed for attitude control, and thrusters are assumed for translational control. The effects of navigation filter, pointing algorithms, and control algorithms are included in the analysis.

This chapter is organized as follows. First, Section 5.2 presents the space vehicle attitude dynamics along with quaternion and Euler angle formulations. Section 5.3 is the modeling section, because it includes the integrated relative motion high fidelity models

along with attitude dynamics models for both chaser and target vehicles as well as sensors and actuators models with their corresponding models for misalignments and biases. In Section 5.4, the augmented navigation system, including measurement models, process noise matrices, and other filter parameters, is provided. Section 5.5 presents the relative translational and rotational controller that supports closed loop proximity attitude control operations and maneuvers. In Section 5.6, the accuracy and performance of the relative navigation and controller based on the high fidelity model are illustrated through different numerical examples and comparisons are made with the true nonlinear model. Finally, Section 5.7 concludes the work done in this chapter.

5.2 Spacecraft Attitude Modeling

The angular acceleration, angular velocity, and the angular position (orientation) of the spacecraft or any rigid body are governed by Euler's equations of motion. In particular, Euler's 2nd law describes the relationship between torques acting on a rigid body, and its angular motion. This law states that the moments applied to a rigid body relative to any fixed point equals the rate of change with respect to an inertia frame of angular momentum of the rigid body around that point.

Generally, the forces acting on the orbiting body also influence the rotational dynamics in the form of torques and moments. The sources of torques can be caused by gravity, aerodynamics, magnetics, solar radiation, thrusters offset and others.[43,55,75] Let the origin of the body reference frame be at the body's center of mass and express its angular velocity in body coordinates. Then, the angular momentum in body coordinates is simply the inertia matrix, I, times the body angular velocity, ω.

$$H = I\omega \tag{5.1}$$

Then, the rate of change of angular momentum (torque, τ) expressed in body coordinates becomes

$$\dot{H} = \tau = I\dot{\omega} + \omega \times I\omega \tag{5.2}$$

The angular acceleration becomes a function of the torques and the current angular velocity of the body.

$$\dot{\omega} = I^{-1}(\tau - \omega \times I\omega) \tag{5.3}$$

Integrating the angular acceleration determines the angular velocity.

The angular position or orientation of the spacecraft is expressed as a quaternion. In particular, q is expressed as a right handed quaternion with its scalar part as the fourth element. Quaternions and quaternion algebra are used extensively to describe the attitude of both target and chaser vehicles. For a thorough derivation and explanation of the quaternions and their associated algebra, see References 55 and 75. Once the quaternion is known, any vector can be rotated or transformed from one reference frame to another. Note that the quaternion derivative is directly related to the angular velocity of the spacecraft. The dynamic equations of motion of the quaternion are a function of the angular velocity, or

$$\dot{q}_I^b = \frac{1}{2}\omega \otimes q_I^b = \frac{1}{2}\Omega(\omega)q_I^b \tag{5.4}$$

where q_I^b defines the inertial to body quaternion, $\otimes$ indicates quaternion multiplication, and

$$\Omega = \begin{bmatrix} 0 & \omega_z & -\omega_y & \omega_x \\ -\omega_z & 0 & \omega_x & \omega_y \\ \omega_y & -\omega_x & 0 & \omega_z \\ \omega_x & -\omega_y & -\omega_z & 0 \end{bmatrix} \tag{5.5}$$

An alternative common way to represent the attitude of a rigid body is Euler angles. Euler angles are popular because they are easy to understand, easy to implement,

and they minimize the number of parameterizing variables required to construct the attitude rotation matrix. The main disadvantages of Euler angles are: (1) they employ associated angular functions that have singularities, (2) they are less accurate than Euler parameters when used to integrate incremental changes in attitude over time, and (3) they involve use of transcendental functions. These deficiencies in the Euler angle representation have led researchers to use unit quaternions as a parameterization of the attitude of a rigid body, especially in spacecraft applications which have a much wider range of attitude states than most aircraft. The relevant functions of unit quaternions have no singularities and the representation is well-suited to integrating the angular velocity of a body over time. The main disadvantages of using unit quaternions are: (1) they do not have intuitive physical meaning, (2) they must have unity norm to be a pure rotation, and (3) they require an extra variable to be processed.

Table 5.1 Euler Angle and Quataernion Rotation Matrices

$$R = R_1(\theta_3)R_2(\theta_2)R_3(\theta_1) = \begin{bmatrix} c_{\theta_2}c_{\theta_1} & c_{\theta_2}s_{\theta_1} & -s_{\theta_2} \\ s_{\theta_3}s_{\theta_2}c_{\theta_1} - c_{\theta_3}s_{\theta_1} & s_{\theta_3}s_{\theta_2}s_{\theta_1} + c_{\theta_3}c_{\theta_1} & s_{\theta_3}c_{\theta_2} \\ c_{\theta_3}s_{\theta_2}c_{\theta_1} + s_{\theta_3}s_{\theta_1} & c_{\theta_3}s_{\theta_2}s_{\theta_1} - s_{\theta_3}c_{\theta_1} & c_{\theta_3}c_{\theta_2} \end{bmatrix}$$

$$\theta_1 = \tan^{-1}(R_{12}/R_{11})$$
$$\theta_2 = -\sin^{-1}(R_{13})$$
$$\theta_3 = \tan^{-1}(R_{23}/R_{33})$$

$$R = \begin{bmatrix} 1 - 2(q_2^2 + q_3^2) & 2(q_1q_2 + q_3q_4) & 2(q_1q_3 - q_2q_4) \\ 2(q_2q_1 - q_3q_4) & 1 - 2(q_1^2 + q_3^2) & 2(q_2q_3 + q_1q_4) \\ 2(q_3q_1 + q_2q_4) & 2(q_3q_2 - q_1q_4) & 1 - 2(q_1^2 + q_2^2) \end{bmatrix}$$

$$q_1 = \frac{R_{23} - R_{32}}{2\Delta}, \qquad q_2 = \frac{R_{31} - R_{13}}{2\Delta}$$
$$q_3 = \frac{R_{12} - R_{21}}{2\Delta}, \qquad q_4 = \frac{\Delta}{2}$$
$$\Delta = (R_{11} + R_{22} + R_{33} + 1)^{\frac{1}{2}}$$

In this chapter, the Euler angle representation is only used for the purpose of visualizing the numerical simulation results for the chaser attitude determination and pointing control errors. Table 5.1 shows the attitude rotation matrix in terms of quaternions and Euler angles and how to construct the angles for the 3-2-1 rotation sequence and quaternion vector components. For complete information about Euler angle transformations and quaternion representations, refer to Reference 76.

5.3 Coupled Attitude and Orbit True Model

Equations (4.1) and (4.2) in Chapter 4 are used to model the true target orbit and relative motion dynamics, respectively. The Euler equation of motion is used to describe the attitude dynamics for both target and chaser vehicles and a quaternion formulation is used for attitude kinematics. The dynamics for both vehicles are given below as[68]

$$\dot{q}_i^t = \frac{1}{2}\omega^t \otimes q_i^t \tag{5.6}$$

$$\dot{\omega}^t = I_t^{-1}[\tau_t - \omega^t \times I_t\omega^t] \tag{5.7}$$

$$\tau_t = \tau_{t_g} + \tau_{t_d} \tag{5.8}$$

$$\dot{q}_i^c = \frac{1}{2}\omega^c \otimes q_i^c \tag{5.9}$$

$$\dot{\omega}^c = I_c^{-1}[\tau_c - \omega^c \times I_c\omega^c] \tag{5.10}$$

$$\tau_c = \tau_{c_c} + \tau_{c_g} + \tau_{c_d} \tag{5.11}$$

where $\otimes$ is the quaternion multiplication operator defined by[77]

$$p \otimes q = \begin{bmatrix} p_4 & p_3 & -p_2 & p_1 \\ -p_3 & p_4 & p_1 & p_2 \\ p_2 & -p_1 & p_4 & p_3 \\ -p_1 & -p_2 & -p_3 & p_4 \end{bmatrix} \begin{bmatrix} q_1 \\ q_2 \\ q_3 \\ q_4 \end{bmatrix} \tag{5.12}$$

and the i vehicle gravity gradient torque is defined by

$$\tau_{i_g} = 3\frac{\mu}{|R_i|^5}(R_i \times I_i R_i)$$ (5.13)

In Equations (5.6)-(5.13), the target states include the quaternion, q_i^t, that defines the orientation of the target with respect to the inertial frame, and the target's angular rate, ω^t. Similarly the chaser states are q_i^c and ω^c. I_t and I_c are the target and chaser inertia matrices, respectively. The gravity gradient torque, τ_{i_g}, for both vehicles (τ_{c_g} for the chaser and τ_{t_g} for the target) is derived from the point mass gravity models. The random disturbances, τ_{t_d} and τ_{c_d}, are included in the models to account for disturbance torques such as drag, solar radiation, and other unmodeled disturbances acting on each vehicle. These unmodeled disturbances are represented as uncorrelated white noise, with mean and variance defined by a trial and error technique outlined by Lear.[61] The control input, τ_{c_c}, is the torque executed by the actuators (momentum wheels) on the chaser spacecraft.

It is assumed that the available sensors are the LIDAR for tracking the target and an assembly of a star tracker and gyros for attitude determination. The parameter states for these sensors are modeled as first-order Markov processes with large time constants, causing them to behave like biases. The parameter states include the gyro bias b_ω^c, star camera misalignments ϵ_s^s, and LIDAR misalignments ϵ_l^l. The dynamic model associated with these states is given by

$$\dot{b}_\omega^c = -\frac{b_\omega^c}{\tau_b^\omega} + w_b^\omega$$ (5.14)

$$\dot{\epsilon}_s^s = -\frac{\epsilon_s^s}{\tau^s} + w^s$$ (5.15)

$$\dot{\epsilon}_l^l = -\frac{\epsilon_l^l}{\tau^l} + w^l$$ (5.16)

where w_b^ω, w^s, and w^l are white noise terms driving the first-order Markov processes, and τ_b^ω, τ^s, and τ^l are the corresponding time constants.

The actuator models used in the simulation include the momentum wheels for orientation control and thrusters for translational control. The mathematical model for the actual control torque generated by the wheels and the impulsive thrust by the thrusters are

$$\tau_{cc} = \delta T(\epsilon_\tau^c)[\{I_{3\times3} + Diag(f_\tau^c)\}\hat{\tau}_{cc} + b_\tau^c + v_\tau^c] \tag{5.17}$$

$$u_{c_{\Delta V}} = \delta T(\epsilon_{\Delta V}^c)[\{I_{3\times3} + Diag(f_{\Delta V}^c)\}\Delta V_c + b_{\Delta V}^c + v_{\Delta V}^c] \tag{5.18}$$

The generated torque and impulsive ΔV include errors such as noises v^c, biases b^c, scale factor biases f^c, and misalignments ϵ^c. These errors can be modeled also as white noise.

The simulation contains gyros, star tracker, and LIDAR sensor models. The models for these measurements are given by

Gyro Model: $\qquad \tilde{\omega}^c = \delta T(\epsilon_\omega^c)[\{I_{3\times3} + Diag(f_\omega^c)\}\omega^c + b_\omega^c + v_\omega^c] \tag{5.19}$

Star Tracker Model: $\quad \tilde{q}_I^s = \delta q(v_s^s) \otimes \delta q(\epsilon_s^s) \otimes q_c^s \otimes q_I^c \tag{5.20}$

LIDAR Model: $\quad \begin{pmatrix} \tilde{\alpha} \\ \tilde{\beta} \\ \tilde{\rho} \end{pmatrix} = \begin{pmatrix} tan^{-1}\left(\frac{i_y}{i_x}\right) \\ sin^{-1}(i_z) \\ \rho \end{pmatrix} + \begin{pmatrix} v_\alpha \\ v_\beta \\ v_\rho \end{pmatrix} \tag{5.21}$

where

$$i_{los}^l = \begin{pmatrix} i_x \\ i_y \\ i_z \end{pmatrix} = \begin{pmatrix} c_\alpha c_\beta \\ s_\alpha c_\beta \\ s_\beta \end{pmatrix} = T^{ll}T^{ls}T^{s\hat{s}}T^{\hat{s}l}T^{lT}\left(-\frac{\rho}{\rho}\right) \tag{5.22}$$

The gyro models include bias b_ω^c, scale factor bias f_ω^c, and angular random walk noise v_ω^c. The star camera model accounts for the uncertainty in the alignment of the star camera frame ϵ_s^s, with respect to the chaser frame and sensor noise v_s^s. The term q_c^s refers

to the fixed orientation of the star camera coordinate frame with respect to the chaser body coordinate frame. The LIDAR model includes angle measurement (azimuth α and elevation β) noises v_α, v_β and range (ρ) noise v_ρ. The transformation matrix denoted by T^{ab} is the transformation matrix used to transform any vector from coordinate b to coordinate a. The t^l_{los} is the line of sight vector in the LIDAR coordinate frame (see Figure 4.1 in previous chapter). The transformations T^{ll}, T^{ls}, $T^{s\delta}$, $T^{\delta l}$, and T^{lT} are a series of transformation matrices to transform the line of sight vector from the target local vertical local horizontal coordinate frame to the LIDAR coordinate frame. These transformations include errors from sensor misalignments, noises, and attitude determination errors.

The small angle rotations can be written in terms of quaternions as

$$\delta q(\theta) \approx \begin{bmatrix} \theta/2 \\ 1 \end{bmatrix} \tag{5.23}$$

or attitude matrices as

$$\delta T(\theta) \approx I - \theta^\times \tag{5.24}$$

where $\theta = \theta u$ is a small rotation vector, and $\theta^\times$ operating on vector ω is a cross product matrix defined by the ordinary cross product $\theta^\times \omega = \omega \times \theta$.

5.4 Coupled Attitude and Orbit Navigation Model

Again, Equations (4.3) and (4.4) in Chapter 4 are used to propagate the navigation model of the target orbit and relative model states. On the other hand, the navigation model for the target angular motion is used only to produce a reference attitude trajectory. This trajectory will be tracked by the chaser attitude control system.

$$\hat{\dot{q}}^t_i = \frac{1}{2} \hat{\omega}^t \otimes \hat{q}^t_i \tag{5.25}$$

$$\hat{\dot{\omega}}^t = \hat{I}_t^{-1}\left[\hat{\tau}_t - \hat{\omega}^t \times \hat{I}_t\hat{\omega}^t\right] \tag{5.26}$$

$$\hat{\tau}_t = \hat{\tau}_{tg} \tag{5.27}$$

For the chaser vehicle, the propagation of the state can be accomplished by using numerical integration techniques. However, in general, the gyro observations are sampled at a high rate (usually higher than, or at least equal to, the same rate as the vector attitude observations). A discrete propagation is usually sufficient. Discrete propagation can be derived using a power series approach[75]

$$\hat{q}_I^c(t) = \Omega(\hat{\omega}^c)\hat{q}_I^c(t_0) \tag{5.28}$$

where

$$\hat{\omega}^c = \tilde{\omega}^c - \hat{b}_\omega^c \tag{5.29}$$

$$\Omega(\hat{\omega}^c) = \begin{bmatrix} \cos\left(\frac{1}{2}\|\hat{\omega}^c\|\Delta t\right)I_{3\times3} - [\hat{\psi}^c \times] & \hat{\psi}^c \\ -\hat{\psi}^{c\,T} & \cos\left(\frac{1}{2}\|\hat{\omega}^c\|\Delta t\right) \end{bmatrix} \tag{5.30}$$

$$\hat{\psi}^c = \frac{\sin\left(\frac{1}{2}\|\hat{\omega}^c\|\Delta t\right)\hat{\omega}^c}{\|\hat{\omega}^c\|}$$

Finally, the propagation dynamic model for the error parameters is given by

$$\begin{bmatrix} \hat{b}_\omega^c(t) \\ \hat{e}_s^s(t) \\ \hat{e}_l^l(t) \end{bmatrix} = \phi_{Markov}(t, t_0)\begin{bmatrix} \hat{b}_\omega^c(t_0) \\ \hat{e}_s^s(t_0) \\ \hat{e}_l^l(t_0) \end{bmatrix} \tag{5.31}$$

where ϕ_{Markov} is defined as follows

$$\phi_{Markov} = \begin{bmatrix} e^{-\frac{\Delta t}{\tau_b^\omega}}I_{3\times3} & 0_{3\times3} & 0_{3\times3} \\ 0_{3\times3} & e^{-\frac{\Delta t}{\tau^s}}I_{3\times3} & 0_{3\times3} \\ 0_{3\times3} & 0_{3\times3} & e^{-\frac{\Delta t}{\tau^l}}I_{3\times3} \end{bmatrix} \tag{5.32}$$

The state vector of the Kalman filter is defined to be

$$x = [\rho \quad \dot{\rho} \quad \theta_c \quad b_\omega^c \quad \epsilon_s^s \quad \epsilon_l^l]^T \tag{5.33}$$

and Kalman filter matrices are given by

$$\phi_k = \begin{bmatrix} \phi_{REL} & 0_{6\times6} & 0_{6\times6} \\ 0_{6\times6} & \phi_{Attitude} & 0_{6\times6} \\ 0_{6\times6} & 0_{6\times6} & \phi_{Markov} \end{bmatrix} \tag{5.34}$$

$$P_k = \begin{bmatrix} P_{REL} & 0_{6\times6} & 0_{6\times6} \\ 0_{6\times6} & P_{Attitude} & 0_{6\times6} \\ 0_{6\times6} & 0_{6\times6} & P_{Markov} \end{bmatrix} \tag{5.35}$$

$$Q_k = \begin{bmatrix} Q_{REL} & 0_{6\times6} & 0_{6\times6} \\ 0_{6\times6} & Q_{Attitude} & 0_{6\times6} \\ 0_{6\times6} & 0_{6\times6} & Q_{Markov} \end{bmatrix} \tag{5.36}$$

The term ϕ_{REL} refers to the state transition matrix of relative motion defined in Chapter 2 by Equation (2.21) for the Tschauner-Hempel model, and by Equation (2.8) for the relative linear time varying model. The state vector contains θ_c instead of q_I^c because the quaternion must obey a normalization constraint, which can be violated by the linear measurement updates associated with the filter. The most common approach to overcome this shortfall involves using a multiplicative error quaternion, where, after neglecting higher order terms, the four component quaternion can effectively be replaced by a three component error vector θ_c.[75] Therefore, to within first-order, the quaternion update is given by

$$q_I^{c+} = \delta q(\theta_c) \otimes q_I^{c-} \tag{5.37}$$

and the discrete attitude error state transition matrix can also be derived using a power series approach to be

$$\phi_{Attitude} = \begin{bmatrix} \phi_{11}^c & \phi_{12}^c \\ \phi_{21}^c & \phi_{22}^c \end{bmatrix} \tag{5.38}$$

where

$$\phi_{11}^{c} = I_{3\times3} - [\widehat{\omega}^{c} \times]\frac{\sin(\|\widehat{\omega}^{c}\|\Delta t)}{\|\widehat{\omega}^{c}\|} + [\widehat{\omega}^{c} \times]^{2}\frac{\{1 - \cos(\|\widehat{\omega}^{c}\|\Delta t)\}}{\|\widehat{\omega}^{c}\|^{2}} \qquad (5.39)$$

$$\phi_{12}^{c} = [\widehat{\omega}^{c} \times]\frac{\{1 - \cos(\|\widehat{\omega}^{c}\|\Delta t)\}}{\|\widehat{\omega}^{c}\|^{2}} - I_{3\times3}\Delta t$$

$$\qquad (5.40)$$

$$- [\widehat{\omega}^{c} \times]^{2}\frac{\{\|\widehat{\omega}^{c}\|\Delta t - \sin(\|\widehat{\omega}^{c}\|\Delta t)\}}{\|\widehat{\omega}^{c}\|^{3}}$$

$$\phi_{21}^{c} = 0_{3\times3} \qquad (5.41)$$

$$\phi_{22}^{c} = I_{3\times3} \qquad (5.42)$$

The initial error covariance matrix P_0^{-} is given below for the relative motion, attitude, and error parameters.

$$P_{REL}^{-} = \begin{bmatrix} \sigma_x^2 & 0 & 0 & 0 & \varepsilon\sigma_x\sigma_y & 0 \\ 0 & \sigma_y^2 & 0 & \varepsilon\sigma_{\dot{x}}\sigma_y & 0 & 0 \\ 0 & 0 & \sigma_z^2 & 0 & 0 & 0 \\ 0 & \varepsilon\sigma_{\dot{x}}\sigma_y & 0 & \sigma_{\dot{x}}^2 & 0 & 0 \\ \varepsilon\sigma_x\sigma_{\dot{y}} & 0 & 0 & 0 & \sigma_{\dot{y}}^2 & 0 \\ 0 & 0 & 0 & 0 & 0 & \sigma_{\dot{z}}^2 \end{bmatrix} \qquad (5.43)$$

$$P_{Attitude}^{-} = \begin{bmatrix} \sigma_{w_b^{\theta}}^2 & 0_{3\times3} \\ 0_{3\times3} & \sigma_{w_b^{\omega}}^2 \end{bmatrix} \qquad (5.44)$$

$$P_{Markov}^{-} = \begin{bmatrix} \sigma_{w^s}^2 I_{3\times3} & 0_{3\times3} \\ 0_{3\times3} & \sigma_{w^l}^2 I_{3\times3} \end{bmatrix} \qquad (5.45)$$

Parameters σ_x, σ_y, and σ_z denote the standard deviation uncertainties of the relative position components and $\sigma_{\dot{x}}$, $\sigma_{\dot{y}}$, and $\sigma_{\dot{z}}$ are the standard deviation uncertainties for the relative velocity components. The standard deviations $\sigma_{w_b^{\theta}}$, $\sigma_{w_b^{\omega}}$, σ_{w^s}, and σ_{w^l} refer to the uncertainties of initial attitude, gyro biases, star tracker misalignments, and LIADR misalignments respectively. The discrete process noise matrix Q_k components of the relative motion can be approximated by

$$Q_{REL} = \begin{bmatrix} \sigma_{w_x}^2\left(\dfrac{\Delta t^3}{3}\right) & 0 & 0 & \sigma_{w_x}^2\left(\dfrac{\Delta t^2}{2}\right) & 0 & 0 \\ 0 & \sigma_{w_y}^2\left(\dfrac{\Delta t^3}{3}\right) & 0 & 0 & \sigma_{w_y}^2\left(\dfrac{\Delta t^2}{2}\right) & 0 \\ 0 & 0 & \sigma_{w_z}^2\left(\dfrac{\Delta t^3}{3}\right) & 0 & 0 & \sigma_{w_z}^2\left(\dfrac{\Delta t^2}{2}\right) \\ \sigma_{w_x}^2\left(\dfrac{\Delta t^2}{2}\right) & 0 & 0 & \sigma_{w_x}^2(\Delta t) & 0 & 0 \\ 0 & \sigma_{w_y}^2\left(\dfrac{\Delta t^2}{2}\right) & 0 & 0 & \sigma_{w_y}^2(\Delta t) & 0 \\ 0 & 0 & \sigma_{w_z}^2\left(\dfrac{\Delta t^2}{2}\right) & 0 & 0 & \sigma_{w_z}^2(\Delta t) \end{bmatrix} \tag{5.46}$$

$$Q_{Attitude} = \begin{bmatrix} \left(\sigma_{v_\omega^c}^2\Delta t + \dfrac{1}{3}\sigma_{v_b^\omega}^2\Delta t^3\right)I_{3\times3} & -\left(\dfrac{1}{2}\sigma_{v_b^\omega}^2\Delta t^2\right)I_{3\times3} \\ -\left(\dfrac{1}{2}\sigma_{v_b^\omega}^2\Delta t^2\right)I_{3\times3} & -\left(\sigma_{v_b^\omega}^2\Delta t\right)I_{3\times3} \end{bmatrix} \tag{5.47}$$

$$Q_{Markov} = \begin{bmatrix} \sigma_{v^s}^2\Delta t I_{3\times3} & 0_{3\times3} \\ 0_{3\times3} & \sigma_{v^l}^2\Delta t I_{3\times3} \end{bmatrix} \tag{5.48}$$

Here, σ_{w_x}, σ_{w_y}, and σ_{w_z} are the standard deviations for the random unmodeled acceleration disturbances that act on the relative motion during the sample time period Δt and $\sigma_{v_\omega^c}$, $\sigma_{v_b^\omega}$, σ_{v^s}, and σ_{v^l} are the random process uncertainty noises for gyros, gyro biases, star tracker misalignments, and LIADR misalignments respectively.

The measurements sensitivity matrices H_k and sensor measurements noise matrices R_k are defined for both star sensor and LIDAR as

$$H_k = \begin{bmatrix} H_k^{lidar} \\ H_k^s \end{bmatrix} \tag{5.49}$$

$$R_k = \begin{bmatrix} R_k^{lidar} & 0_{3\times3} \\ 0_{3\times3} & R_k^s \end{bmatrix} \tag{5.50}$$

The measurement partials for the azimuth, elevation, and range measurements are computed with the help of the LIDAR measurement range vector. Utilizing Equation

(5.22) and small angle approximations lead to the following equation for the relative range in terms of the navigation states.

$$\boldsymbol{\rho}^l = \rho \begin{pmatrix} C_\alpha C_\beta \\ S_\alpha C_\beta \\ S_\beta \end{pmatrix} = \left[I_{3\times3} - \boldsymbol{\epsilon}_l^{l\times} \right] \left[I_{3\times3} - \boldsymbol{\epsilon}_s^{s\times} \right] \left[I_{3\times3} - \boldsymbol{\theta}_c^{\times} \right] T^{sl} (q_i^{c-}) T^{lT} (-\boldsymbol{\rho}) \qquad (5.51)$$

Using the chain rule, the partial of the range vector with respect to the navigation states can be expressed as[68]

$$\frac{\partial \boldsymbol{\rho}^l(x)}{\partial x} \bigg|_{\hat{x}} = \left[\frac{\partial \boldsymbol{\rho}^l(x)}{\partial \alpha} \frac{\partial \alpha(x)}{\partial x} + \frac{\partial \boldsymbol{\rho}^l(x)}{\partial \beta} \frac{\partial \beta(x)}{\partial x} + \frac{\partial \boldsymbol{\rho}^l(x)}{\partial \rho} \frac{\partial \rho(x)}{\partial x} \right]_{\hat{x}} \qquad (5.52)$$

$$= \left[(\rho \boldsymbol{p}_\alpha^l) \boldsymbol{h}_\alpha + (\rho \boldsymbol{p}_\beta^l) \boldsymbol{h}_\beta + \boldsymbol{p}_\rho^l \boldsymbol{h}_\rho \right]_{\hat{x}}$$

$$\boldsymbol{p}_\alpha^l = \begin{bmatrix} -C_\beta S_\alpha \\ C_\beta C_\alpha \\ 0 \end{bmatrix}, \qquad \boldsymbol{p}_\beta^l = \begin{bmatrix} -S_\beta C_\alpha \\ -S_\beta S_\alpha \\ C_\beta \end{bmatrix}, \qquad \boldsymbol{p}_\rho^l = \begin{bmatrix} C_\beta C_\alpha \\ C_\beta S_\alpha \\ S_\beta \end{bmatrix} \qquad (5.53)$$

The measurement geometry can now be computed by taking advantage of the property that $\boldsymbol{p}_\alpha^l$, $\boldsymbol{p}_\beta^l$, and $\boldsymbol{p}_\rho^l$ are orthogonal to each other and taking the dot product with respect to each.

$$\boldsymbol{h}_\alpha = \frac{(\boldsymbol{p}_\alpha^l)^T}{\rho C_\beta^2} \left[\frac{\partial \boldsymbol{\rho}^l(x)}{\partial x} \right], \qquad \boldsymbol{h}_\beta = \frac{(\boldsymbol{p}_\beta^l)^T}{\rho} \left[\frac{\partial \boldsymbol{\rho}^l(x)}{\partial x} \right], \qquad \boldsymbol{h}_\rho = (\boldsymbol{p}_\rho^l)^T \left[\frac{\partial \boldsymbol{\rho}^l(x)}{\partial x} \right] \qquad (5.54)$$

Evaluation of the relative range vector with respect to the navigation states yields

$$\left[\frac{\partial \boldsymbol{\rho}^l(x)}{\partial x} \right] = \begin{bmatrix} -T^{lT} & 0_{3\times3} & -T^{ll} T^{ls} [\boldsymbol{\rho}^s \times] & 0_{3\times3} & -T^{ll} [\boldsymbol{\rho}^s \times] & -[\boldsymbol{\rho}^l \times] \end{bmatrix} \qquad (5.55)$$

Now, the LIDAR measurement sensitivity matrix and covariance matrix can be written as

$$H_k^{lidar} = \begin{bmatrix} \hat{\boldsymbol{h}}_\alpha & \hat{\boldsymbol{h}}_\beta & \hat{\boldsymbol{h}}_\rho \end{bmatrix}^T \qquad (5.56)$$

and

$$R_k^{lidar} = \begin{bmatrix} \sigma_\alpha^2 & 0 & 0 \\ 0 & \sigma_\beta^2 & 0 \\ 0 & 0 & \sigma_\rho^2 \end{bmatrix} \tag{5.57}$$

When processing star tracker data, a derived measurement is calculated.[68] This quantity is effectively the residual to be processed by the filter.

$$\begin{bmatrix} \frac{1}{2}\tilde{z}_s \\ 1 \end{bmatrix} = \tilde{q}_I^s \otimes [\hat{q}_c^I \otimes \hat{q}_s^c \otimes \delta\hat{q}(\hat{\epsilon}_s^s)] \tag{5.58}$$

The derived star tracker measurement can be written as a function of the navigation states as

$$\tilde{z}_s = h_s(x) + v_s^s = \theta_c^s + \epsilon_s^s + v_s^s \tag{5.59}$$

Therefore, the measurement sensitivity matrix for the star tracker can be derived to be

$$H_k^s = \frac{\partial h_s(x)}{\partial x}\bigg|_{\hat{x}} = [0_{6\times6} \quad I_{3\times3} \quad 0_{3\times3} \quad I_{3\times3} \quad 0_{3\times3}] \tag{5.60}$$

and the star tracker measurement covariance is

$$R_k^s = \sigma_s^2 I_{3\times3} \tag{5.61}$$

5.5 Integrated Relative Motion Controller

For close proximity operations, a proportional-derivative controller is employed for the rotational control. The commanded torques for the chaser spacecraft to match its orientation with the target vehicle are computed as

$$\hat{\tau}_{cc} = K_q \delta\hat{q} + K_\omega \delta\hat{\omega} \tag{5.62}$$

where

$$\delta\hat{q} = \delta\hat{q}_{e_v} \delta\hat{q}_{e_s} \tag{5.63}$$

$$\delta\hat{\omega} = \hat{\omega}_{des}^c - \hat{\omega}^c \tag{5.64}$$

and

$$\hat{q}^c_{i_{des}} = \hat{q}^t_i \qquad (5.65)$$

$$\hat{\omega}^c_{des} = T^{ct}\hat{\omega}^t \qquad (5.66)$$

$$\hat{q}_e = \hat{q}^c_{i_{des}} \otimes \hat{q}^c_i = \begin{pmatrix} \delta\hat{q}_{e_v} \\ \delta\hat{q}_{e_s} \end{pmatrix} \qquad (5.67)$$

$\hat{q}^c_{i_{des}}$ and $\hat{\omega}^c_{des}$ are the desired orientation and angular velocity, respectively, to be tracked by the chaser vehicle. The angular offset and angular rate offset between target and chaser are denoted by $\delta\hat{q}_e$ and $\delta\hat{\omega}$, respectively. The proportional and derivative control gains K_q and K_ω are determined based on the desired natural frequency ω_θ and damping ratio ζ_θ of the attitude control system, and the moment of inertia of the chaser spacecraft I_c.[78]

$$K_q = \omega^2_\theta I_c, \qquad K_\omega = 2\zeta_\theta\omega_\theta I_c \qquad (5.68)$$

On the other hand, the translation control algorithm computes the required ΔV based on two different techniques described earlier in Chapter 4. The first technique is to generate discrete thrust that is based on the TH model to track the desired trajectory specified by the guidance algorithms, while the second one is based on the PD closed loop GN&C continuous thrust design approach. Both techniques are illustrated through the following numerical examples.

5.6 Simulation Examples

Although there are a variety of mission parameters that may be of interest to analyze, the research in this chapter primarily focuses on the performance of the guidance, navigation, and control of the chaser vehicle. For close proximity, the

rotational dynamics of the chaser play an important role and influence the overall performance of the mission. As a consequence, a six degree of freedom, nonlinear, high fidelity simulation has been employed, and highlights of the rotational performance are mentioned to support the navigation and ΔV performance analysis.

Table 5.2 Simulation Initial Conditions

Initial Conditions	Parameter	Value
Inertia		
Chaser	I_c	$\begin{bmatrix} 1.31 & 0 & 0 \\ 0 & 10.220 & 0 \\ 0 & 0 & 10.65 \end{bmatrix} \times 10^6$ kg-m^2
Target	I_t	$\begin{bmatrix} 128 & 0 & 0 \\ 0 & 107 & 0 \\ 0 & 0 & 201 \end{bmatrix} \times 10^6$ kg-m^2
Initial Relative Attitude Errors	$\delta\phi, \delta\theta, \delta\psi$	$[7.5 \quad -7.5 \quad 7.5]$ deg
Control Parameters		
Rotational natural frequency	ω_θ	1/30 s^{-1}
Rotational damping ratio	ζ_θ	0.7
Translational natural frequency	ω_ρ	1/50 s^{-1}
Translational damping ratio	ζ_ρ	0.7
Unmodeled Disturbances		
Rotational disturbances	τ_{i_d}	10^{-6} kg-km^2/s^2
Translational disturbances	f_w	10^{-8} km/s^2
Sensors Errors		
Gyro error (3σ)	Drift rate Random walk	3 deg/hr/axis 0.05 mrad/s$^{1/2}$
Star Tracker error (3σ)	Misalignment Noise Measurements	1 mrad/axis 1 mrad/axis 1 Hz
LIDAR error (3σ)	Misalignment Noise Measurements	1 mrad/axis $[1$ mrad $\quad$ 1 mrad $\quad$ 0.5 m$]$ 1 Hz

As mentioned earlier in Chapter 4, three key metrics are considered for the analysis, and they include: (1) the navigation performance, (2) trajectory control performance, and (3) fuel performance, or ΔV usage. These metrics are illustrated now through two main scenarios. Initial conditions for the first scenario are listed in Tables 4.1 and 4.2 from the previous chapter, along with Table 5.2 from this chapter. These

tables include the vehicle initial parameters (orbital and attitude) and all the other uncertain parameters in the simulation that need to be initialized for the navigation filter and controller.

The TH and LTV models are used separately in designing the navigation filter and in maneuver targeting of the guidance system. Considering the TH model, the performance of the navigation system is shown in Figures 5.1 and 5.2. In these figures, the thrusters are off and both target and chaser vehicles are in the same neighborhood initially (see Table 4.2). Figure 5.1 shows the relative position and relative velocity between the vehicles during simulation. Figure 5.2 depicts how accurately the navigation system can estimate the chaser's relative position and velocity. From this figure, the filter is able to converge within a few minutes and the relative position and velocity can be accurately estimated to within the accuracy of the sensors. The chaser attitude dynamics, navigation errors, and PD control tracking performance data are shown in Figures 5.3 and 5.4. As indicated by these figures, the chaser attitude navigation system is able to converge quickly, and the chaser attitude PD controller can track the target attitude and angular velocity trajectories. The uncertain parameters (gyros biases, star tracker misalignments, and LIDAR misalignments), navigation error performance, and required attitude control wheel torques to perform the tracking maneuvers, are shown in Figure 5.5. In this figure, the navigation system performance indicates that the gyros biases are converged, while the misalignment navigation errors are bounded during the period of simulation.
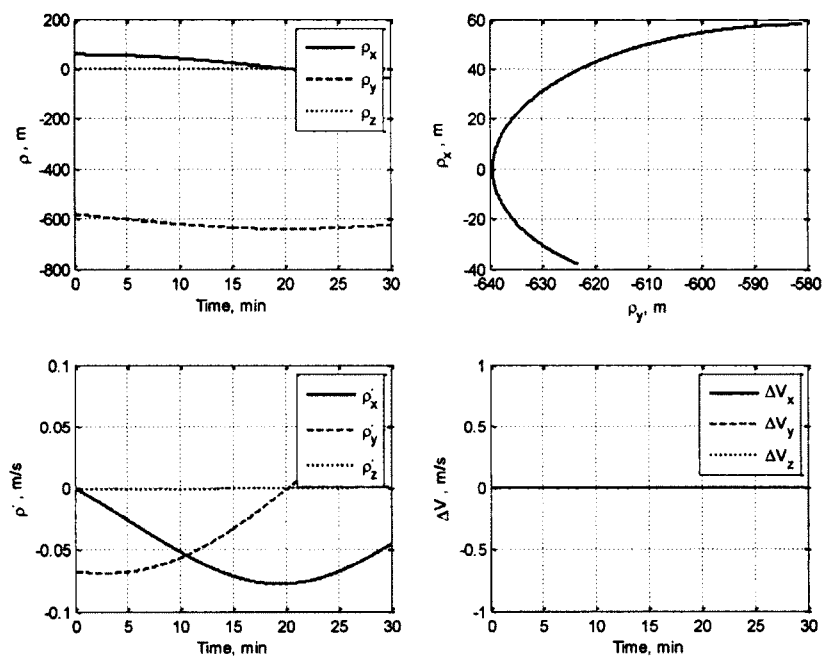
Figure 5.1 Relative Motion Without ΔV using TH Model
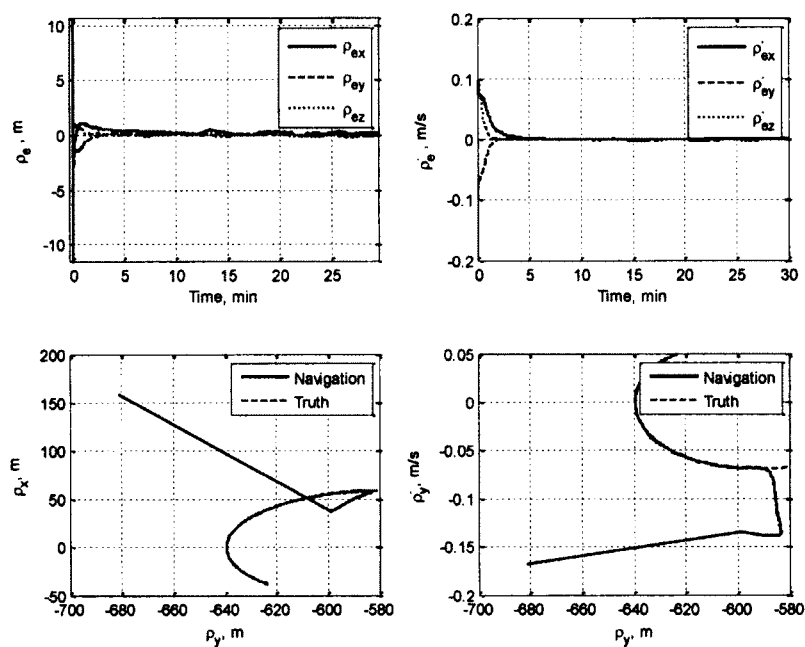
Figure 5.2 Navigation Performance Without ΔV using TH Model
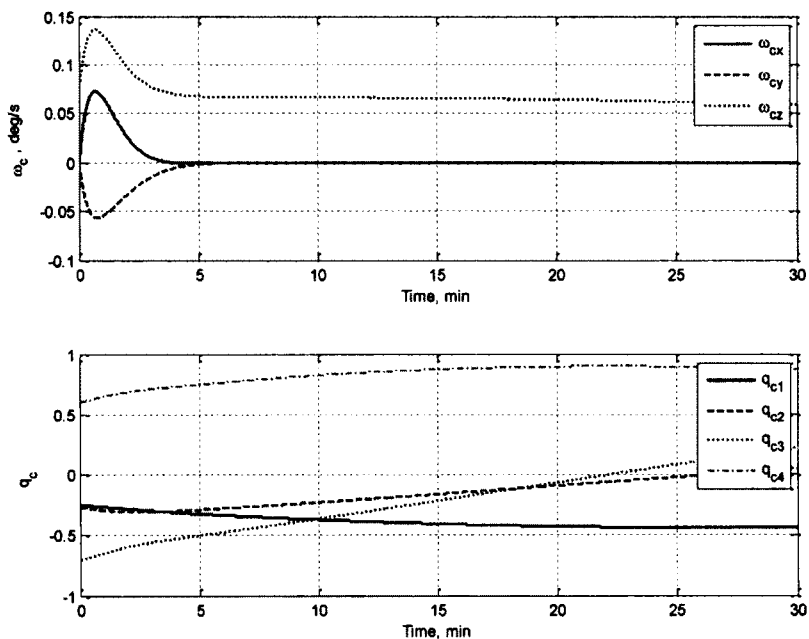
Figure 5.3 Chaser Attitude Dynamics
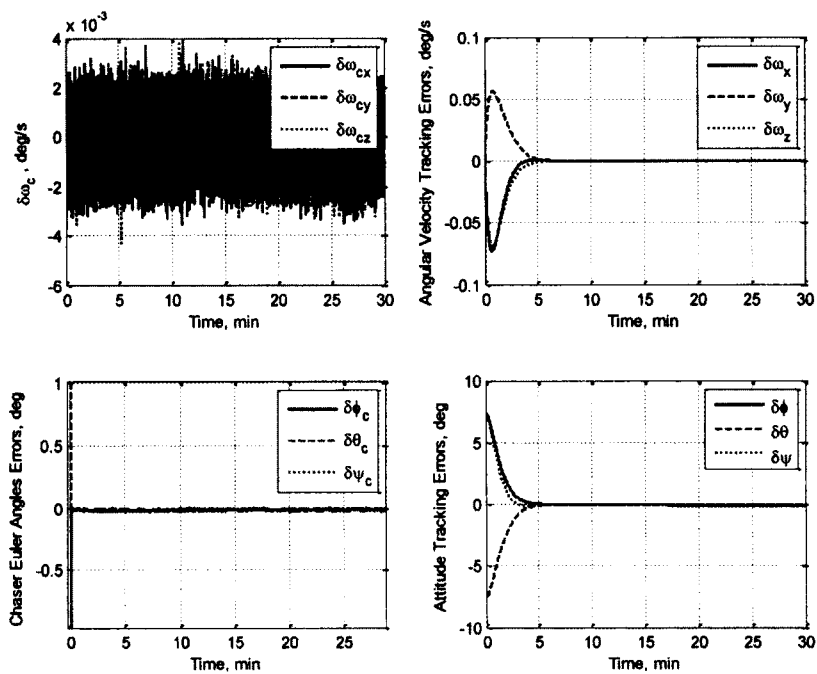
Figure 5.4 Chaser Attitude Navigation and Control Performance
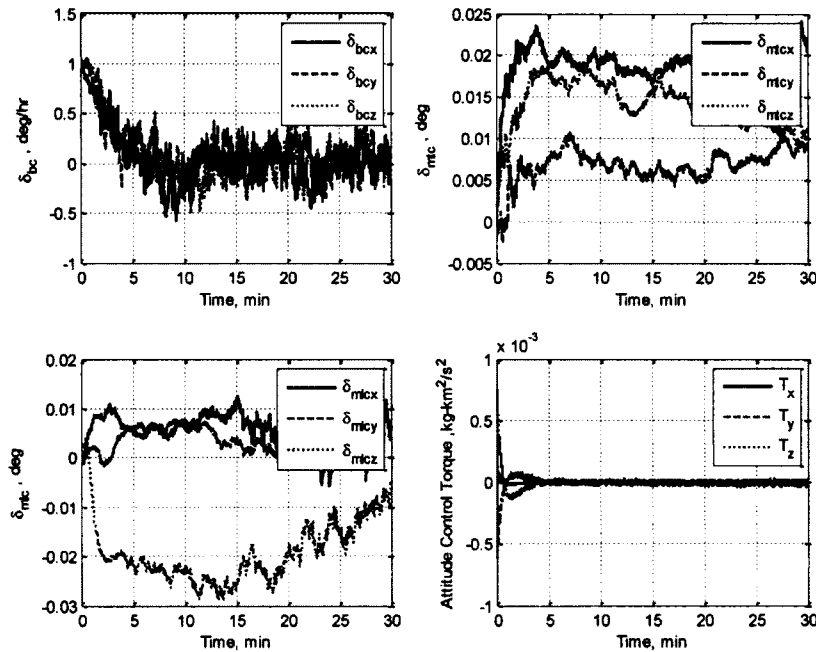
Figure 5.5 Uncertain Parameter Navigation Errors and Attitude Control Torque

A complete rendezvous and close proximity operation example is considered next, and consists of three main segments: inbound segment, flyaround segment, and outbound segment. Each segment of the glideslope is followed by 3 minutes of station keeping. First, for the inbound segment, the chaser starts to approach the target from [58 - 580 0]m behind the target and ends at [0 -100 0]m, effected by 10 pulses in 20 minutes, decelerating the chaser from several meters per seconds to rest. After 3 minutes of station keeping at -100m behind the target, the chaser performs a 100m 20 pulse flyaround in 20 minutes. The chaser then stationkeeps behind the target for 3 minutes, followed by an outbound accelerating glideslope from -100m to -1000m in 10 pulses over 20 min. The chase then stays at rest at that location for another 3 minutes. The results of this scenario are shown in Figures 5.6 and 5.7. In all of these figures, different segments of the glideslope are shown and the variations of in-plane relative motion of the chaser with

respect to the target vehicle are presented. Figure 5.6 shows the relative position and velocity plots of relative motion along with the required ΔV to achieve this trajectory maneuver, while Figure 5.7 shows the error in relative position and velocity between the true model and the navigation model. In all of the above glideslopes, the overall performance of the rendezvous and proximity operations are satisfactory.
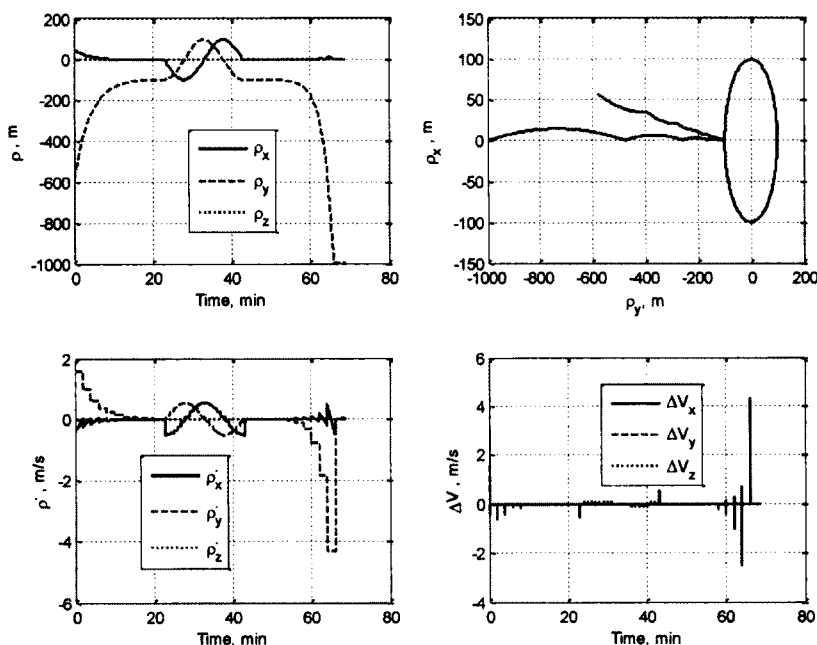
Figure 5.6 Relative Motion Multipulse Glideslope Scenario 1 using TH Model

Similar to the TH model, the LTV model is considered here for the same scenario. First the navigation filter performance is presented in Figures 5.8 and 5.9 along with required attitude control torque. From these figures, using the LTV model in the design process of the navigation system is an appropriate option, since the navigation filter performance as indicated by the convergence rate and stability is highly successful.
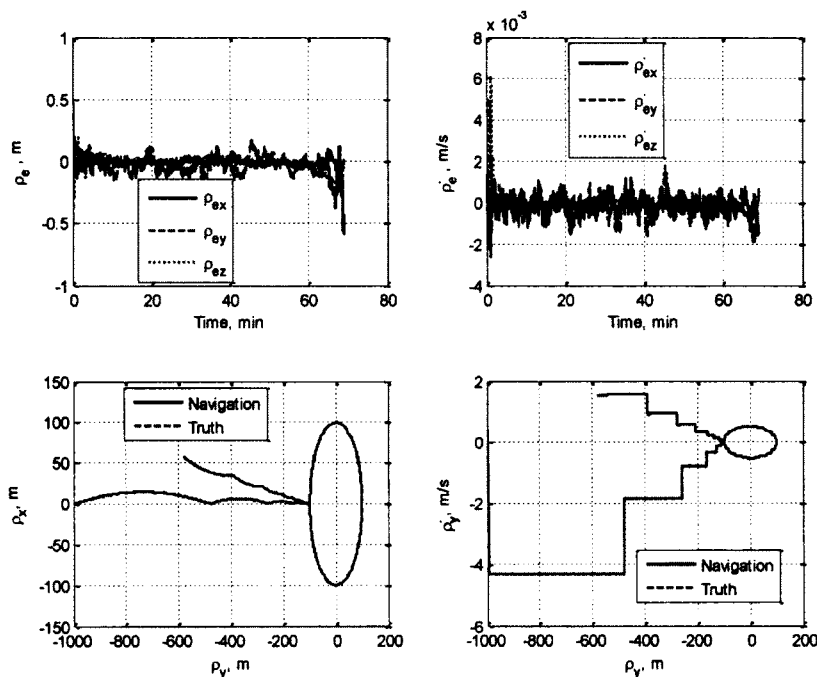
Figure 5.7 Scenario 1 Navigation and Control Performance using TH Model

The basic glidelope rendezvous and close proximity operation scenario, used to evaluate the performance of the entire closed loop relative position and attitude control system with the navigation filter, consists of two simulation cases. In the first case, the LTV model is used with discrete thrust, and consists of three main segments: inbound, flyaround, and outbound, as shown in Figures 5.10 and 5.11. This case is similar to the previous case used to test the TH model. In the second case, the LTV model is used with continuous thrust and consists of two main segments: an inbound segment and an outbound segment. Each segment of the glideslope is followed by 3 minutes of station keeping. First, during the inbound segment, the chaser starts to approach the target from [58 -580 0]m behind the target and ends at [0 -100 0]m. After 3 minutes of station keeping at -100m behind the target, the chaser starts to depart from the target leading to a

new location -1000m behind the target. The chase then stays at rest at that location for another 3 minutes. The results of this scenario are shown in Figures 5.12 and 5.13. In both of these figures, different segments of the glideslope are shown and the variations of in-plane relative motion of the chaser with respect to the target vehicle are presented. Figure 5.12 shows the relative position and velocity plots of relative motion along with the required ΔV to achieve this trajectory maneuver, while Figure 5.13 shows the error in relative position and velocity between the true model and the navigation model. Again, as indicated by these figures in all of the above glideslopes, the overall performance of the GN&C rendezvous and proximity operations are satisfactory.
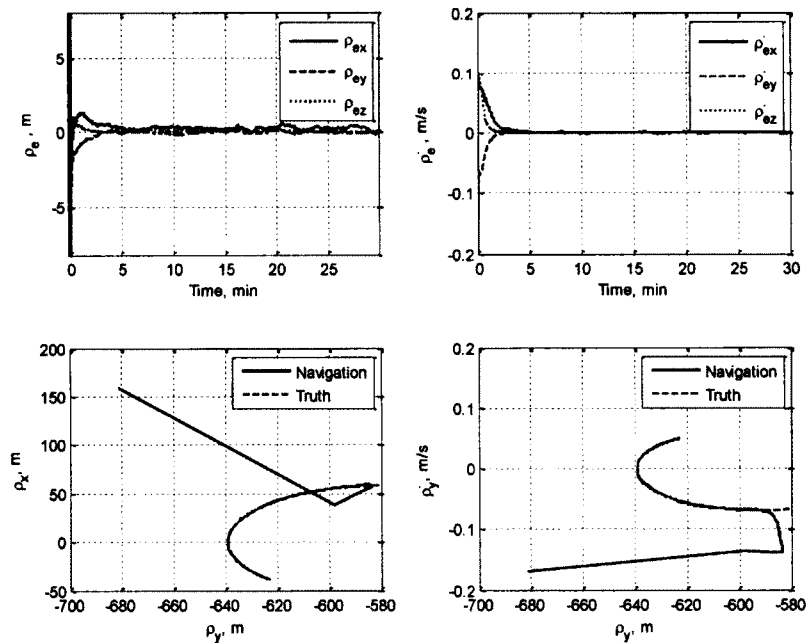
**Figure 5.8 Navigation Performance Without ΔV using LTV Model**
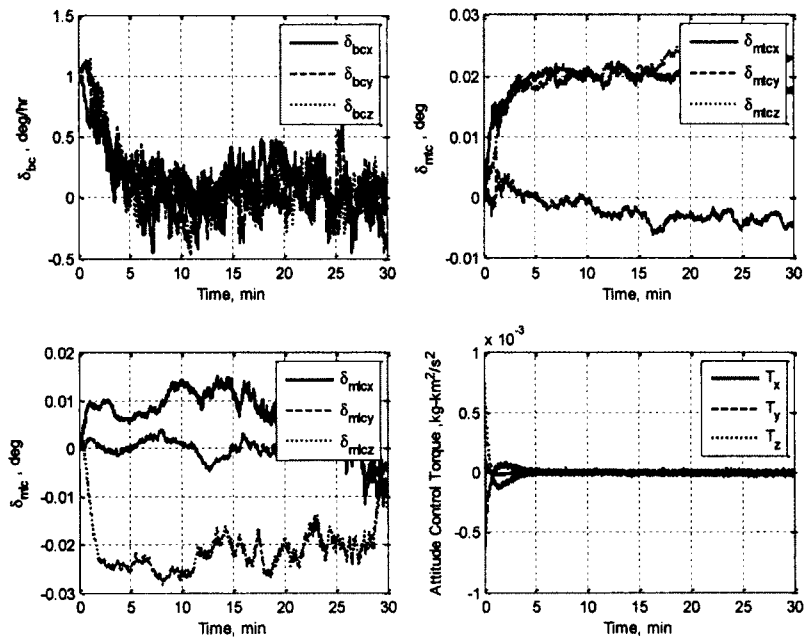
Figure 5.9 Uncertain Parameter Navigation Errors and Attitude Control Torque

Figure 5.10 Relative Motion Multipulse Glideslope Scenario 1 using LTV Model

Figure 5.11 Scenario 1 Navigation and Control Performance using LTV Model
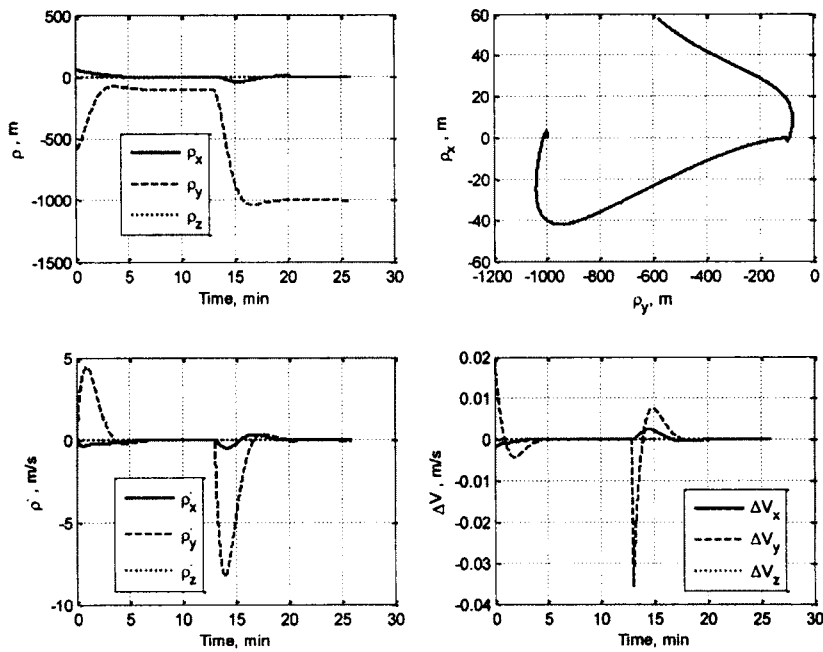
Figure 5.12 Relative Motion Continuous Glideslope Scenario 1 using LTV Model
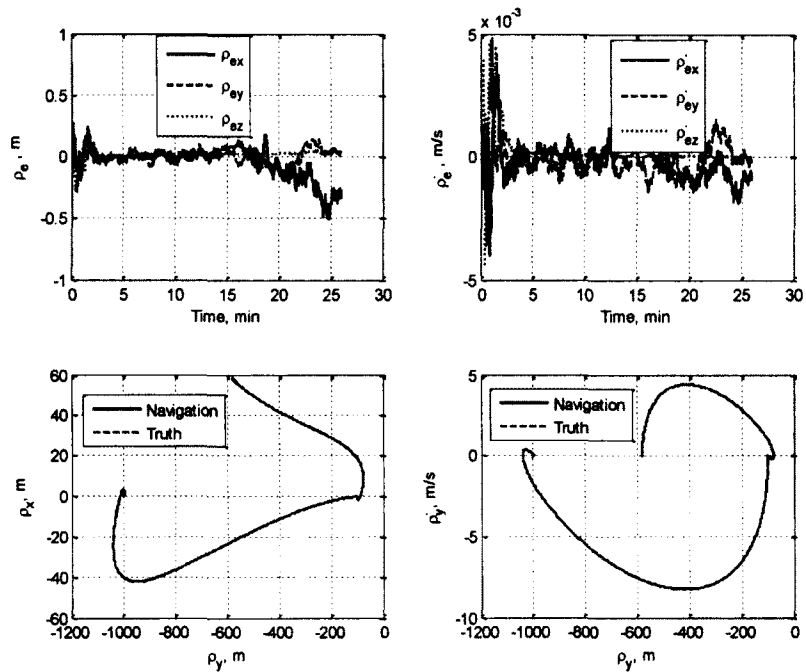
Figure 5.13 Scenario 1 Navigation and Control Performance using LTV Model

The initial conditions for the second scenario that is used to evaluate the performance of the GN&C system are listed in Table 5.2 and 5.3. In this scenario, the TH and LTV model are used as before in the first scenario to design the navigation filter and to accomplish the tracking maneuvers.

Table 5.3 Vehicles Orbital Elements

Parameter	Target	Chaser
a, km	6723.2576	6723.3920
e	0.1	0.1005
i, deg	51.6467	51.6493
Ω, deg	188. 0147	188. 0128
ω, deg	174.3022	174.3005
f, deg	270.0882	270.0852

The glideslope consists of three main segments: inbound, flyaround, and outbound. Each segment of the glideslope is also followed by 3 minutes of station keeping in which there is no ΔV applied. First, during the inbound segment, the chaser starts to approach the target from [-510.97 -686.36 315.24]m behind the target and ends at [0 -150 0]m. After 3 minutes of station keeping at -150m behind the target, the chaser starts to depart away from the target leading to a new location [200 -500 -200]m with respect to the target local vertical local horizontal coordinate frame. The chaser then stays at rest at that location for another 3 minutes. The results of this scenario are shown, in Figures 5.14-5.17. In all of these figures, different segments of the glideslope are shown and the variations of in-plane relative motion of the chaser with respect to target vehicle are presented. Figure 5.14 and 5.16 show the relative position and velocity plots of relative motion along with the required ΔV to achieve this trajectory maneuver for both the LTV and TH models, respectively, while Figures 5.15 and 5.17 show the corresponding errors in relative position and velocity between the true model and navigation model. This scenario shows the effectiveness of using the proposed LTV and TH models coupled with attitude dynamics to model the relative motion in the relative coordinate system and to perform close proximity operations.
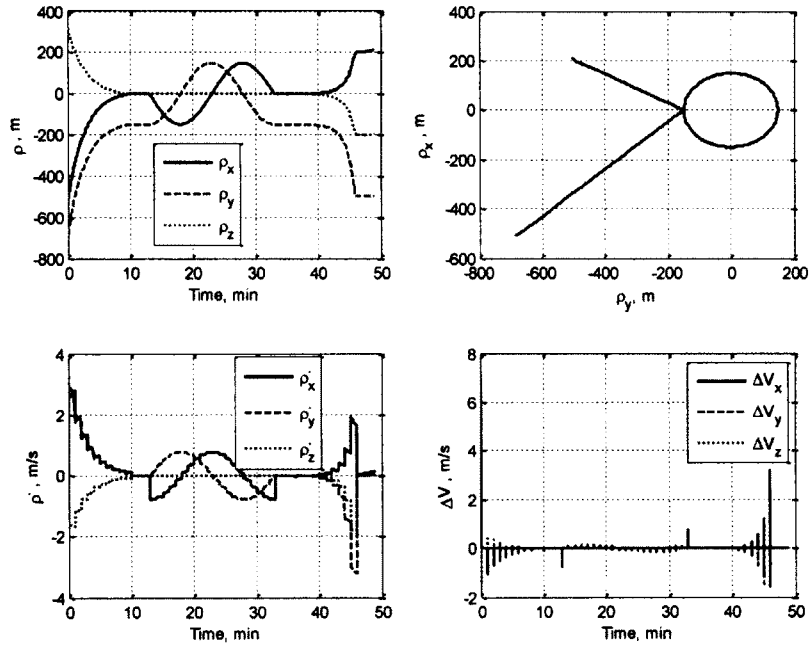
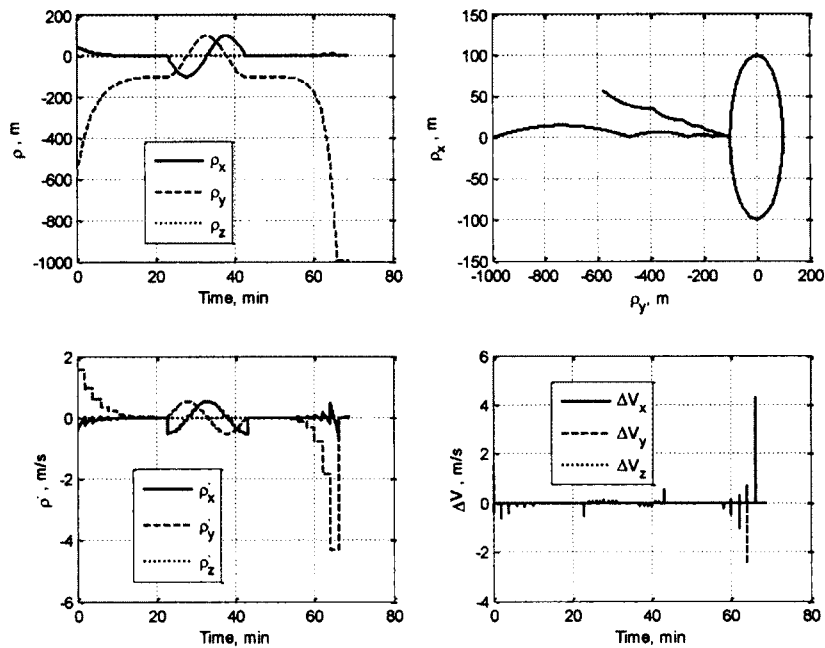**Figure 5.14 Relative Motion Multipulse Glideslope Scenario 2 using LTV Model**
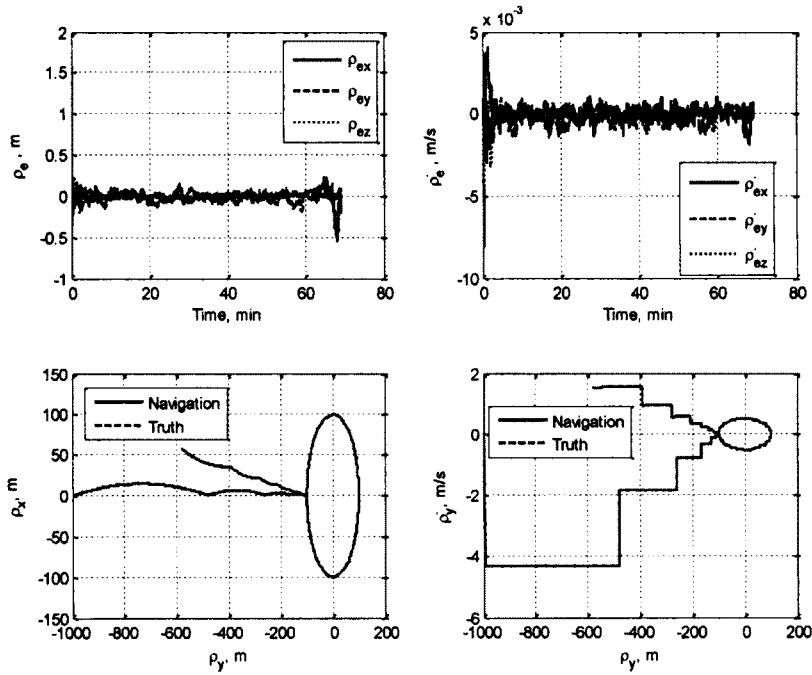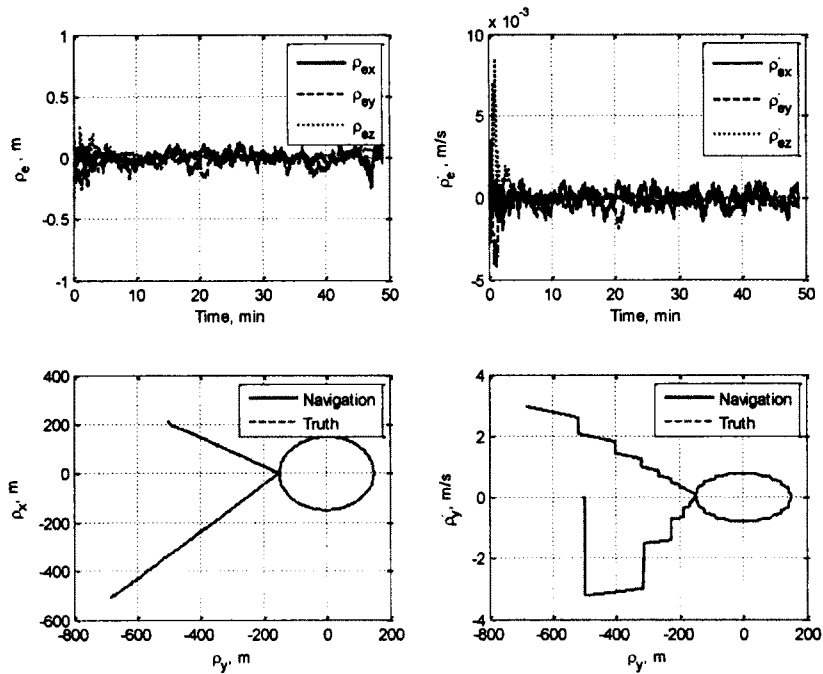
Figure 5.15 Scenario 2 Navigation and Control Performance using LTV Model
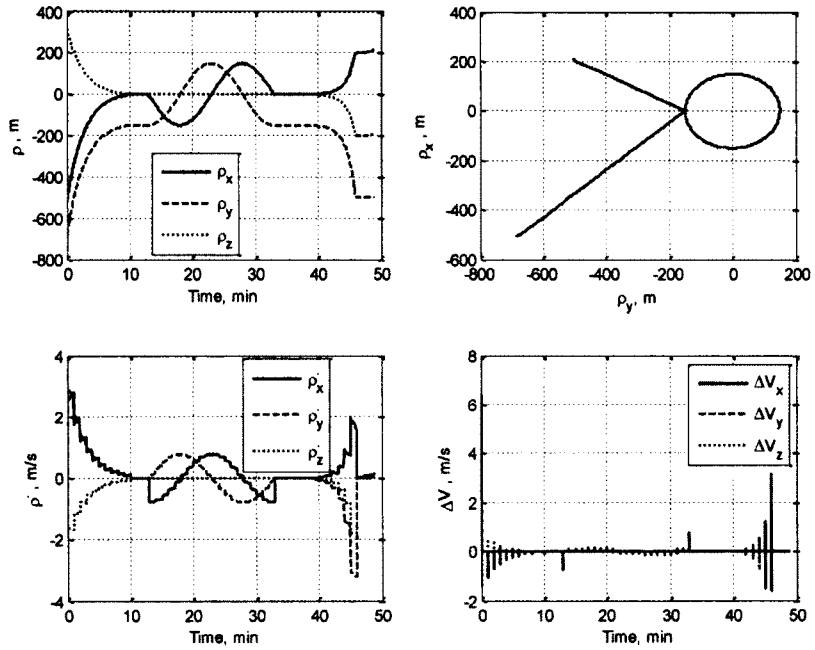
**Figure 5.16 Relative Motion Multipulse Glideslope Scenario 2 using TH Model**
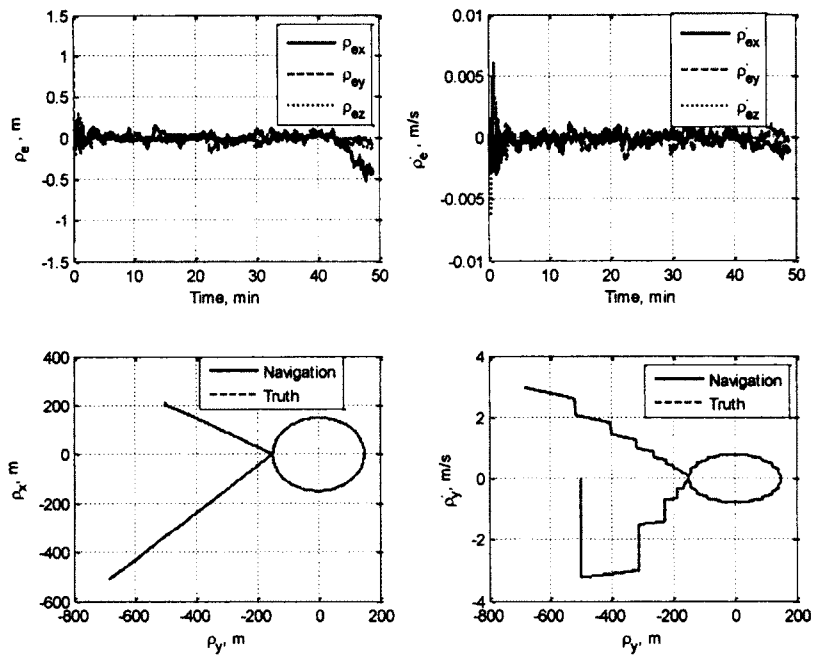
Figure 5.17 Scenario 2 Navigation and Control Performance using TH Model

5.7 Summary

In this chapter, the development of relative navigation, guidance, and control algorithms of an autonomous space rendezvous and docking system are presented. These algorithms are based on using the TH and LTV models. The navigation system uses an extended Kalman filter to estimate the relative position and velocity of the chaser vehicle with respect to the target vehicle and the chaser attitude and gyros biases. This filter uses the range and angle measurements of the target relative to the chaser from a simulated LIDAR system, along with the star tracker and gyro measurements of the chaser. The corresponding measurement models, process noise matrix, and other filter parameters are provided. The guidance and control algorithms are based on the glideslope used in the past for rendezvous and proximity operations of the Space Shuttle with other vehicles. These algorithms are used to approach, flyaround, and to depart from a target vehicle in elliptic orbits. Another proposed guidance technique, based on a simple PD controller, was also investigated. The algorithms are general and able to translate the chaser vehicle in any direction. Numerical nonlinear simulations that illustrate the relative navigation, attitude estimation, guidance, and control algorithms' performance and accuracy are evaluated in the current chapter. The analyses included the navigation errors, trajectory dispersions, and attitude dispersions.

6. CONCLUSIONS

6.1 Summary

Although significant progress and technical development have been achieved with regards to orbital rendezvous such as International Space Station supply and repair, and automated inspection, servicing, and assembly of space systems, there are limitations to the traditional methods that struggle to meet the new demands for orbital rendezvous. Presently, to perform such close proximity operational missions, controllers generally require significant cooperation between vehicles, and utilize man-in-the-loop to ensure successful maneuvering of both spacecraft. The interest in autonomous rendezvous and proximity operations has increased with the recent demonstration of XSS-11, Demonstration of Autonomous Rendezvous Technology, and Orbital Express. Autonomous rendezvous and proximity operations have also been demonstrated by Japanese EST-VII, and the Russian Progress vehicles. In addition, future missions to the ISS will require autonomous rendezvous and proximity operations.

Many relative motion modeling and control strategies have been designed using the linearized Clohessy-Wiltshire equations to describe the relative motion between satellites. The CW equations are valid if two conditions are satisfied: (1) the distance between the chaser and the target is small compared with the distance between the target and the center of the attracting planet, and (2) the target orbit is near circular. The CW equations do not include any disturbance forces, for example gravitational perturbations and environmental forces (solar radiation pressure and atmospheric drag). Alternative linear equations that have been used to model the relative motion are the Tschauner-Hempel equations. These expressions generalize the CW equations and are similar to

them in their derivation and types of applications. Tschauner and Hempel derived these equations from the viewpoint of rendezvous of a spacecraft with an object in an elliptical orbit. This dissertation has presented an innovative way to obtain the complete analytical solution by deriving the state transition matrix explicitly in time. This form of solution is used to analyze the relative motion between the chaser and the target vehicles in the relative frame of motion more efficiently and rapidly than solving the exact nonlinear differential equations in the inertial coordinate system. The TH equations do not take into account any perturbation forces. These perturbations have a significant effect on the satellite relative motion.

Due to the previous limitations of the CW and TH models, this dissertation proposed another innovative linear model that includes both the J_2 perturbation that reflects the Earth oblateness effect and atmospheric drag perturbation in the Cartesian coordinate orbital frame with little complication. Especially in low Earth orbits, these perturbations have a deep influence on the relative dynamics and their inclusion in the linear model can sensibly increase the performance of the linear filters, allow greater insight of satellite relative motion, and provide an opportunity to investigate alternative feedback control strategies for the proximity operations. By using these models, this dissertation presented simple guidance algorithms for glideslope and circumnavigation to autonomously approach, flyaround, and depart from a target vehicle.

This dissertation uses an extended Kalman filter formulation to estimate the relative motion and chaser attitude using range and angle measurements from a LIDAR system coupled with gyro and star tracker measurements of the chaser. The Kalman filter basically consists of two main stages. The first stage is the propagation stage, where the

states are propagated numerically, based on the proposed linear models. The second stage comes when the measurements from the sensors are available and it is used to update the states of the first stage. The corresponding measurement models, process noise matrix, and other filter parameters are provided. Momentum wheels are assumed for attitude control and thrusters are assumed for translation control. The effects of the navigation filter, pointing algorithms, and control algorithms are included in the analysis.

The dissertation objectives are summarized as follows: (1) develop linearized high fidelity models for relative motion in a perturbed orbit that take into account target orbit eccentricity, (2) design a navigation filter that can determine the relative position and velocity between target and chaser vehicles, as well as orientations and angular rates of the chaser that support closed loop proximity attitude control operations and maneuvers, and (3) design a control system for the chaser vehicle to either approach, flyaround, or depart from the target vehicle in proximity operations in a general perturbed orbit for coupled translation and rotation relative motion.

The results of this study indicate that the proposed developed models are clearly effective at estimating the relative position and velocity and controlling the relative trajectory. In addition, these models are not restricted to a circular orbit but can be used as well for eccentric orbits. Furthermore, by using these models, simple guidance algorithms for glideslope and circumnavigation are developed to autonomously approach, flyaround, and depart from a target vehicle. The relative navigation in this study utilizes range, azimuth, and elevation measurements of the target relative to the chaser from a simulated LIDAR system along with the star tracker and gyro measurements of the chaser and an extended Kalman filter. Vehicle attitude dynamics, attitude tracking

control, attitude determination, and uncertainties like measurement biases and sensor misalignments are considered in this study to fire the thrusters in the right direction in the chaser coordinate frame. Numerical nonlinear high fidelity simulation examples that illustrate the relative navigation, attitude estimation, guidance, and control algorithms performance and accuracy are evaluated.

6.2 Future Work

There are several extensions that can be made to this work in the future. First, it was assumed that the target had some level of cooperation and it was known (orbit and moments of inertia). Is it possible to approach an unknown vehicle and determine the relative position and, consequently, the orientation between the vehicles? Also, can the target's orbit and moments of inertia be accurately estimated? Can the navigation filter adapt and teach itself properties of the target? Deriving solutions to these important questions can affect future missions.

Second, several topics and simulation scenarios that extensively analyze off nominal situations, limitations and operational range of the sensors, and limitations of the actuator should be considered by the analyst.

Lastly, besides all of these theoretical developments, the experimental validations of autonomous guidance, navigation, and control in close proximity operations, including rendezvous and docking should be considered to evaluate the algorithm performances. The evaluation process should ensure that safe, autonomous collision-free docking is achieved and that fuel consumption is minimized.

REFERENCES

[1]Fehse, W., *Automated Rendezvous and Docking of Spacecraft*, Cambridge University Press, U.K., 2003.

[2]Woffinden, D. C. and Geller, D. K., "Navigating the Road to Autonomous Orbital Rendezvous," Journal of Spacecraft and Rockets, Vol. 44, No. 4, 2007, pp. 898-909.

[3]Morris, J. C., "Automated Spacecraft Docking Using a Vision-Based Relative Navigation Sensor," M.S. Thesis, Dept. of Aerospace Engineering, Texas A&M University, College Station, TX, 2009.

[4]Boynton, J. H. and Kleinknecht, K. S., "Systems Design Experience from Three Manned Space Programs," Journal of Spacecraft and Rockets, Vol. 7, No. 7, 1970, pp. 770-784.

[5]Askins, B. and Card, M., *Automated Rendezvous and Capture Review: Executive Summary*, NASA TM-108597, November 1991.

[6]Polites, M. E., "Technology of Automated Rendezvous and Capture in Space," Journal of Spacecraft and Rockets, Vol. 36, No. 2, 1999, pp. 280-291.

[7]Goodman, J. L., "History of Space Shuttle Rendezvous and Proximity Operations," Journal of Spacecraft and Rockets, Vol. 43, No. 5, 2006, pp. 944-959.

[8]Siddiqi, A. A., *Challenge to Apollo: The Soviet Union and the Space Race, 1945-1974*, Chap. 14: Getting Back on Track, SP-4408, NASA History Division, 2000, pp. 609-652.

[9]Kawano, I., Mokuno, M., Kasai, T., and Suzuki, T., "Result of Autonomous Rendezvous Docking Experiment of Engineering Test Satellite-VII," Journal of Spacecraft and Rockets, Vol. 38, No. 1, 2001, pp. 105-111.

[10]Oda, M. and Inaba, N., "Mission Design of an In-Orbit Satellite Inspection-Feasibility of the In-Orbit Satellite Servicing," Proceedings of the AAS/AIAA Space Flight Mechanics Meeting, Santa Barabara, CA, February 2001, pp. 2071-2085.

[11]Japan Aerospace Exploration Agency Press Release (February 2009), "HTV: An indispensable part of ISS operations," Available: www.jaxa.jp/article/special/transportation/torano01_e.html.

[12]Rumford, T. E., "Demonstration of Autonomous Rendezvous Technology (DART) Project Summary," Proceedings of SPIE Space Systems Technology and Operations, Vol. 5088, Orlando, FL, April 2003, pp. 10-19.

[13]Weismuller, T. and Leinz, M., "GN&C Technology Demonstrated by the Orbital Express Autonomous Rendezvous and Capture Sensor System," AAS 06-016, 29th Annual AAS Guidance and Control Conference, Breckenridge, CO, February 2006.

[14]Cislaghi, M., Lellouch, M., and Pairot , J. M., "The ATV Rendezvous Predevelopment (ARP) Project," ESA Directorate of Manned Spaceflight and Microgravity, Noordwijk, The Netherlands, European Space Agency Bulletin 89, February 1997.

[15]Sengupta, P., "Satellite Relative Motion Propagation and Control in The Presence of J_2 Perturbations," M.S. Thesis, Dept. of Aerospace Engineering, Texas A&M University, College Station, TX, 2003.

[16]Vaddi, V. V., "Modeling and Control of Satellite Formations," Ph.D. Dissertation, Dept. of Aerospace Engineering, Texas A&M University, College Station, TX, 2003.

[17]Geller, D., "Analysis of the Relative Attitude Estimation and Control Problem for Satellite Inspection and Orbital Rendezvous," Journal of Astronautical Sciences, Vol. 55, No. 2, 2007.

[18]Subbarao, K. and Welsh, S., "Nonlinear Control of Motion Synchronization for Satellite Proximity Operations," Journal of Guidance, Control, and Dynamics, Vol. 31, No. 5, 2008, pp. 1284-1294.

[19]Lee, S. S., "Dynamics and Control of Satellite Relative Motion: Designs and Applications," Ph.D. Dissertation, Dept. of Aerospace and Ocean Engineering, Virginia Polytechnic Institute and State University, Blacksburg, VA, 2009.

[20]Clohessy, W. H. and Wiltshire, R. S., "Terminal Guidance System for Satellite Rendezvous," Journal of the Astronautical Sciences, Vol. 27, No. 9, 1960, pp. 653-678.

[21]Lawden, D. F., Optimal Trajectories for Space Navigation, Butterworths, London, 1963.

[22]Carter, T. E., "New Form for the Optimal Rendezvous Equations Near a Keplerian Orbit," Journal of Guidance, Control, and Dynamics, Vol. 13, No. 1, 1990, pp. 183-186.

[23]Tschauner, J. and Hempel, P., "Rendezvous zu einem in Elliptischer Bahn Umlaufenden Ziel," Acta Astronautica, Vol. 11, 1965, pp. 104-109.

[24]Melton, R. G., "Time-Explicit Representation of Relative Motion Between Elliptical Orbits," Journal of Guidance, Control, and Dynamics, Vol. 23, No. 4, 2000, pp. 604-610.

[25]Broucke, R. A., "Solution of the Elliptic Rendezvous Problem with the Time as Independent Variable," Journal of Guidance, Control, and Dynamics, Vol. 26, No. 4, 2003, pp. 615-621.

[26]Yamanaka, K. and Ankersen, F., "New State Transition Matrix for Relative Motion on an Arbitrary Elliptical Orbit," Journal of Guidance, Control, and Dynamics, Vol. 25, No. 1, 2002, pp. 60-66.

[27]Kechichian, J. A., "Motion in General Elliptic Orbit with Respect to a Dragging and Precessing Coordinate Frame," Journal of Astronautical Sciences, Vol. 46, No. 1, 1998, pp. 25-46.

[28]Sedwick, R. J., Miller, D. W., and Kong, E. M. C., "Mitigation of Differential Perturbations in Clusters of Formation Flying Satellites," Journal of the Astronautical Sciences, Vol. 47, No. 3, 1999, pp. 309-331.

[29]Schweighart, S. A. and Sedwick, R. J., "High-Fidelity Linearized J_2 Model for Satellite Formation Flight," Journal of Guidance, Control, and Dynamics, Vol. 25, No. 6, 2002, pp. 1073-1080.

[30]Vadali, S. R., "An Analytical Solution for Relative Motion of Satellites," Proceedings of the Fifth International Conference on Dynamics and Control of Structures and Systems in Space, Cranfield, U. K., July 2002.

[31]Yan, H., Sengupta, P., Vadali, S. R., and Alfriend, K. T., "Development of a State Transition Matrix for Relative Motion Using the Unit Sphere Approach," AAS 04-163, Proceedings of the 14th AAS/AIAA Space Flight Mechanics Meeting, Maui, HI, February 2004.

[32]Alfriend, K. T. and Yan, H., "Evaluation and Comparison of Relative Motion Theories," Journal of Guidance, Control, and Dynamics, Vol. 28, No. 2, 2005, pp. 254-261.

[33]Gim, D. W. and Alfriend, K. T., "State Transition Matrix of Relative Motion for the Perturbed Noncircular Reference Orbit," Journal of Guidance, Control, and Dynamics, Vol. 26, No. 6, 2003, pp. 956-971.

[34]Pearson, D. J., "The Glideslope Approach," AAS 89-162, Advances in the Astronautical Sciences, Vol. 69, American Astronautical Society, San Diego, CA, 1989, pp. 109-123.

[35]Hablani, H. B., Tapper, M. L., and Dana-Bashian, D. J., "Guidance and Relative Navigation for Autonomous Rendezvous in a Circular Orbit," Journal of Guidance, Control, and Dynamics, Vol. 25, No. 3, 2002 , pp. 553-562.

[36]Inalhan, G., Tillerson, M., and How, J. P., "Relative Dynamics and Control of Spacecraft Formation in Eccentric Orbits," Journal of Guidance, Control, and Dynamics, Vol. 25, No. 1, 2002, pp. 48-58.

[37]Zimpfer, D. and Spehar, P., "STS-71 Shuttle/Mir GNC Mission Overview," AAS 96-129, Advances in the Astronautical Sciences, Vol. 93, Pt. I, American Astronautical Society, San Diego, CA, 1996, pp. 441-460.

[38]Cruzen, C. A., Lomas, J. J., and Dabney, R. W., "Test Results for the Automated Rendezvousand Capture System," AAS 00-003, Advances in the Astronautical Sciences, Vol. 104, American Astronautical Society, San Diego, CA, 2000, pp. 35-56.

[39]Upadhyay, T., Cotterill, S., and Deaton, A. W., "Autonomous Reconfigurable GPS/INS Navigation and Pointing System for Rendezvous and Docking," AIAA 92-1390, AIAA Space Programs and Technologies Conference, Huntsville, AL, March, 1992.

[40]Howard, R. T., Bryan, T. C., Brook, M. L., and Dabney, R. W., "The Video Guidance Sensor: A Flight Proven Technology," AAS Paper 99-025, Advances in the Astronautical Sciences, American Astronautical Society, San Diego, CA, 1999, pp. 281–298.

[41]Battin, R. H., An Introduction to the Mathematics and Methods of Astrodynamics, AIAA Education Series, Reston, VA, 1999.

[42]Battin, R. H. and Vaughan R. M., "An Elegant Lambert Algorithm," Journal of Guidance, Control, and Dynamics, Vol. 7, No. 6, 1984, pp. 662-670.

[43]Vallado, D. A., Fundamentals of Astrodynamics and Applications, 2nd ed., Microcosm Press, El Segundo, CA, 2001.

[44]Wie, B. and Barba, P. M., "Quaternion Feedback for Spacecraft Large Angle Maneuvers," Journal of Guidance, Control, and Dynamics, Vol. 8, No. 3, 1985, pp. 360-365.

[45]Crassidis, J. L. and Vadali, S. R., "Optimal Variable-Structure Control Tracking of Spacecraft Maneuvers," Journal of Guidance, Control, and Dynamics, Vol. 23, No. 3, 2000, pp. 564-566.

[46]Sharma, R. and Tewari, A., "Optimal Nonlinear Tracking of Spacecraft Attitude Maneuvers," IEEE Transactions on Control Systems Technology, Vol. 12, No. 5, 2004, pp. 677-682.

[47]Zhou, Z. and Colgren, R., "Nonlinear Attitude Control for Large and Fast Maneuvers," AIAA 05-6177, AIAA Guidance, Navigation, and Control Conference and Exhibit, San Francisco, CA, August 2005.

[48]Hall, C. D., Tsiotras, P., and Shen, H., "Tracking Rigid Body Motion Using Thrusters and Momentum Wheels," Journal of the Astronautical Sciences, Vol. 50, No. 3, 2002, pp. 311-323.

[49]Lo, S. C. and Chen, Y. P., "Smooth Sliding-Mode Control for Spacecraft Attitude Tracking Maneuvers," Journal of Guidance, Control, and Dynamics, Vol. 18, No. 6, 1995, pp. 1345-1349.

[50]Kojima, H. and Mukai, T., "Smooth Reference Model Adaptive Sliding-Mode Control for Attitude Synchronization with a Tumbling Satellite," JSME International Journal Series C, Vol. 47, No. 2, 2004, pp. 616-625.

[51]Kang, W., Yeh, H. H., and Sparks, A., "Coordinated Control of Relative Attitude for Satellite Formation," AIAA 01-4093, AIAA Guidance, Navigation, and Control Conference, Montreal, CAN, August 2001.

[52]VanDyke, M. C. and Hall, C. D., "Decentralized Coordinated Attitude Control within a Formation of Spacecraft," Journal of Guidance, Control, and Dynamics, Vol. 29, No. 5, 2006, pp. 1101-1109.

[53]Yuan, C. Q., Li, J. F., Wang, T. S., and Baoyin, H. X., "Robust Attitude Control for Rapid Multi-Target Tracking in Spacecraft Formation Flying," Applied Mathematics and Mechanics, Vol. 29, No. 2, 2008, pp. 185-198.

[54]Schaub, H. and Junkins, J. L., Analytical Mechanics of Space Systems, American Institute of Aeronautics and Astronautics, Reston, VA, 2003.

[55]Carter, T. E., "State Transition Matrices for Terminal Rendezvous Studies: Brief Survey and New Example," Journal of Guidance, Control, and Dynamics, Vol. 21, No. 1, 1998, pp. 148-155.

[56]Sengupta, P. and Vadali, S. R., "Relative Motion and the Geometry of Formations in Keplerian Elliptic Orbits," Journal of Guidance, Control, and Dynamics, Vol. 30, No. 4, 2007, pp. 953-964.

[57]Okasha, M. and Newman, B., "Relative Motion and Autonomous Rendezvous in Keplerian Elliptic Orbits," AIAA 2010-7593, Proceedings of the AIAA Guidance, Navigation, and Control Conference, Toronto, Ontario, CAN, August, 2010.

[58]Woffinden, D. C., "On-Orbit Satellite Inspection Navigation and Δv Analysis," M.S. Thesis, Dept. of Aeronautics and Astronautics, Massachusetts Institute of Technology, Cambridge, MA, 2004.

[59]De Vries, J. P., "Elliptic Elements in Terms of Small Increments of Position and Velocity Components," AIAA Journal, Vol. 1, No. 11, 1963, pp. 2626-2629.

[60]Carter, T. E. and Humi, M., "Fuel-Optimal Rendezvous Near a Point in General Keplerian Orbit," Journal of Guidance, Control, and Dynamics, Vol. 10, No. 6, 1987, pp. 567-573.

[61]Lear W. M., *Kalman Filtering Techniques*, NASA TR-JSC-20688, NASA Mission Planning and Analysis Division, Houston, TX, 1985.

[62]Vaughan, A. T., "A Monte-Carlo Performance Analysis of Kalman Filter and Targeting Algorithms for Autonomous Orbital Rendezvous," M.S. Thesis, Massachusetts Institute of Technology, Cambridge, MA, May 2004.

[63]Kalman R. E., "A New Approach to Linear Filtering and Prediction Problems," Transactions of the ASME, Journal of Basic Engineering, Vol. 82, No. Series D, 1960, pp. 35-45.

[64]Gelb A., editor, *Applied Optimal Estimation*, The MIT Press, Cambridge, MA, 1974.

[65]Siouris G. M., *An Engineering Approach to Optimal Control and Estimation Theory*, John Wiley & Sons, New York, NY, 1996.

[66]Brown, R. G. and Hawag, P., *Introduction to Random Signals and Applied Kalman Filtering*, John Wiley & Sons, NY, New York, 1997.

[67]Woffinden, D. C., "Angles-Only Navigation for Autonomous Orbital Rendezvous," Ph.D. Dissertation, Utah State University, Logan, UT, December 2008.

[68]Woffinden, D. C. and Geller, D. K., "Relative Angles-Only Navigation and Pose Estimation for Autonomous Orbital Rendezvous," Journal of Guidance, Control, and Dynamics, Vol. 30, No. 5, 2007, pp. 1455-1469.

[69]Jenkins, S. C. and Geller, D. K., "State Estimation and Targeting for Autonomous Rendezvous and Proximity Operations," AAS 07-316, Proceedings of the AIAA/AAS Astrodynamics Specialists Conference, Mackinac Island, MI, August 2007.

[70]Junkins, J. L., Kim, S., Crassidis, L., Cheng, Y., and Fosbury, A. M., "Kalman Filtering for Relative Spacecraft Attitude and Position Estimation," AIAA 2005-6087, Proceedings of the AIAA Guidance, Navigation, and Control Conference, San Francisco, CA, August, 2005.

[71]Okasha, M. and Newman, B., "Relative Motion Guidance, Navigation and Control for Autonomous Spacecraft Rendezvous," AAS 11-212, Proceedings of the 21st AAS/AIAA Space Flight Mechanics Meeting, New Orleans, LA, February, 2011.

[72]Okasha, M. and Newman, B., "Relative Motion Modeling and Control in a Perturbed Orbit," AAS 11-211, Proceedings of the 21st AAS/AIAA Space Flight Mechanics Meeting, New Orleans, LA, February, 2011.

[73]Okasha, M. and Newman, B., "Relative Motion Guidance, Navigation and Control for Autonomous Orbital Rendezvous," AIAA 2011-6427, GNC-26 Proceedings of the AIAA Guidance, Navigation, and Control Conference, Portland, OR, August, 2011.

[74]Okasha, M. and Newman, B., "Guidance, Navigation and Control for Satellite Proximity Operations using Tschauner-Hempel Equations," AIAA 2011-6428, GNC-26, Proceedings of the AIAA Guidance, Navigation, and Control Conference, Portland, OR, August, 2011.

[75]Crassidis, J. L. and Junkins, J. L., *Optimal Estimation of Dynamic System*, CRC Press, Boca Raton, FL, 2004.

[76]Okasha, M. and Newman, B., "Switching Principles to Circumvent Euler Angle Singularity," AIAA 2010-7651, Proceedings of the AIAA Guidance, Navigation, and Control Conference, Toronto, Ontario, CAN, August, 2010.

[77]Pittelkau, M. E., "Rotation Vector in Attitude Estimation," Journal of Guidance, Control, and Dynamics, Vol. 26, No. 6, 2003 , pp. 855-860.

[78]Wie, B., *Space Vehicle Dynamics and Control*, American Institute of Aeronautics and Astronautics, Reston, VA, 1998.

VITA

Mohamed El Sayed Ali Abd El Aziz Okasha

Career Objective

Make a significant contribution to the advancement of space flight and exploration, particularly in the field of guidance, navigation, and control systems.

Education

Ph.D. Degree: Aerospace Engineering

Old Dominion University, Norfolk, VA, USA, 2007-2012

- Emphasis on guidance, navigation, and control (GN&C)
- Dissertation: *Dynamics and Control of Satellite Relative Motion in Proximity Operations*

M.S. Degree: Aerospace Engineering

Cairo University, Cairo, Egypt, 2001-2005

- Emphasis on dynamics and controls
- Thesis: S*pacecraft Attitude–Power Tracking Control Using Thrusters and Momentum Wheels*

B.S. Degree: Aerospace Engineering

Cairo University, Cairo, Egypt, 1995-2000

- Emphasis on dynamics and controls
- Project: S*pacecraft Attitude Dynamics and Control*

Experience

Research Assistant, *Old Dominion University (ODU), Mechanical and Aerospace Department,* Norfolk, VA, USA, 2007-2012.

- Developed tools for the analysis of space rendezvous proximity operations
- Created and integrated a navigation filter for orbital rendezvous into a high fidelity simulation tool containing sensors, actuators, orbital dynamics, and GN&C algorithms

Teaching Assistant, *Russian University (ERU),* Cairo, Egypt, 2006-2007.

- Member of Engineering Department
- Taught different courses for undergraduate engineering studies

System Engineer, *YOUSHNOI Design Office,* Dnepropetrovsk, Ukraine, 2003-2005.

- Member of Egypt Sat-1 system engineer group
- Received on-job training to transfer Micro-Satellites technology of mathematical model of spacecraft as an object of control
- Designed, analyzed, and evaluated the attitude determination and control systems (ADCS) performance of Micro-Satellites using Matlab/Simmulink, Satellite Tool Kit (STK), ANSYS, and Mechanical desktop (MDT) software packages

Research Assistant, *National Authority of Remote Sensing and Space Science (NARSS),* Cairo, Egypt, 2003-2007.

- Member of system engineers and member of spacecraft ADCS for Egypt Sat-1 project
- Analyzed and developed tools for spacecraft mission analysis
- Created mathematical models to simulate the spacecraft orbit and attitude trajectory during different phases of operations and evaluated the ADCS performance

Research Assistant, *Aerospace Department, Cairo University,* Cairo, Egypt, 2001-2002.

- Helped design and analyze the attitude determination and control systems of a low Earth orbit spacecraft
- Developed an attitude tracking controller to track both ground target like a ground station and the Sun (to generate maximum power and to track a specified power profile) at the same time